MODULARIZATION OF TOPOLOGY OPTIMIZED STRUCTURES

AN IMAGE MOMENT APPROACH

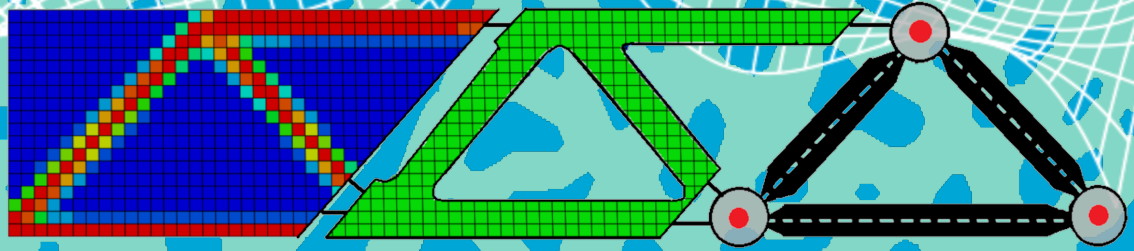

Masters Thesis
Harshavardhan Vijaya Kumar

Aerospace Structures and Materials
Faculty of Aerospace Engineering

TU Delft

SAFRAN

MODULARIZATION OF TOPOLOGY OPTIMIZED STRUCTURES

AN IMAGE MOMENT APPROACH

MODULARIZATION OF TOPOLOGY OPTIMIZED STRUCTURES

AN IMAGE MOMENT APPROACH

Masters Thesis

to obtain the degree of

Master of Science - Aerospace Structures and Materials

at the Delft University of Technology

in collaboration with Safran Cabins, Alkmaar

to be defended publicly on Tuesday September 28, 2021 at 2:00 PM.

Student number:	4897374	
Project duration:	Feb 1, 2020 – Aug 1, 2021	
Thesis committee:	Dr. Sergio R. Turtletaub,	TU Delft
	Dr.-Ing. Saullo G.P. Castro,	TU Delft
	Ir. J. Sinke,	TU Delft
	Ad Eijkelenboom,	V.P R&T, Safran Cabins

This thesis is confidential and cannot be made public until September 30, 2024.

This thesis has been supervised by

Dr. Sergio R. Turteltaub	Associate Professor ASCM, TU Delft
Dr.-Ing. Saullo G.P. Castro	Assistant Professor ASCM, TU Delft
Ad Eijkelboom	Vice President , R&T Safran Cabins, Alkmaar
Suresh Konidala	Structural Engineer, R&T Safran Cabins, Alkmaar

An electronic version of this dissertation will be available at
http://repository.tudelft.nl/.

The art of structure is -
how and where to put the holes.

Le Ricolais

ABSTRACT

Topology optimization (TO) has proven to be a capable design methodology for the realization of lightweight solutions that maximize structural stiffness or other design objectives. Due to its capability to be adapted to suit a wide range of objectives and constraints, both structural and non-structural, TO has been widely applied in all industries, including aerospace. The application of TO in secondary structures offers the scope for further weight savings and, therefore, this thesis investigates the employment of TO on a galley structure provided by Safran-Cabins. The galley structure is an essential equipment for the functioning of passenger aircrafts and hence, provides an ideal product, which once optimized could offer widespread weight saving.

The next generation of commercial aircrafts require solutions which are lightweight and yet economic to manufacture. TO solutions are renowned for their complex architectures and frequent employment in conjunction with additive manufacturing. However, for products such as galleys, which are required to be manufactured in large quantities, complex manufacturing strategies are not economically feasible. Therefore, this thesis proposes a modularization strategy which can be used to augment the monolithic TO solution into an assembly of simpler and identical modules. The modular design strategy has proven to be a capable strategy to enhance manufacturability as well as reduce costs over the board and offers a unique opportunity to leverage the capabilities of TO for employment on a wider range of products.

To achieve the aforementioned goal, an image moment-based modularization strategy is investigated which treats the TO solutions as digital images and identifies positions of simple bar/beam modules within the image based on matching of the image moments. Through a detailed investigation, a fragment constrained bar matching strategy is developed. It is demonstrated that, the proposed matching strategy is capable of identifying positions of bar/beam modules within TO solutions from the literature. Additionally, a post-processing strategy is developed to augment the obtained modules and their positions into simplified and assembled frame structures analogous to the underlying TO solution. The developed framework is employed on the topologically-optimized galley, and its practical capabilities and limitations identified, thus providing a foundational work to be further refined.

CONTENTS

LIST OF FIGURES

LIST OF TABLES

NOMENCLATURE

λ_{ij} i,j ordered 2D Legendre moment

ρ Topology optimization pseudo density.

$B[x_1, y_1, x_2, y_2]$ A bar with endpoints x_1, y_1 and x_2, y_2

$D[(X_{LL}, X_{UL}), (Y_{LL}, Y_{UL})]$ A bounding box between said x and y coordinates

d_{el} Finite element mesh size

$G5$ G5 Galley

L_x Inertial Load factor in the x direction

N_m Moment matrix size

$R_circumscribe$ circumscribing radius of fragment

R_{filter} Checkerboard filter radius

RX, RY, RZ Reaction force limits in x,y and z directions

V_0 Initial Volume

V_{lim} Volume constraint

w_i weight of item i

x_i, y_i, z_i coordinates of centre of gravity of item i

CG Centre of Gravity

EASA European Union Aviation Safety Agency

FWBM Fragment wise bar match

GS Ground Structure

L2E L2 norm of the Error matrix

LM Legendre moment Matrix

MMA Method of Moving Assymptotes

OC Optimality criteria

P_n	Legendre polynomial of order n
RF	Reaction Force
SE	Strain Energy
SIMP	Solid Isotropic Material with Penalization
TO	Topology optimization
UDL	Uniformly distributed Load

PREFACE

As I write this I am reminded of when I first arrived in the Netherlands and I was overwhelmed by the awe-inspiring panorama Delft offered. Everything from canals in the city center to the giant cone on the Library was a stark contrast for a boy who lived in the countryside of a city in India for 20 years and the fact that I was risking homelessness was not helpful. I had never imagined when I had applied to TU Delft, that I would be accepted. This led me to feel like an impostor for a significant portion of my time. However, 3 years later, after the exhilarating courses, the challenging assignments, the countless coffee-aided nights and not to mention a worldwide pandemic, I can confidently claim that TU Delft was definitely the place for me. After the transformative journey these past years I am left humbled, thankful, and thirsty for more.

I would firstly like to thank my supervisors Dr. Sergio Turteltaub and Dr.-Ing Saullo Castro for their guidance throughout the duration of this thesis as well as for the courses they instructed. I still cannot believe that this thesis was an outcome of me just asking about it on a whim during a 10-minute break between classes. I will always be deeply grateful to them for accepting me as their thesis student as well as for the confidence they posed in me to tackle a project such as this. I still remember how walking into Professor Turteltaub's office for a small conversation would lead to an exciting discussion lasting for hours. And I will forever carry with me Professor Saullo's positive attitude of remarking 'That is interesting' at every positive and problematic outcome during the thesis. Both of them will continue to be my role models and have enriched my interest in research as well as have kindled in me an interest in academia even though as Professor Turteltaub claims 'Research is always 2 steps forward and 1 step back or in the worst case 1 step forward and 2 steps back.'

Although my time in the office was limited, I would like to thank Ad Eijkelenboom and Suresh Konidala for their guidance and supervision during this thesis. Although the schedule for the project was delayed by a large extent, I am very grateful to Ad for his understanding and for allowing me to complete it to satisfaction. My conversations with him and other colleagues at the office were instrumental in gaining an understanding of the exciting world that is the commercial aircraft industry. I hope that my efforts in this project will be a useful first step for the development of the next generation of cabin solutions.

I would like to thank all my friends old and new for making my Master's experience the best I could have asked for. Aravind, Srikanth, and Siddharth for their friendship and support whenever I felt completely lost. I will forever cherish our paperclip poker games. Antonin for teaching me that a well-planned schedule can surprise you with

what you can achieve in a small period of time. Kevin, Sean, Arne, and Deacon for the stress-relieving gaming sessions and the heated debates on politics, history, and technology. Alex for his wonderful baked goods. Sebastian and Jens for enlightening me on the nuances of being Dutch, especially the best choice of bread. Each and everyone new friendship I have made here at TU Delft has truly been one I would like to cherish for many years to come.

I strongly believe that I would not be half the person I am if not for the teachers in my life. I would like to thank my high school math tutor Pushpa for teaching me the rigorousness required for mathematics. My choice of study and career in engineering would have not been possible if not for you.

I would like to thank my parents, Mamatha and Vijaya Kumar, without your emotional, physical, and not to mention financial support I would not have been able to pursue this course and thesis. I aim to make both of you proud and hope to do for my children what you both have done for me. Also, I would like to thank my uncle Ravi. I believe in your limited capacity, you have also had a role to play in the person I am today.

Lastly, I would like to thank my girlfriend Arpita. Words cannot describe how you have changed my life. This thesis would not have been possible without your love and motivation. I hope going forward I can do the same for you as we begin our life together.

Harshavardhan Vijaya Kumar
Delft, September 2021

1

INTRODUCTION

Air travel has been on the rise since the beginning of the 20th century but, never before has the industry had to face the unique situation it faces at this moment. There is a predicted increase in demand for air travel and a simultaneous increase in fuel price [44]. These factors coupled with the need to reduce carbon footprints make lightweight solutions that are quick to manufacture an utmost necessity to stay relevant in the industry. Additionally, the COVID-19 pandemic has resulted in a €22.2 billion net loss for aviation industry in Europe [7]. This leads to the requirement for the next decade of commercial aircraft products to be cost-effective for the airlines and the manufacturers.

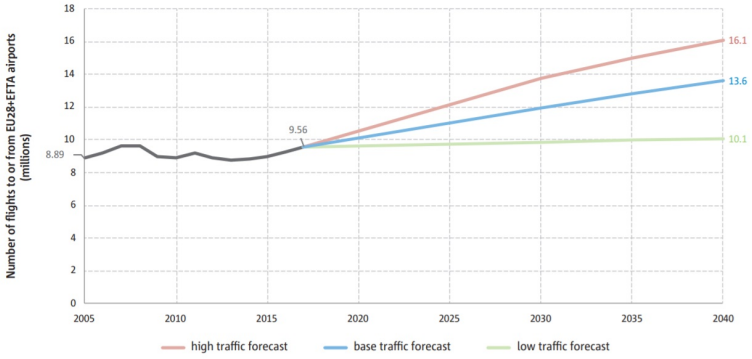

(a) Travel prediction for 2040

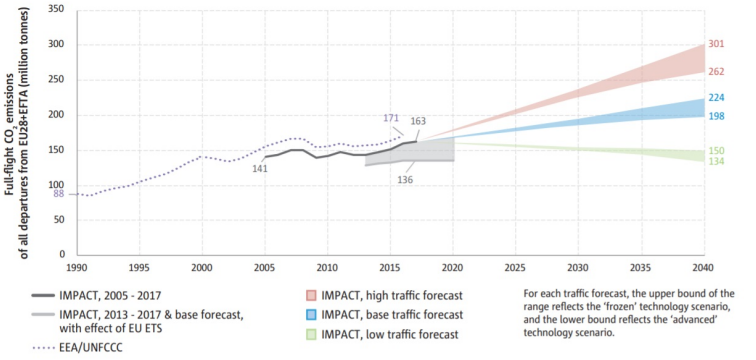

(b) Carbon emission prediction for 2040

Figure 1.1: Extrapolated predictions made by the European Aviation Safety Agency [44].

In the past, the most crucial change introduced to aircraft structures to reduce weight and improve efficiency was through the employment of composite materials. Boeing introduced the first commercial aircraft with close to 50% use of composite materials in their 787 series nearly a decade ago [4]. Since then composite structures have been employed throughout the aircraft in various applications, both on the exterior and the interior. However, the overall design philosophies have remained the same. The essential task being tailoring the material, thickness, and shape with a chosen design architecture.

Topology optimization(TO) offers an advanced designing scheme that can identify optimized design architectures (or topologies) for a given material and loading condition. Its most notable application in the aerospace industry is the optimization of the leading edge ribs of the Airbus A380 [64], where a 500kg weight alleviation was achieved as compared to its previous design. TO identifies both essential and redundant material simultaneously throughout the domain, hence extracting the most suitable material distribution. Typically applied to primary structures which are largely enclosed, the usage

of topology optimization into secondary structures has not been significantly explored. If proven to be capable, this could offer a new avenue for new designs as well as noticeable weight loss.

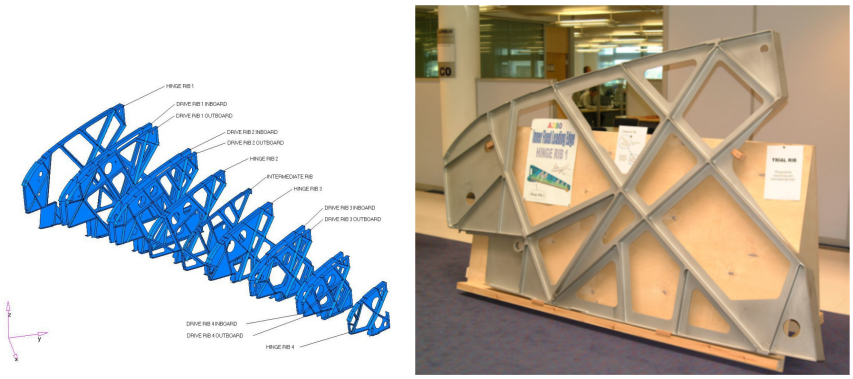

Figure 1.2: Airbus A380 leading edge ribs designed through topology optimization [64].

Cabin structures encompass a wide range of structures within the interior of the aircraft and have been key employers of composite material. Often overlooked due to their deceptively mundane application, cabin structures are vital in the functioning of any passenger aircraft and are required to sustain a wide range of requirements: structural as well as functional. They are also silent contributors to the overall weight of any aircraft. However, their essential configuration and architecture have largely remained unchanged. Recently, AIRBUS illustrated the capacity for design advancements in cabin structures through the development of an unorthodox truss like architecture to replace a panel-based design for a partition wall. This new design displayed a significant increase in performance as well as reduced weight by 50%.

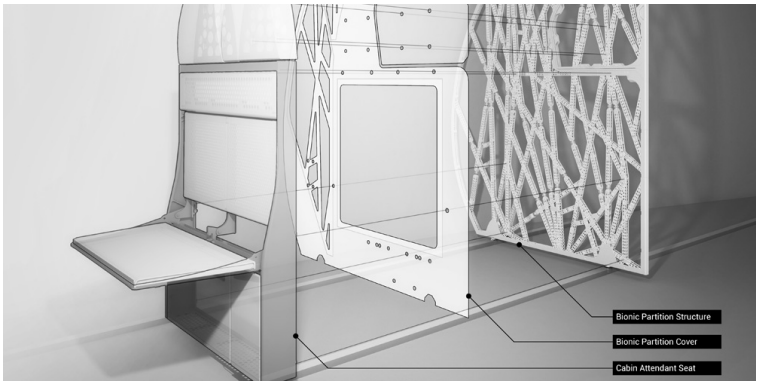

Figure 1.3: Bionic Partition developed by AIRBUS (Nagy et al. [84])

Therefore, with the need for reinvention of cabin structures and possible scope for improvements, TO is a suited design and optimization strategy worthy of exploration. Nonetheless, while topology optimization is a powerful tool, unlike the generous design domain offered by primary structures like aircraft ribs, cabin structures i.e galleys are panel-based and complex in architecture and the generated design is to be operative/functional for daily use. Thus, the design domain is limited in both its scope as well as its space. This exploration of the application of topology optimization on an unorthodox structure as a galley formulates the first research goal:

Can topology optimization be employed on a galley structure? If yes, how can a suitable/practical structure be generated?

Although the use of TO offers weight savings, from a manufacturing and maintenance perspective, complex structures realized as monoliths increase the direct manufacturing costs as well as auxiliary maintenance and deployment costs. Therefore, the one-piece structure provided by TO is to be divided into suitable pieces so as to enhance manufacturability. This allows us to retain the optimized structure provided by topology optimization and regain the additional costs. Additionally, if the extracted parts exhibit similarity, this could allow for an additional scope for reduction in manufacturing costs, ease of maintenance and repair as well as lower certification and development costs.

This exploration for identification of a modular structure within TO solutions forms the second research goal:

How can a topology optimized structure (galley) be suitably modularized into simple modules?

In the following chapters, TO is employed on the G5 galley provided by SAFRAN-Cabins. The requirements provided by EASA and the aircraft requirements provided by AIRBUS are suitably modeled and implemented within the TO tool to generate an optimized structure of the same weight as the current composite structure. In this work a commercial tool: TOSCA-ABAQUS is employed for modeling and optimization. Following which a Legendre image moment matching-based modularization strategy is developed and investigated in its capability to identify similar width bars within the TO solution. Based on the investigation, a fragmented matching followed by a post-processing pipeline is proposed to reconstruct a TO solution into a truss/frame like structure. This methodology is investigated on TO solutions from literature and to finally conclude, employed on the optimized G5 galley.

The outline for the thesis is as follows: Firstly in Chapter 2, the modeling and analysis methodology applied to currently assess the galley structure will be briefly explained. The requirements of the galley for certification and aircraft integration is briefly described. In Chapter 3, the basis on which TO functions is outlined with the analytical formulation for the minimum compliance problem and the material penalization strategy.

A survey of the implementations of constraints on design and geometry with additional details on the numerical instabilities common to TO is described as well. Chapter 4 comprises the details on the modeling of the galley for TO as well as the subsequent TO investigations and their results. Chapter 5 comprises of previous investigations into the influence of modularity on performance and cost in literature as well as brief discussion into methods employed to process TO structures for manufacturing. Chapter 6 describes the analytical basis for the Legendre moments and investigates the moment matching characteristics and the required adaptation to obtain relevant results from the bar matching algorithm. Chapter 7 describes a modified fragmented-bar matching methodology, with investigations on case studies from literature as well as implementation on the topology optimized galley panels.

2

GALLEY DESIGN AND CERTIFICATION

This chapter provides an overview of the cabin structure chosen to be optimized along with its necessary certification and employment requirements. These requirements currently utilized for the design of the galley will be subsequently translated into suitable objectives and constraints for TO. Section 2.2 describes the product-specific regulations and customer requirements followed by Section 2.3 comprising of the industry-approved methodology for the modeling and analysis of the structure.

2.1. GALLEY STRUCTURES

Aircraft structures are often romanticized through wing boxes with complex ribs and spar architectures due to this one of the most vital structures which fulfill the passenger requirements firsthand is overlooked: Cabin Structures. Cabin structures although categorized as secondary structures are vital in the safe and functional operation of any passenger aircraft. Cabin structures encompass all elements within the passenger and crew area such as galleys, luggage storage, lavatories, and seats. Of these, a structure that grabs the attention of any passenger as you enter the aircraft is the galley structure. galleys are shelf-like compartments that are used for various purposes including heating food as well as storage of equipment and trolleys.

The G5 galley is one of the largest and most versatile cabin products developed by SAFRAN-Cabins and will be the body of focus for this project. Capable of containing 7 fully equipped trolleys and 4 ovens, the G5 is truly a workhorse. Figure 2.1 illustrates the panel-based architecture employed in the G5 structure and the various appliances distributed throughout all its compartments.

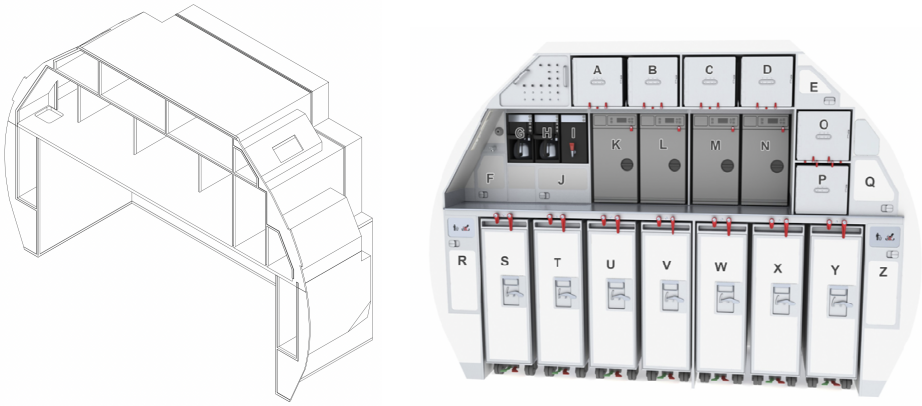

(a) galley iso-view

(b) Appliances and trolleys

Figure 2.1: G5 galley

It is to be noted that the G5 itself is a flexible product and can be adapted to the customer requirements. This can include an assortment of appliances and configurations. The specific model considered for investigation during the project is the SA ACP unit with a trolley divider(non-chilled) to be employed in the A320.

Although straightforward in its application, it is vital that the galley satisfies stringent safety requirements for aviation safety. Outlined by the European aviation safety agency(EASA) [43], these requirements include a wide range of specifications from material selection to emergency landing requirements. Additionally, the aircraft limitations stipulated by AIRBUS allow to incorporate operational requirements.

2.2. GALLEY REQUIREMENTS

Specified by the EASA, the CS-25 certification specification encompasses the certification requirements of large air crafts. Of the myriad of safety requirements the certification loading for the galley is based on the emergency landing requirements. The ultimate inertia forces acting individually and relative to the surrounding structure are as tabulated in Table 2.1. These requirements are the minimum requirements for the safety of the passengers, but maximum operating forces are to be taken into consideration as well, these are specific to the aircraft and operational parameters. To satisfy operational as well as emergency requirements, the maximum possible loading is utilized for the design of the structure.

Load factors (acceleration)				
Load Direction	Emergency Landing Load Factors CS-25 Requirements	Emergency Landing Load Factors JAR 25.561 Ch.1	Max. Flight and Landing Loads A318, A319, A320, A321	Max. Load Factors
Upward	3.0g	2.0g	AB_{UP}	L_{UP}
Forward	9.0g	9.0g	AB_{FWD}	L_{FWD}
Side-ward	4.0g	1.5g	AB_{LR}	$L_{L,R}$
Downward	6.0g	4.5g	AB_{DWN}	L_{DWN}
Rearward	1.5g	1.5g	AB_{AFT}	L_{AFT}

Table 2.1: Ultimate load factors

Although the galley is designed to sustain loads, it is essential that the interface with the aircraft itself sustain the load transfer as well. The galley is attached to a set of hard-point floor attachments. Each attachment point has distinct load-carrying capabilities in all directions. Some points also have no load-carrying abilities in a certain direction (flutter point attachments). These limitations dictate the limitations of design variables for the loading requirements dictated by the ultimate load factors. Thus, the load transfer to the aircraft is to be directed or redirected appropriately to prevent any separation. The specific limitations are tabulated in Table 2.2.

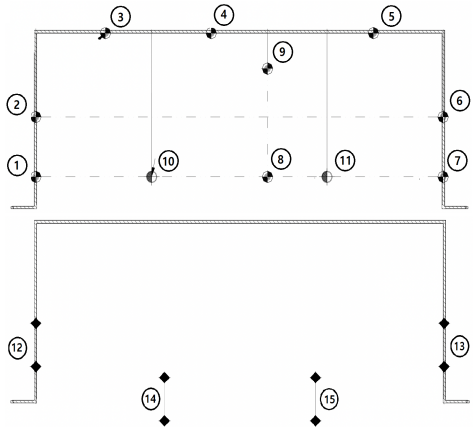

Figure 2.2: Top and bottom attachments

Table 2.2: Interface limits

Attachment point i	Direction	Allowable (N)
1,3,4, 5,7, 8,9	X	$\pm RX_{1,3,4,5,6,8,9}$
	Y	$\pm RY_{1,3,4,5,6,8,9}$
	Z	$\pm RZ_{1,3,4,5,6,8,9}$
2,6	X	$\pm RX_{2,6}$
	Y	$\pm RY_{2,6}$
	Z	$\pm RZ_{2,6}$
10,11	X	$\pm RX_{10,11}$
	Y	$\pm RY_{10,11}$
	Z	$\pm RZ_{10,11}$
12,13	X	$\pm RX_{12,13}$
	Y	$\pm RY_{12,13}$
	Z	$\pm RZ_{12,13}$
14,15	X	$\pm RX_{14,15}$
	Y	$\pm RY_{14,15}$
	Z	$\pm RZ_{14,15}$

2.3. GALLEY MODELING AND ANALYSIS

The certified modeling and analysis tool used in-house utilizes the commercial tool NX/NASTRAN (version 8.0) with modeling and post-processing performed on FEMAP (version 10.3). The software uses the Finite Element Method to calculate deflections, stresses, and reaction loads of the galley model.

- Elements - The conventional galley utilizes a multi-layered composite as the basic material for all the panels. These are modeled using first ordered quadrilateral and triangular elements. The element is build up out of 3 layers: 2 face sheets and 1 core. The insert weights are modeled with mass elements, located at the center of gravity, which is attached to the structure with RBE3 elements.

- Loading - All insert weights are modeled as nodal forces at their tie-down or restraint points in the forward load case. In the case of doors, the load is modeled as a distributed line load at the hinge side of the door and a nodal force at the latched side. In all other cases, the inserts are modeled as distributed loads. The empty structure weight is modeled through an acceleration force.

- Boundary conditions - All fixing points of the unit in the aircraft are considered stiff (no moment transfer). Spring rates of $K_{x,y}$ DaN/mm in the x-direction and y-direction and K_z DaN/mm in the vertical (z) direction are used to simulate the stiffness of aircraft attachments. (Stiffness rates are standard values provided by Airbus).

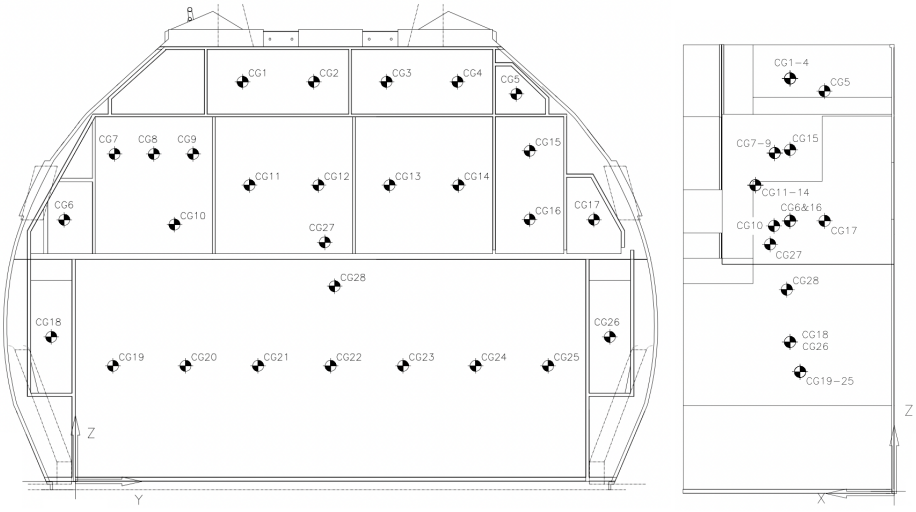

(a) AFT view

(b) side view

Figure 2.3: CG positions where loads are applied

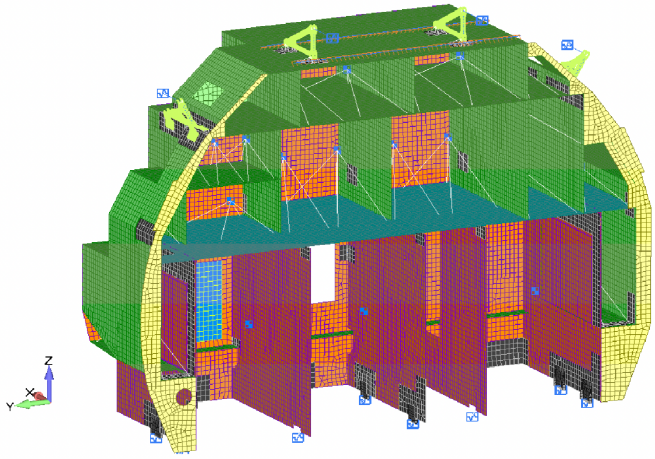

Figure 2.4: CG coupled to tie down points

CG no.	Item	Weight (kg)	X (mm)	Y (mm)	Z (mm)
1	A	w_A	x_A	y_A	z_A
2	B	w_B	x_B	y_B	z_B
3	C	w_C	x_C	y_C	z_C
4	D	w_D	x_D	y_D	z_D
5	E	w_E	x_E	y_E	z_E
6	F	w_F	x_F	y_F	z_F
7	G	w_G	x_G	y_G	z_G
8	H	w_H	x_H	y_H	z_H
9	I	w_I	x_I	y_I	z_I
10	J	w_J	x_J	y_J	z_J
11	K	w_K	x_K	y_K	z_K
12	L	w_L	x_L	y_L	z_L
13	M	w_M	x_M	y_M	z_M
14	N	w_N	x_N	y_N	z_N
15	O	w_O	x_O	y_O	z_O
16	P	w_P	x_P	y_P	z_P
17	Q	w_Q	x_Q	y_Q	z_Q
18	R	w_R	x_R	y_R	z_R
19	S	w_S	x_S	y_S	z_S
20	T	w_T	x_T	y_T	z_T
21	U	w_U	x_U	y_U	z_U
22	V	w_V	x_V	y_V	z_V
23	W	w_W	x_W	y_W	z_W
24	X	w_X	x_X	y_X	z_X
25	Y	w_Y	x_Y	y_Y	z_Y
26	Z	w_Z	x_Z	y_Z	z_Z

Table 2.3: Centers of gravity of all G5 galley elements

3

TOPOLOGY OPTIMIZATION

Before a galley can be optimized, it is essential to understand the basis upon which Topology optimization (TO) functions. This chapter presents a brief review of structural topology optimization beginning with its computational framework in Section 3.1. This is followed followed by the implementations of relevant design and performance constraints proposed and employed in literature in Section 3.1.2 and 3.1.3. Section 3.2 describes the numerical anomalies and instabilities frequently observed in TO as well as the corresponding alleviation strategies. Since the galley has to satisfy multiple loading requirements, Section 3.4 explores commonly employed approaches for multi-objective optimization. Section 3.5 concludes with a brief exploration of commonly employed topology optimization tools as well as a comparison of accessible packages.

3.1. THE COMPLIANCE MINIMIZATION FORMULATION

Introduced by Bendsøe and Kikuchi, topology optimization is in essence a material distribution problem. Early versions utilized an artificial composite material (foam-like) whose local elastic properties are estimated as a function of its local density. By optimizing the compliance with respect to the local density, a globally optimized shape and topology is obtained as illustrated in Figure 3.1.

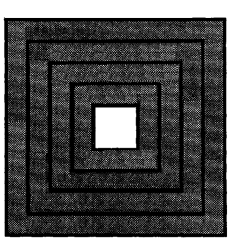

(a) Artificial square void foam

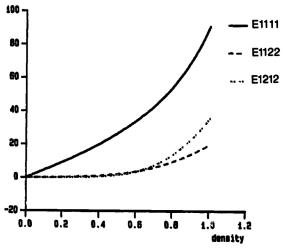

(b) Interpolated Elastic Modulii

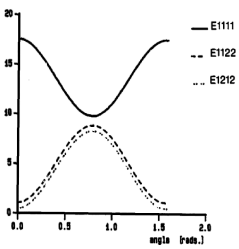

(c) Elastic Modulli vs angle.

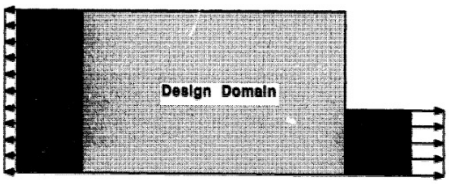

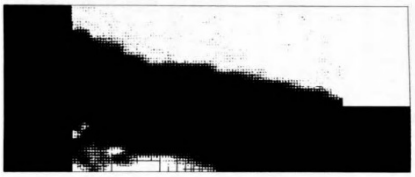

(d) Optimal topology for minimum compliance with volume constraint 64%.

Figure 3.1: Structural optimization using local cell density optimization (Bendsøe and Kikuchi [21]).

The minimum compliance optimization problem takes the form:

$$\begin{aligned} \text{minimize}: \quad & L(v) = \int_{\Omega} f \cdot v dx + \int_{\Gamma_T} t \cdot v ds \\ \text{s.t:} \quad & E_{ijkl} \in U_{ad} \\ \text{subject to}: \quad & a_E(u,v) = L(v), v \in U, \text{ design constraints.} \\ \text{where}: \quad & a_{\mathrm{E}}(u,v) = \int_{\Omega} E_{ijkl} \varepsilon_{kl}(u) \varepsilon_{ij}(v) \mathrm{d}x \end{aligned} \tag{3.1}$$

Where U_{ad} is the kinematically admissible deformation field and design constraints can include limitations on stress, strain, natural frequency, etc. E_{ijkl} is the local elastic tensor for the material. In a general material distribution problem E_{ijkl} can be used for regions with material and 0 elsewhere. But this form of discrete optimization cannot be solved using gradient descent methodologies. To convert the problem to a continuous system, interpolation functions are employed to model the material property between the solid and void states.

$$E_{ijkl} = I_{\Omega^{mat}} E^0_{ijkl} \tag{3.2}$$

$$I(x) = \begin{cases} 1 & \text{if } x \in \Omega^{mat} \\ 0 & \text{if } x \in \Omega < \Omega^{mat} \end{cases} \tag{3.3}$$

The original method employed homogenization to estimate the material elasticity as a function of a square cell pseudo-density ρ[1] and orientation (shown in 3.1). This is coupled with a resource constraint (V_c) i.e. the volume of the structure, resulting in the typical topology optimization problem in its discretized form as stated in (3.4).

$$\begin{aligned} \min_{\rho}: \quad & \mathbf{f}^T\mathbf{u}) \\ \text{subject to}: \quad & \mathbf{K}(E_e)\,\mathbf{u} = \mathbf{f} \\ & E_e = f\left(\rho\right) \\ \sum_V \rho\Delta v < V_c, \quad & 0 \le \rho \le 1 \end{aligned} \tag{3.4}$$

3.1.1. SIMP AND OTHER DENSITY-BASED INTERPOLATION METHODS

After the pioneering work by Bendsøe and Kikuchi, further work by Bendsøe and Yang and Chuang employed power-law based empirical expressions to obtain the intermediate density properties of the material and eventually Rozvany et al. coined what is known today as the SIMP [2] method. The empirical expression for the material elasticity with respect to the TO density of the material is given by $E = E_0\rho^p$. The parameter p is the penalization parameter that pushes the design variables towards 0 and 1. The magnitude of p decides the influence of density on the stiffness of the material. As p is increased, the material's softening response to having voids increases. For $p = 1$, the model is analogous to a plate thickness sizing model, and as p is increased to 2-3 the model resembles a rule of mixtures approximation as illustrated in Figure 3.2.

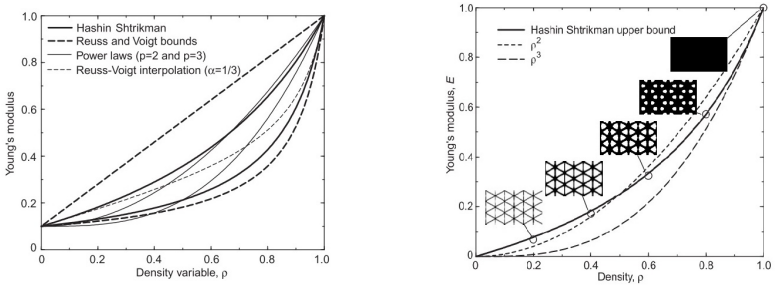

(a) Material interpolation models commonly used in density-based topology optimization[19]

(b) Comparison of power-law based material with Hashin Shtrickman material model

Figure 3.2: Material interpolation models

[1] $\rho = 1$ a solid square cell, $\rho = 0$ implies an empty cell (no material) and intermediate values ($0 \le \rho \le 1$) are for foam like cells with intermediate void sizes.

[2] SIMP - Solid Isotropic Material with Penalization

Penalizing the stiffness results in a material cost to benefit problem where the material is used only in locations where the stiffness is required and at locations where the material is not required the density drop results in an exponential drop in stiffness and as the problem converges, at lower densities, the cost of material overtakes the effective stiffness offered and hence the material is entirely eliminated. At higher densities for a small increase in cost, an exponential increase in stiffness leads to fully solid material deposition. The SIMP model has been the most widely used in topology optimization and has been used to formulate simple yet powerful frameworks, one of the most famous being the 99-line topology optimization code written in MATLAB [97].

It must be noted, the SIMP method assumes an isotropic-Elasticity(E) and TO-density(ρ) relationship. But, the Poisson's ratio is assumed constant (independent of density) in most applications [119] [19]. Yet, the method has still shown to be superior to the homogenization method (where the Poisson's ratio varies with density). Zhou and Rozvany illustrated the SIMP method's capability by comparison to the homogenization method as well as the analytical solution, as seen in Figure 3.3 for an MBB[3] beam.

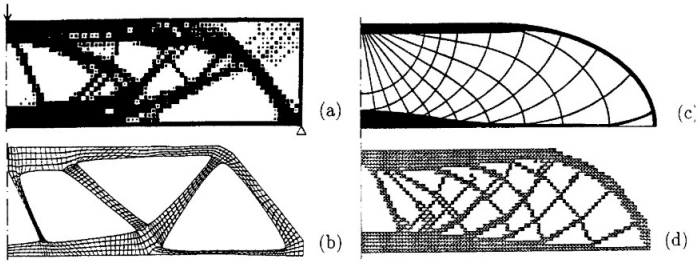

Figure 3.3: (a) MBB beam optimized using the homogenization method, (b) A modified second stage method ,(c) Analytical optimal result obtained using COC layout solutions, (d) MBB Beam optimized using the SIMP method (Zhou and Rozvany [124]).

Other material interpolation models have been proposed as an alternative to SIMP. A few of the prominent methods are listed here:

1. RAMP - *Rational Material Penalization* - Proposed as an alternative to the SIMP model for its capability to increase the convexity (In comparison to the SIMP model) of the problem [103]. The parameter q is analogous to the penalization parameter p in the SIMP model. E_0 here represents the lower threshold and ΔE represents the difference between the upper and lower limits of the stiffness.

$$E_q(\rho) = E_0 + \frac{\rho}{1+q(1-\rho)}\Delta E \tag{3.5}$$

2. SINH - Based on the hyperbolic sine function, this method was proposed for use in cases where the SIMP model results in largely grey areas instead of solid-void

[3] MBB - Messerschmitt-Bölkow-Blohm, a German aerospace company whose famous patent for an optimized beam structure is used as a standard design problem to assess topology optimization frameworks

designs [28]. The method instead of penalizing the material stiffness penalizes material volume with respect to the design variable ρ. The penalization of the element volume using η_2, achieves the same effect as penalizing element stiffness using ρ^p. Hence resulting in the redistribution of intermediate density material.

$$\begin{aligned} \eta_1 &= \hat{\eta}_1(\rho) = \rho \text{ and} \\ \eta_2 &= \hat{\eta}_2(\rho) = 1 - \frac{\sinh(p(1-\rho))}{\sinh(p)} \end{aligned} \tag{3.6}$$

3. Logistic function - A material interpolation model based on the logistic regression analysis function is capable of penalizing low-density elements and enhancing high dense elements, hence achieving more solid - void designs[38]. Here a represents the penalization parameter and $-1/m$ represents the lower threshold.

$$E_i = \frac{e^{-a/m+a\rho}}{1+e^{-a/m+a\rho}} E_0 \tag{3.7}$$

Apart from these artificial models, traditional models such as the Hashin Shtrickman model, Voigt, and Reuss - Voigt model have been frequently used [19]. But in these cases, the focus has been to design viable cellular material-based structure topology.

Much of the versatility of topology optimization is a result of its ability to be applied to any discretized system and the integration of design constraints within the optimization routine. Hence, this allows its employment in non-structural domains such as thermal engineering [75][48], acoustical engineering [39], electronics design [85] and even multi-physics applications [121].

TO without design constraints can be used as an initial tool for design. The resource/volume constraint described in Section 3.1 satisfies typical demands to generate lightweight structures. But, from a manufacturing perspective, not all structures generated in this fashion can be realized. This leads to the requirement of the design space to be limited to achievable structures. Furthermore, not all such topologies generated can sustain the applications it is optimized for. This leads to the requirement of performance constraints, to allow for direct integration of material and structural limitations. Each of these is addressed by suitable design constraints.

3.1.2. DESIGN GEOMETRY CONSTRAINTS

Design constraints on the optimization problem allow for control of the design features such as the body dimensions and hole sizes. The use of such constraints not only serves a practical purpose but also allows to constraint the solution in some cases. The practical limitations can include material deposition limits in semiconductor manufacturing (MEMS) [100] or tooling limitations on machined structures.

PERIMETER CONSTRAINT

One of the first methods to impose geometrical constraints on the design was through upper limits on the perimeter of the structure [51]. Although initially posed as a solution to non-unique solutions (which will be elaborated in section 3.2), the bound placed by the perimeter displayed a reduction of the geometric complexities of the obtained solutions. The only drawback is that the perimeter and the scaling of the features of the design did not exhibit a clear-closed form relationship other than a clear increase in feature sizes as the upper limit of the perimeter is reduced as illustrated in Figure 3.4. The reduction in fine features with the perimeter constraint is accompanied by an increase in the compliance of the structure. This can be largely attributed to the comparatively localized drop in stiffness in the case of smaller holes and cutouts as compared to the global drop in stiffness in the case of large cutouts. But from a manufacturing perspective, microscopic voids are not practically realizable. Therefore, the drop in stiffness is counteracted with the relaxation of manufacturing complexity. Thus, the perimeter constraint allows to quantify the manufacturing complexity to some extent [50].

Figure 3.4: The MBB Problem constrained with a perimeter constraint of (a)30L , (b) 24L and (c) 22L. (Haber et al. [51])

MINIMUM LENGTH SCALE

The minimum length scaling fixes a lower limit on the finest features of the design. A lower limit on the feature sizes not only allows for manufacturing considerations but also computational by-products such as single-node connections. This is especially common in compliant mechanism design [90] as well as minimum compliance problems with low material volume fraction limitations.

The most common method for applying a minimum length scale is through mesh independent filters [29]. The method utilizes mesh independent filtering to achieve a radial smearing of the density about each pixel which allows for minimum length scaling. A modification of this methodology to use nodal design variables instead of using element density variables has shown promise as well [49]. However, heavy-side filter-based projection methods that can provide scaling on both solids or voids have been shown to not always provide manufacturable designs [114]. Local gradient constraints have also shown to be effective in providing a minimum length scale [56], although their initial intended purpose was to counteract checkerboarding effects. One of the other methods which have gained prominence is the monotonicity-based minimum length scale (MOLE) which can be used in structured regular grids [90], where the monotonicity in the coordinate and diagonal directions are studied for a span equal to the minimum length desired. The function measuring the monotonicity is integrated over the domain and is used as a constraint on the problem. A more recent and more complex [69] implementation is proposed by Zhou et al. using a three-field formulation (design, filtered,

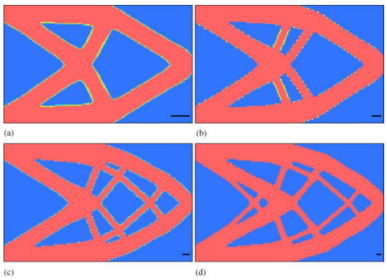

(a) Results obtained using minimum length scale imposition using mesh independent filters for various minimum member sizes (a) d_{min} = 4.0 ,(b) d_{min} = 2.0, (c)d_{min}=1.5 and (d) d_{min}=1.0 (Guest et al. [49]).

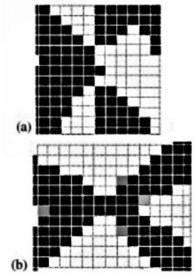

(b) A minimum length scale imposed using the MOLE method (b), eliminating single node connections (a) in compliant mechanism design (Poulsen [90]).

Figure 3.5: Minimum length scaling.

projected) where the filtered design variables impose length scaling on the solid region and the projected variables on the void regions [125].

MAXIMUM LENGTH SCALE

Maximum length scaling limits the material deposition at a particular region in the domain, this allows limiting feature dimensions within the domain. Coupled with the minimum length scaling, feature sizes in the domain can be standardized to obtain more intuitively realizable structures with standardized parts. This was achieved by a narrow-band filtering approach used by Lazarov and Wang which avoids both large as well as small members, and the limit is posed both on the solid as well as void regions [68]. However, filtering in the frequency domain does not allow for direct control in the density domain. To achieve a direct control in the density domain, morphological filters have proven to be superior as they allow for modification of both solid and void regions independently. Hence, achieving separate solid and void length scaling as illustrated in Figure 3.7. An explicit method to impose general scaling in SIMP methods was proposed by Zhang et al.. The method is capable of providing local control of the sizing by measuring the features sizes with respect to a so-called structural skeleton, which is often used in image processing [92] [11]. By measuring both minimum and maximum lengths with respect to the structural skeleton, a custom banded scaling is possible as illustrated in Figure 3.8.

3.1.3. DESIGN PERFORMANCE CONSTRAINTS

Topology optimized structures often fall short from a strength perspective when low volume fractions are considered. The reason being that although the obtained structure exhibits an optimal objective (say compliance), the structure is incapable of carrying loads without failure or collapsing (buckling). Hence, to achieve optimal structures which do not fail for the applied loads, a suitable constraint is required. Common performance

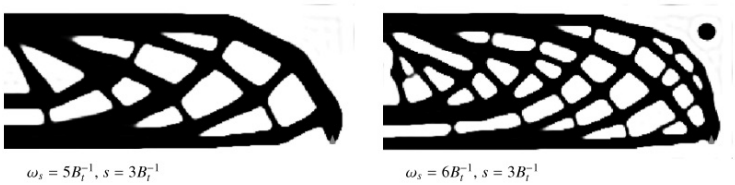

Figure 3.6: Maximum length scaling imposed using bandpass filters. The w_S represents the frequency below which the densities are set to 0 leading to larger feature sizes. As w_S is increased the feature sizes generated reduce. (Lazarov and Wang [68])

Figure 3.7: Maximum length scaling imposed morphological operations. Case 1: Maximum length scaling on both phases and Case 2: Scaling only on the solid phase. (Lazarov and Wang[68])

measures utilized include stress constraints and buckling constraints for static loading and eigenvalue constraints for dynamic considerations.

STRESS CONSTRAINTS

In most cases, topology optimization is utilized in cases where the number of design variables is much larger than the number of design responses since this allows for an efficient adjoint formulation. However, applying stress constraints directly results in an inefficient formulation since the location of the critical stress is not previously known leading to the addition of a number of constraints equal to the number of design variables. Furthermore, since in topology optimization, the elements are allowed to vanish, this leads to local optima or more often called the "singularity phenomena" which can be attributed to the retaining of constraints pertinent to elements that have vanished i.e $\rho \approx 0$ causing inaccessible solution space. This makes stress-constrained topology optimization a complicated endeavor but never-the-less an utmost necessity for capable structural solutions.

Rozvany and Birker described the nature of the global solution of any n-dimensional singular optimization problem as the solution at the tip of one of many k-dimensional hyper-plane segments or 'spokes' where few of the n dimensions vanish i.e $k < n$ [95][93]. This is illustrated in Figure 3.9, where the global optimal lies at the tip of region FD. The concept of singularities leading to local optima was shown to be alleviated if truss members, as well as their design dependant constraint, were allowed to vanish [106] as this eliminates the truncation caused at the connection points between the spokes and the completely feasible solution space i.e represented by point D in Figure 3.9.

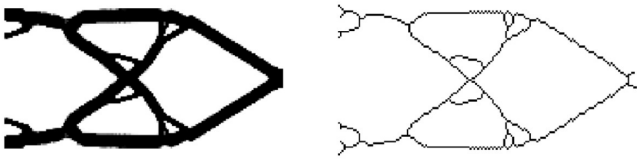

Figure 3.8: Maximum and minimum scaling imposed on a short beam problem, and the corresponding structural skeleton. (Zhang et al.[123])

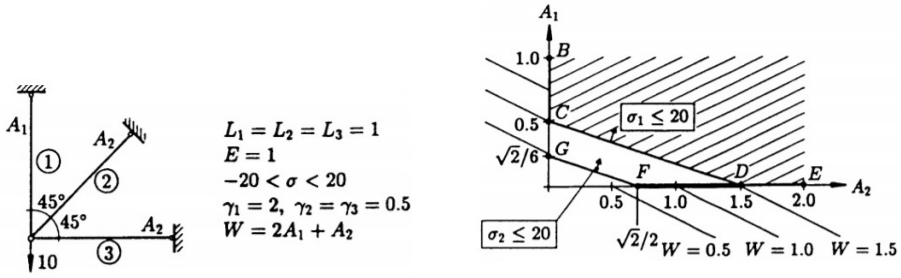

(a) Truss problem with singular solution.

(b) The region FD is inaccessible. The global optimal F is inaccessible since traditional search algorithms stop at D

Figure 3.9: Singularity phenomenon illustration (Kirsch[62]).

A common approach to enable access to the global optima and eliminate the discontinuity caused due to the vanishing members is through the use of smooth envelope functions which relax the stress constraints posed on the variables [93]. Cheng and Guo recommended a method that introduces an ϵ parameter to the constraints to enlarge the feasible domain. This relaxation parameter ϵ can be incorporated through various strategies [32][42][46][40] , the most straightforward is through its inclusion as a tolerance or difference in the original constraints as stated in Equation 3.8.

$$\tilde{g}_j = \bar{g}_j - \varepsilon \leq 0 \tag{3.8}$$

Another common method used is the $q-p$ approach formulated from the microscopic stress perspective. It is important to note that although the stiffness is modeled as a piece-wise distribution in topology optimization when the density is modeled varying from solid(1) to void(0), it is more logical to assume the intermediate material structure to be a cellular material. In such a case, computing stress magnitudes from the averaged elastic properties do not reflect the actual stress experienced in the cellular material, the epsilon relaxation method does not take into consideration this effect. Hence to modify the stress parameter to depict the stress concentration experienced in the cellular material as the density is decreased, a microscopic stress formulation is utilized [27]. Represented in Equation 3.9, p represents the penalization parameter commonly used in the SIMP formulation and q the density exponential which decides the extent of inverse correlation between the stress amplification and the density. The relationship between

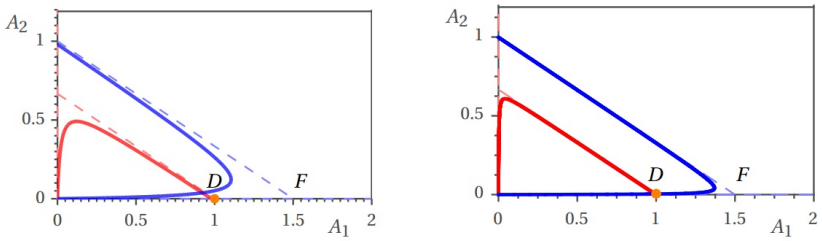

(a) $\varepsilon = 0.01$ (b) $\varepsilon = 0.001$

Figure 3.10: Modified design space with the epsilon relaxation (Verbart et al.[112]).

the parameters can be obtained using the requirements for the constraints to vanish at 0 density as well as the requirement for non-finite stress at 0 density i.e. $p > q$. Figure 3.11 represents the broadening of the solution space using the $q - p$ relaxation strategy.

$$\tilde{g}_j = \frac{\rho_j^{\varepsilon_{qp}} |\boldsymbol{\sigma}_j|}{\sigma_{\text{lim}}} - 1 \leq 0, \quad \text{where } \varepsilon_{qp} = p - q > 0 \tag{3.9}$$

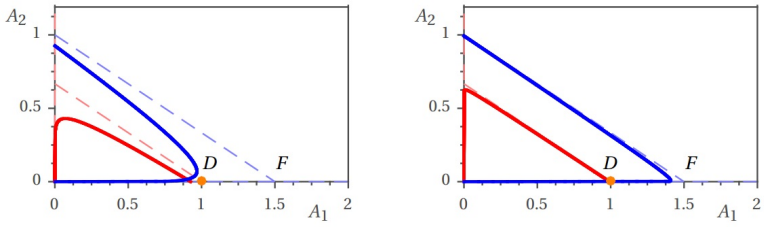

(a) $\varepsilon_{qp} = 0.1$ (b) $\varepsilon_{qp} = 0.01$

Figure 3.11: Modified design space using the qp approach (Verbart et al.[112]).

AGGREGATION

Topology optimization is already a computationally expensive operation. Each optimization iteration requires a finite element solution as well as a design sensitivity computation with respect to each element in the discretized domain. In cases where fine FEM models are used for high-resolution structural solutions, the computational expense is further increased. When a large number of local stress constraints are considered, additional computation is added to the problem. The most common method to compensate for this added expense is to utilize an aggregation function that combines the local constraints in the problem to a single constraint or a set of localized constraints.

The most commonly used aggregation functions are the Kreisselmeier-Steinhauser function, P-norm, and P-mean. Each provides a unitary and continuous function as a replacement to multiple stress variables as well as eliminates non-differentiable points present at points where multiple maximum stress points can exist. Figure 3.12 illustrates the aggregation of two functions f_1 and f_2.

- P-norm [118][53]

$$\Psi_{\text{PN}} = \left(\sum_{e=1}^{N} f_e^P \right)^{1/P} \tag{3.10}$$

- P-mean [41]

$$\Psi_{\text{PM}} = \left(\frac{1}{N} \sum_{e=1}^{N} f_e^P \right)^{1/P} \tag{3.11}$$

- Kreisselmeier-Steinhauser [118]

$$\Psi_{\text{KS}}^{\text{U}} = \frac{1}{P} \ln \left(\sum_{e=1}^{N} e^{P f_e} \right) \tag{3.12}$$

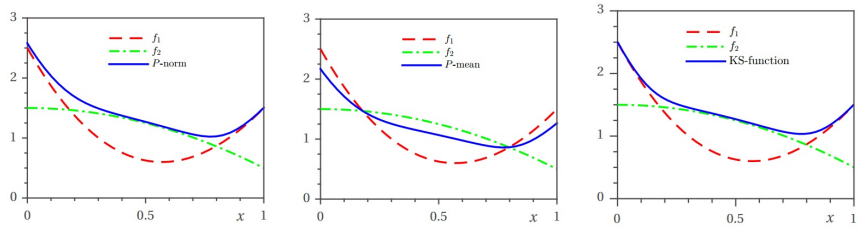

(a) P-norm aggregation applied to function f_1 and f_2

(b) P-mean aggregation applied to function f_1 and f_2

(c) KS norm aggregation applied to function f_1 and f_2

Figure 3.12: Frequently used aggregation functions. (Verbart et al.[112]).

The P-norm is preferred when peak stresses are experienced whereas P-mean is preferred when a largely uniform stress distribution is present. The aggregation functions demonstrate an asymptotic behavior tending to the maximum operator as the aggregation parameter is increased, hence it may seem logical to utilize large aggregation parameters to obtain more accurate sensitivities. However, it has been shown that the resulting large gradients induce numerical instabilities, and hence it is advisable to use moderately high values to ensure smooth aggregate functions and stable numerical convergence.

It must be noted that as the number of distinct constraints increases the accuracy of the aggregation function drops, hence such methods are not preferred for large (very fine) problems. Therefore, although it may seem intuitive to aggregate all of the constraints at once, the resulting numerical instabilities can yield oscillating solutions. But

it must be noted that the computational time required for even this large number of iterations is much lesser than the local constraint problem. A middle ground, where a regional aggregation approach is used achieves a good balance between the number of iterations and computational time. In this approach, the design domain is sub-divided into multiple regions and aggregation of constraints is performed locally within each of these regions. Utilizing multiple aggregation regions/functions yields a better representation of the local stress field, as well as the maximum stress in the domain therefore various recommendations for regional aggregation strategies, have been proposed. París et al. suggested a blocked approach where geometrically local cells are grouped [88]. However, to give prominence to the magnitude of stress rather than its geometric location Le et al. recommends the selection of regions so as to increase the difference in the stress experienced by the elements in each region [70]. Additionally, Holmberg et al. suggests the use of regions where the difference in the aggregated stress between regions is minimized [53]. It is to be noted that although division into regions increases the accuracy of the aggregation, the positive effect of the division diminishes past a point of division [70].

3.2. NUMERICAL INSTABILITIES IN TOPOLOGY OPTIMIZATION

Topology optimization for material distribution problems is prone to certain unique complications. To extract feasible and coherent designs, it is essential that these instabilities are addressed. The most prominent of these being checkerboarding and Mesh dependant solutions, as described by Sigmund and Petersson [98].

3.2.1. CHECKERBOARDING

Checkerboarding refers to the occurrence of alternating solid and void elements in the solution obtained (like checkerboards). Checkerboards are a by-product of rough numerical modeling, as shown by Diaz. Quadrilateral elements with 4 nodes exhibit artificially large stiffness due to the low order shape functions. The actual stiffness of such alternate arrangements of materials has actually been proved to be considerably low and almost non-existent [24]. Hence making checkerboards both an incorrect modeling as well as an undesirable design solution. The effective property estimated for periodic material in 2D was shown to be considerably larger when modeled with 4 node elements instead of 9 node elements.[23]. Hence, using 9 node elements completely eliminates the presence of checkerboards. However, the increase in the number of nodes makes the use of 9 node elements computationally expensive. Therefore, alternative filtering strategies are employed in conjunction to low order elements to alleviate checkerboards. These filtering strategies will be explored in Section 3.2.4.

4 node checkerboard properties : $\bar{E}_{1111} = \bar{E}_{2222} = 0.5000, \bar{E}_{1122} = 0.1500, \bar{E}_{1212} = 0.1750$ (3.13)

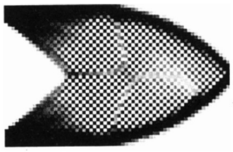

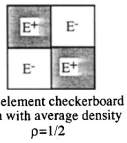

Four element checkerboard patch with average density ρ=1/2

(a) Checker-boarding in TO solutions.

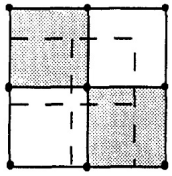

(a) 4-node elements

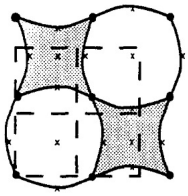

(b) 9-node elements

(b) Difference in response of 4-node and 9-node model of checkerboard

Figure 3.13: Illustration of checkerboarding and artificial stiffness in low order elements. (Diaz[35]).

8 node checkerboard properties : $\bar{E}_{1111} = \bar{E}_{2222} = 0.1720, \bar{E}_{1122} = 0.0941, \bar{E}_{1212} = 0.1159$ (3.14)

3.2.2. MESH DEPENDENCY AND NON-UNIQUENESS

Mesh dependency refers to the variation of the results as the mesh is refined or coarsened. Ideally, any mesh refinement must produce a more detailed description of the boundaries rather than entirely qualitatively different designs. However, in the case of topology optimization, the absence of solutions to the original problem with discrete design values results in a significant variation in the designs for varying mesh sizes [98] as illustrated in Figure 3.14. Mesh dependency is also inherently a possibility in problems with multiple solutions, i.e. non-unique solutions. A very simple example is the design of a bar under tension (without any stress constraints) optimized for reduced material as illustrated in Figure 3.15. The bar itself can either be a single strut or multiple members in parallel and in either case, the stiffness is actually equal (hence multiplicity).

Figure 3.14: Variable solutions obtained for 500 and 5400 element discretization. (Sigmund and Petersson [98]).

Figure 3.15: Illustration of multiple possible solutions for the same problem. (Sigmund and Petersson [98]).

The freedom of the variables to take multiple solutions can be visualized as a by-product of an unconstrained variation. Therefore, to pose a constraint on the solutions and to enforce convergence onto unique solutions, constraints are posed on measures of the density variations.

3.2.3. PERIMETER CONSTRAINT

Previously mentioned in reference to a measure of manufacturing complexity, the perimeter constraint was originally posed as a constraint on the variation of the design variables. The constrained problem is proven to include the optimal solution [12] and to constrain the problem so as to produce mesh independent results [51][47] as illustrated in Figure 3.16.

Figure 3.16: Mesh dependancy alleviation using perimeter constraints. (Haber et al. [51]).

The more mathematically rigorous form of the Perimeter constraint is the norm constraint of the design variables in the Sobolov space. A global gradient constraint is given by equation 3.15.

$$\|\rho\|_{H^1} = \left(\int_\Omega \left(\rho^2 + |\nabla \rho|^2 \right) \mathrm{d}x \right)^{\frac{1}{2}} \leq M \tag{3.15}$$

The local gradient constraint achieves a similar result but results in a 2n/3n increase in the number of constraints hence making the process inefficient. But it is to be noted that the constraint posed on the local gradient almost assures grey designs but significantly reduces checkerboards. The practical implications of Grey designs are elaborated in Section 3.3.

$$\left| \frac{\partial \rho}{\partial x_i} \right| \leq c \tag{3.16}$$

3.2.4. FILTERING

Filtering is typically used in image processing to clean noisy data. Usually utilizing local pixel neighborhood information and intensity variations to modify the image to yield more clear features. A similar approach is utilized to modify design density and design sensitivity to modify the problem to yield a unique and mesh-independent solution.

SENSITIVITY FILTERING

Originally posed as a solution to checkerboarding problems, mesh independent filtering utilizes a local recalculation of the design sensitivities of each element based on a weighted average of the design sensitivities around it [99]. In checkerboard prevention, the neighborhood was limited to a radius of 1 element, but through generalization for larger radii, the method is useful for addressing mesh dependency. The method was initially proposed for modeling bone growth and bone healing and is an excellent representation of how local neighborhood response contributes to the material deposition/elimination rate at a particular location [82]. The filter is represented by equation 3.17. Based on a convolution operation, the local weights are decided based on the distance between the neighboring elements within a certain radius, hence making the sensitivity information a geometrically dependant quantity rather than a mesh dependant quantity. However, models with mesh-dependant sensitivity filtering have been shown to produce good results as well [25].

$$\frac{\widehat{\partial f}}{\partial \rho_k} = \left(\rho_k\right)^{-1} \frac{1}{\sum_{i=1}^{N} \hat{H}_i} \sum_{i=1}^{N} \hat{H}_i \rho_i \frac{\partial f}{\partial \rho_i}$$
$$\hat{H}_i = r_{\min} - \operatorname{dist}(k,i), \quad \{i \in N | \operatorname{dist}(k,i) \leq r_{\min}\} \tag{3.17}$$

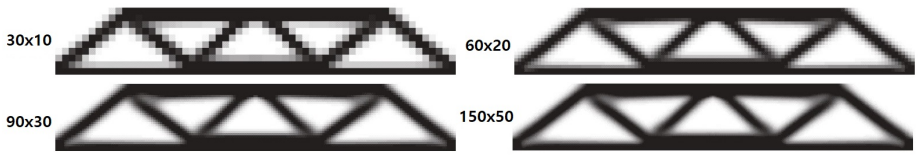

Figure 3.17: Elimination of mesh dependency using Sensitivity filtering (sigmund [99]).

DENSITY FILTERING

The Density filtering approach was first performed by [29] and it is in a sense a discretized convolution with respect to the density [29]. The convolution-based density filtering recalculates the density through a weight-based average over a region around each cell (uniform, conical or exponential), which results in a smoothing of the density (similar to sensitivity filtering) [26].

$$\bar{\rho}(\mathbf{d}) = \sum_j \frac{\omega_j}{\omega} \rho_j$$
$$\omega_j = \max\left(1 - \frac{\left(x_j - x_i\right)^2 + \left(y_j - y_i\right)^2}{r}, 0\right) \tag{3.18}$$
$$\omega = \sum_j \omega_j$$

PDE FILTERING

A fairly new method aims to alleviate a problem in sensitivity and density filtering. The very act of using mesh independent filters requires a search of neighboring elements which is computationally expensive as the mesh size reduces. The PDE filtering approach aims to utilize an implicitly defined filter using the Helmholtz PDE equation [67]. This method is especially efficient when used with very fine meshes and performs well under parallelization [8]. This method is also applicable as both a density filter as well as a sensitivity filter.

$$\begin{gathered}\nabla^{\top}\mathbf{K}_d\nabla\tilde{\rho}+\tilde{\rho}=\rho, \text{ where } \tilde{\rho} \text{ is the filtered density field}\\ f_p(\mathbf{x})=\rho(\mathbf{x})\frac{\partial c}{\partial \rho}\bigg|_{\mathbf{x}}\\ \nabla^{\top}\mathbf{K}_d\nabla\widehat{f_p}+\widehat{f_p}=f_p, \text{ where} \widehat{f_p} \text{is the filtered field}\end{gathered} \tag{3.19}$$

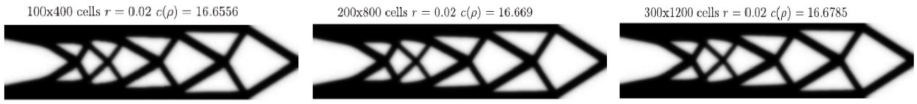

Figure 3.18: Restriction using Helmholltz PDE filter. (Lazarov and Sigmund [67])

It must be noted that the act of filtering was initially just a means to an end and was not deemed logical. The need for rational designs outweighed the search for a rationalization of the operation. However, Sigmund and Maute deduced from a continuum mechanics perspective, the act of filtering in TO can be interpreted as minimizing compliance in a non-local elasticity problem [102]. Hence the act can be deemed more than one of convenience.

3.3. BLACK AND WHITE RESULTS

In the case of application of TO for isotropic materials, the use of any artificial material model employed (such as the SIMP model) is to allow for the local material i.e. ρ to be encouraged towards solid ($\rho = 1$) or voids ($\rho = 0$). However, a frequent byproduct of filtering is grey regions ($0 \leq \rho \leq 1$) in the converged solution. These regions are dependant on the radii used for the filtering operators and results in a requirement for post-processing to obtain black and white results. Analogous to this in image processing, for feature identifications in grey figures, morphological operators are used. The Morphological filters are neighborhood operators which modify the grid values based on the maximum or minimum value in the search region about each cell/voxel. A combination of these filtering techniques has shown to result in Black and White(BW) designs and simultaneously pose minimum feature size constraints[101]. Figure 3.19 illustrates the resulting BW designs through the different morphological operations.

- Erosion : All cells within a structural element are set to the minimum density

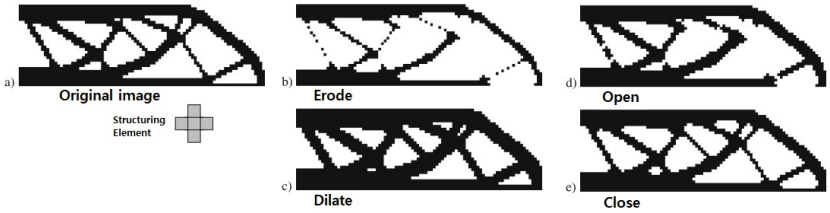

Figure 3.19: Illustration of morphological filtering operations (Sigmund[101]).

within the element.

- Dilation : All cells within a structural element are set to the maximum density within the element.
- Open : Erosion followed by Dilation.
- Close : Dilation followed by Erosion.

In an effort to locate fully B/W designs without filtering, multiple approaches have been proposed. But an interesting method commonly used is the continuation method [98]. A sequential design search is performed through variation of the penalization parameter either in SIMP or RAMP method. The converged result from the previous penalization parameter is used as the starting point for the next, higher penalization parameter. The nature of problems to become mesh dependant is avoided through this method as by varying the penalization parameter sequentially, the tendency to get stuck at a local stationary point (saddle) is avoided and the gradual variation of the penalty parameter allows for more global information to be considered rather than information specific to the current mesh, start design and penalization magnitude. The resulting observation is that the initial grey regions slowly convert to black and white. The method and it's variants have been shown to provide solutions which are globally optimal by Li and Khandelwal [74], J Petersson [56], Buhl et al. [30], and Rojas-Labanda and Stolpe [91]. However, some skepticism has been posed on the methodology since it is heuristic. Although the method has been shown to provide close approximations of the global optimal it cannot be proven to always work. Based on the results obtained by Stolpe and Svanberg [104], even though the initial problem is convex, the trajectories of the penalization using continuation has shown to be non-continuous and not always provide black and white designs even with very high values of the penalization parameter.

An alternate method is the use of heavy-side projection functions in conjunction with density filtering. But an inevitable consequence of direct use of such projection functions is the violation of constraints of the final design [74]. Hence, a modified volume-preserving heavy side projection function was proposed by Xu et al. [117]. However, in most cases, the use of the continuation method and suitable filtering (other than morphological filters) do not entirely eliminate all grey elements, especially at the boundaries of the solid and void regions minimal amounts of grey elements can still be

observed. Therefore, to address the same a thresholding strategy is employed to set all elements above a prescribed density to 1 and below it to 0.

3.4. MULTI-OBJECTIVE TOPOLOGY OPTIMIZATION

TO by its very nature/formulation works best when the loading is unique, as the material deposition is specifically decided for a given loading. However, capable structural designs are required to be versatile and hence, must be capable of handling multiple loading conditions. The idea of multi-objective optimization is more of an approximation as compared to a well-defined single objective problem. It is highly unlikely to find a single optimal solution instead of a set of solutions that all satisfy the optimality conditions, some better than others and some even equal in performance. The immediate most logical method which comes to mind is the min-max formulation where the optimization is performed specifically in each iteration with respect to the load case which has the maximum compliance. However, such a formulation is trifled with discontinuities and hence not preferred. The methods of solving multi-objective problems can be broadly divided into two types based on the presence or absence of prior specification/knowledge of preferences of the objectives relative to each other[77]. The former is most often used in topology optimization as the criticality of each loading case is often known or in most cases considered equal. The most frequently employed being the 'global criterion method', the simplest of which is the weighted exponential sum. The weights utilized corresponding to the individual objectives behave as the corresponding measure of significance/preference.

$$U = \sum_{i=1}^{k} w_i \left[F_i(\mathbf{x})\right]^p \tag{3.20}$$

The most basic form of the weighted exponential is when p = 1 and all the weights are set to 1 and this is commonly used in conjunction with the SIMP method for its simplicity [97]. Similar variations such as the weighted product method and the exponentially weighted criterion are utilized as well. Unit consistency is ensured using normalized objectives.

$$U = \sum_{i=1}^{k} \left(e^{p w_i} - 1\right) e^{p F_i(\mathbf{x})} \tag{3.21}$$

$$U = \prod_{i=1}^{k} \left[F_i(\mathbf{x})\right]^{w_i} \tag{3.22}$$

The bound formulation is an alternate methodology for conversion of a min-max objective formulation into a minimization operation, proposed by Bendsoe et al.. The method is proven to outperform the simple weighted sum formulations when the objectives included a combination of stiffness(compliance) and eigenvalue constraints[65].

The modified formulation is given by (3.23).

$$\begin{aligned} &\min_{D} \beta \\ &\text{subject to: } w_i F_i - \beta \leq 0, \quad i = 1, \ldots, k \end{aligned} \tag{3.23}$$

Although the weighted sum unification and its variants are commonly preferred for their simplicity, this method is incapable of capturing a significant portion of the Pareto front, since the solution obtained depends heavily on the weights used, and hence it is not assured to converge to a global optimal [109]. Consequently, various methods have been suggested for the selection of the weights (when the preference is not known or there is an equal preference), therefore widening the Pareto front to widen the access to globally optimal solutions. Common approaches in determining the weights are the use of evolutionary search methods and fuzzy set logic [77]. However, studies illustrate the inability of constant weights (obtained by any method) to provide globally optimized solutions. Consequently, the weights themselves are to be a function of the objectives themselves [78].

Additionally, the Kreisselmeier-Steinhauser aggregation methodology can be used to model the min-max(compliance) function and has proven to provide more superior results than the bound formulation for TO[57]. The KS objective does not possess any tailoring parameters (weights) that affect the Pareto front and therefore form a suitable alternative to the weight dependant formulations. Figure 3.20 illustrates a comparison between the KS strategy and bound formulations. The KS objective provides a solution that converges quickly when compared to the bound formulation and therefore it is a suitable strategy for larger mesh size.

$$f_{\text{KS}} = \frac{1}{p} \ln \sum_{i=1}^{k} \mathrm{e}^{p f_i} \tag{3.24}$$

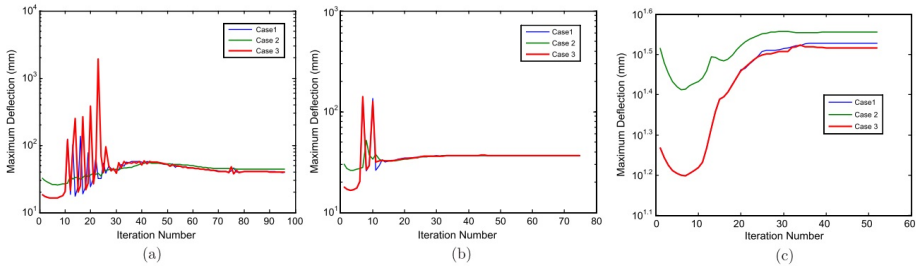

Figure 3.20: Comparison of convergence through (a) Bound formulation (b) Constant KS Aggregation approach (c) Graduated KS Aggregation approach (James et al.[57]).

For TO strategies to generate lightweight solutions, a compliance volume product method has also been suggested by Li et al. to incorporate both volume and compliance as a unified objective using a normalized exponential weighted criterion [72]. The

unique feature of the method is the absence of any empirical decisions of the design constraints. The method is proven to be capable of capturing all the Pareto points in both convex and non-convex problems. An illustration of the method is described in Figure 3.21 and the compliance volume product based objective is given by (3.25).

$$\underset{X=\{x_1,x_2,\ldots,x_n\}^{\mathrm{T}}}{\text{Minimize}} \quad P(x) = \sum_{k=1}^{m} \left(\exp\left(q w_k^c\right) - 1\right) \exp\left(q\left(\frac{C_k(x) - C_k^{\min}}{C_k^{\max} - C_k^{\min}}\right)\right) + \left(\exp\left(q w^v\right) - 1\right) \exp\left(q\left(\frac{V(x) - V^{\min}}{V^{\max} - V^{\min}}\right)\right) \tag{3.25}$$

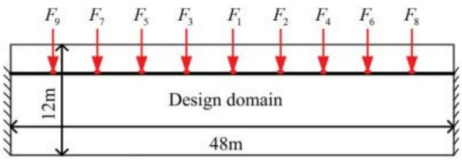

(a) Load cases 1 : F_1 , Load case 2 : $F_{2,3}$, Load case 3 : $F_{4,5}$, Load case 4 : $F_{6,7}$, Load case 5 : $F_{8,9}$

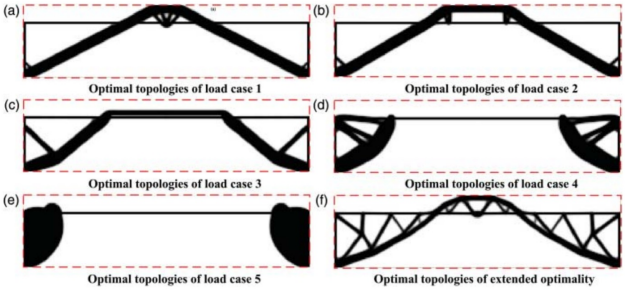

(b) Individual load case solution (a-e) and multiple load case solution(f)

Figure 3.21: Illustration of compliance volume product objective results (Li et al. [72]).

3.5. TOPOLOGY OPTIMIZATION TOOLS

Although initially, TO was more a researcher's tool, its widespread capabilities resulted in a significant number of modeling and simulation software providers adding it to their catalog of product development tools. An extensive list of such tools tabulated in Table 3.1 was consolidated by Barroqueiro et al. for their capability toe be employed for additive manufacturing in the aerospace industry [15]. The most frequently used commercial TO tool is OptiStruct by Altair [64]. However, in this project itself, two packages were considered for use: TopOpt and Abaqus/TOSCA.

Commercial Software	Developer	FEA Solver	Analysis Regime
Dreamcatcher	Autodesk	Standalone	S, E
Within Enhance	Autodesk	Standalone	S, E
Tosca	Dassault Systemes	Ansys/Abaqus /Nastran	S, E, D
ATOM	Dassault Systemes	Abaqus	S,E
Ansys		Standalone	S,E,D
Sol200	MSC	Standalone	S,E,D
Optistruct	Altair	Standalone	S,E,D
Vanderplaats Genesis	VRand	Ansys	S,E,D
Solid Thinking Inspire	Solid Thinking	Optisttruct	S,E,D
PERMAS-TOPO	Intes	Standalone	S,E,D
FEMtools Optimization	Dynamic Design Solutions	Ansys/Abaqus /Nastran	S,E,D
OPTISHAPE-TS	Quint Corporation	Ansys	S,E,D
ParetoWorks	Sciart Rethinking Design	Standalone	S
ProTop	CAESS	Standalone	S,E
Educational Tools			
BESO 3D	RMIT University	Abaqus	S
Topostruct	Sawapan	Standalone	S
ToPy	William Hunter	Standalone	S
TRINITAS	Linköping University	Standalone	S
TopOpt	TopOpt Research Group	Standalone	S

Table 3.1: List of commercial and open-source tools available for topology optimization. The analysis regime covered are S-Static, E-Eigen value and D- Dynamic (Barroqueiro et al. [15]).

3.5.1. EVALUATED TOOLS

TOPOPT

The TopOpt package developed by Danish Technological University is an open-source topology optimization package that is capable of performing large-scale topology optimization in 3D[8]. The framework is based on PETSc/TAO where PETSc is a suite of data structures and routines for the scalable (parallel) solution of scientific applications modeled by partial differential equation and TAO is the toolkit for advanced optimization. The Topopt package is readily able to voxel-based TO tasks as illustrated in Figure 3.22a, but it is incapable of importing CAD models. Thus keeping in mind the complex architecture of the galley, the employment of TopOpt would prove to be rather cumbersome.

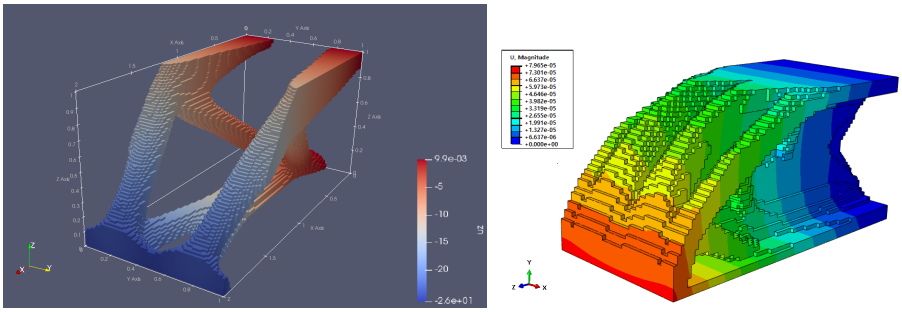

(a) TopOpt (b) Abaqus-TOSCA

Figure 3.22: Topology optimized 3D cantilever beam using available packages

ABAQUS/TOSCA

Abaqus is one of the leading commercial Finite Element Analysis tools. The optimization toolbox within Abaqus utilizes a subset of the TOSCA optimization package. Capable of performing size, shape, topology, and bead optimization, Abaqus is a highly capable tool to realize lightweight, rigid, and durable structures. The professionally developed tool is well adapted to handle both 2D as well as 3D structures with the capability of custom free form modeling using the CAE application. Thus, making it an ideal candidate for the G5 galley optimization. Therefore in the interest of time, availability, and simplicity, ABAQUS/2019 was chosen for the optimization of the G5 galley.

4

G5 Topology Optimization

The G5 optimization is conducted using the TOSCA package within ABAQUS. This chapter comprises the modeling, analysis, and optimization strategy employed for the same. Section 4.1 comprises the TO compatible modeling strategy employed in ABAQUS analogous to those currently used for certification. Section 4.2 describes the specifications for the optimization itself , followed by the corresponding results in Sections 4.3 and 4.4.

4.1. G5 MODELING

Keeping with the modeling method utilized for certification as specified in Section 2.3, the galley is modeled using plates with all intermediate inserts and fixtures eliminated. A key difference in the modeling employed for TO is the material model. Although the G5 galley is a composite structure, the TO methodology to be employed relies on the SIMP model which assumes an isotropic material elasticity. Therefore, the galley material is changed to Aluminium with Elastic modulus E = 70 GPa and Poisson's ratio = 0.25. Additionally, the G5 currently employs variable plate thickness, however the model employed for TO utilizes uniform thickness plates.

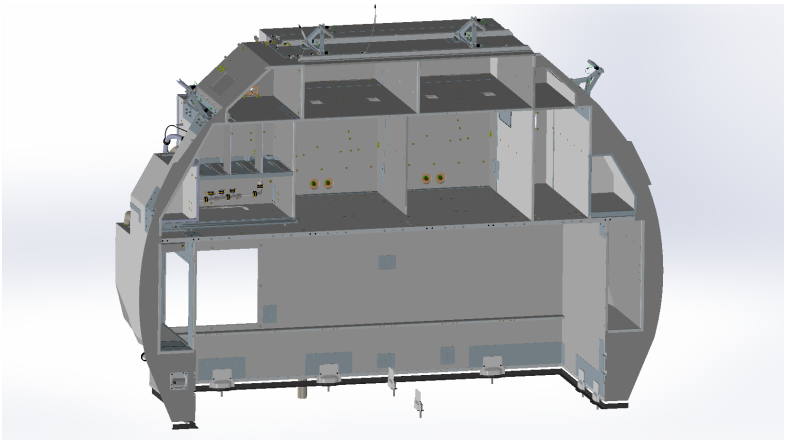

(a) G5 Solidworks model

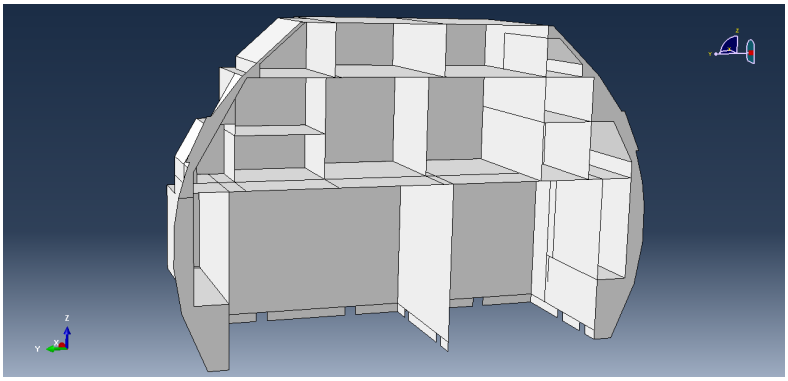

(b) G5 Abaqus model

Figure 4.1: Modeling panel-based design of G5 as plate elements.

4.1.1. LOADING

The certification loading is inertial in nature, different in all 6 directions. This is not problematic in the case of static analysis, but in the case of topology optimization, the material distribution and the relative density change constantly, hence this changes the inertial loading in each iteration of the optimization process. Also, Abaqus is incapable of performing topology optimization in the case of distributed loading since, all load application points are frozen and if unfrozen, the load itself is no longer resisted by the structure. Hence there is no direct method to incorporate self weight-induced inertial loading. Therefore, the inertial loading of the galley itself will be omitted. However, the galley weight is limited to close to 30% of all the appliance weight combined therefore comparatively, the influence of the galley inertial load is comparatively lesser than the appliance and trolley loading.

TROLLEY LOADING - CONSISTENT POINT LOAD SET

During the sideways load case, the trolley makes contact with the adjacent galley panels as illustrated in Figure 4.2. This can be modeled as a uniformly distributed load (UDL) over the corresponding panel surface. However, since loading points are frozen in TO, a UDL force will yield an absence of any material removal in the adjacent panel. This limits the possibilities for optimized solutions. Therefore, an alternative loading strategy is required to simultaneously allow for load transfer as well as material removal. A possible methodology is to utilize a set of point loads equal to a fraction of the inertial load distributed over the panel. Additionally, to ensure that consistency is maintained on converting from a uniformly distributed load to a point load, the moment and forces experienced at the boundaries of the panel must remain equivalent.

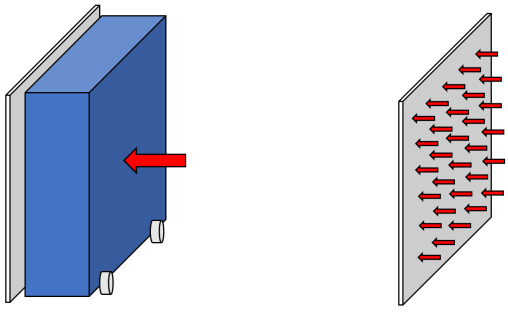

(a) Trolley inertial force

(b) UDL trolley inertial force on the adjacent panel

Figure 4.2: Trolley loading on adjacent panel.

To this extent, a simplified set of point loads is proposed which produces the same displacement profile as well as reaction force profile as a UDL. This can be obtained as a solution to the equivalent n^{th} moment transfer at the boundaries due to n point loads. The locations of a set of N equal loads to replace a UDL(P applied over a span L)

is provided through solving a set of N non-linear equations given by (4.1).

$$\sum_{i=1}^{N} {x_i}^n = \frac{NL^n}{n+1} \text{ where, } n \in (1, N) \tag{4.1}$$

With the equal point loads given by:

$$F_i = \frac{PL}{N} \tag{4.2}$$

No. of point loads	Location (0-L)	Load (F_T = P*L)
1	0.5	F_T
2	0.21132487, 0.78867513	0.5 F_T
3	0.14644661, 0.5, 0.85355339	0.333 F_T
4	0.10267276, 0.40620376, 0.59379624, 0.89732724,	0.25 F_T
5	0.08375126, 0.3127293, 0.5, 0.6872707, 0.91624874	0.2 F_T

Table 4.1: UDL equivalent point load and locations for a span of L=1.

The results in Figure 4.3 prove that the method is successful in approximating the displacement profile of a UDL load over a 1x1m span plate clamped on all edges. Therefore in the context of a galley where UDL load is applied on a panel, the replaced set of point loads can result in the same magnitude of load and moment transferred to the adjacent connected panels.

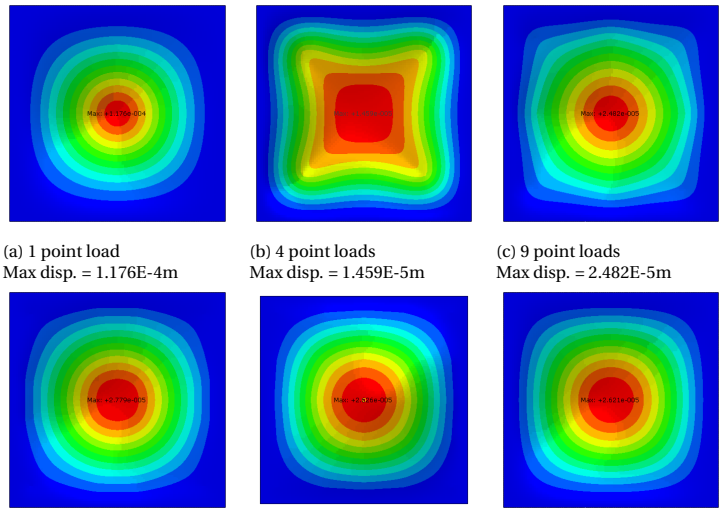

(a) 1 point load
Max disp. = 1.176E-4m

(b) 4 point loads
Max disp. = 1.459E-5m

(c) 9 point loads
Max disp. = 2.482E-5m

(d) 16 point loads
Max disp. = 2.779E-5m

(e) 25 point loads
Max disp. = 2.626E-5m

(f) UDL load
Max disp. = 2.621E-5m

Figure 4.3: Maximum displacement of 1x1m fully clamped plate subjected to UDL (Magnitude 1 kN) and a set of equivalent point loads.

Figure 4.4 illustrates the results when the same 'UDL equivalent point load set' approach is used as the loading case for topology optimization of said plate. The resulting topology is designed to handle the same amount of load as the total UDL and has the benefit of being a more practical structure. For the G5 itself a set of 3 × 3 set is used for the LEFT/RIGHT load case and 2 × 3 set is used for the AFT Load case.

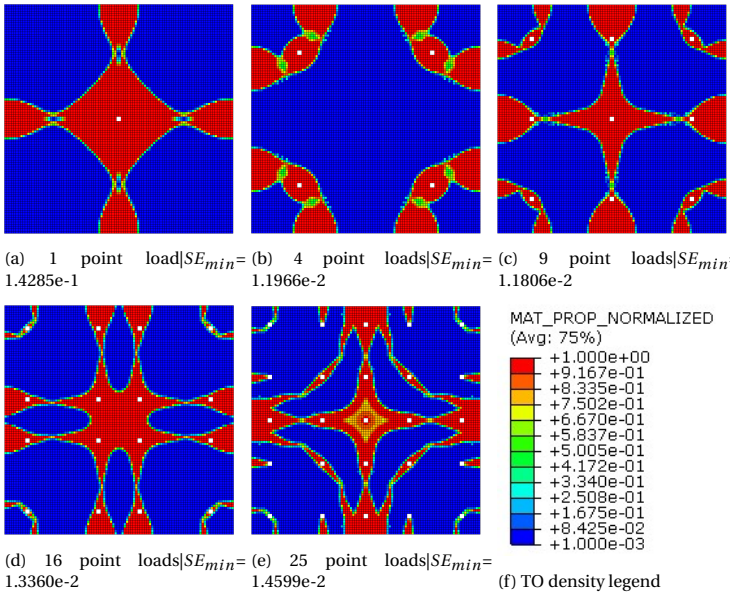

(a) 1 point load|SE_{min}= 1.4285e-1 (b) 4 point loads|SE_{min}= 1.1966e-2 (c) 9 point loads|SE_{min}= 1.1806e-2

(d) 16 point loads|SE_{min}= 1.3360e-2 (e) 25 point loads|SE_{min}= 1.4599e-2 (f) TO density legend

Figure 4.4: TO solution for 1x1m fully clamped plate subjected to a set of UDL equivalent point loads(white squares)

APPLIANCE LOADS

Following the currently accepted methodology for loading as specified in Section 2.3. The appliance inertial loads are modeled as point loads applied at the CG of the appliance with coupling to tie-down points of the appliances within the cabinet space as illustrated in Figure 4.5.

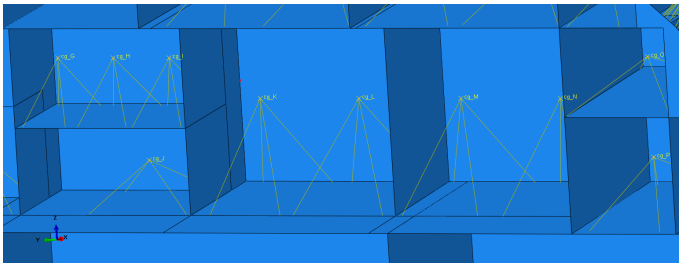

Figure 4.5: Appliance loading through CG coupling.

4.1.2. BOUNDARY CONDITIONS

The galley is attached to the aircraft at discrete locations through fixtures and anchors as indicated by Figure 4.6. These interface points form the boundary conditions for the analysis of the structure. The joints connecting the G5 galley to the aircraft are incapable of supporting any reaction moments and can only sustain reaction forces. The joints are modeled through a single connection point coupled to the galley as illustrated in Figure 4.7.

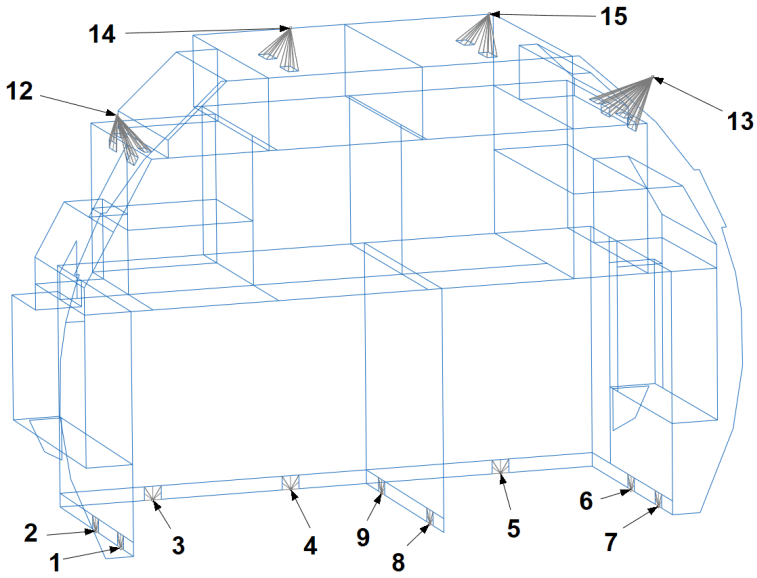

Figure 4.6: G5 Interface points

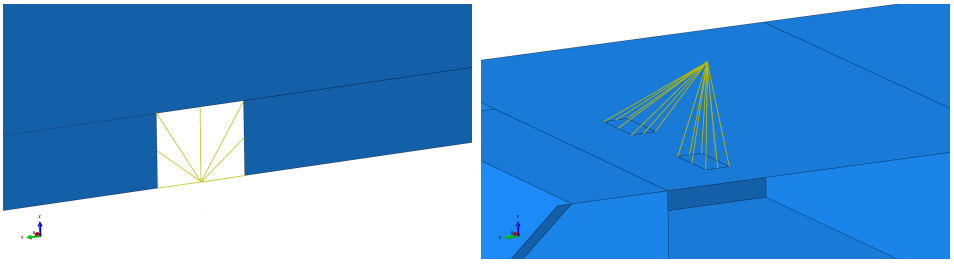

(a) Bottom (UX,UY,UZ = 0)

(b) Top (UX = 0)

Figure 4.7: G5 boundary conditions.

4.2. G5 TOPOLOGY OPTIMIZATION FORMULATION

Following the construction of a suitable model and adaptation of loads and boundary conditions, the TO of the galley itself requires suitable topological descriptors and descriptive design responses to be enhanced and constrained. These are encompassed within the Design domain, the optimization objective, and constraints. The Finite Element Model is constructed within ABAQUS with the required boundary conditions. Each load case is modeled as an individual static analysis. The constructed model and the static analysis results are utilized as the descriptors for the objective and constraints within TOSCA (within ABAQUS).

DESIGN DOMAIN

The design domain is the Finite Element Mesh of the undivided galley as a whole. The domain is discretized into quadrilateral elements of size 10mm. For simplicity and in the interest of uniformity, a constant shell thickness of 12.5mm is adopted throughout the galley.

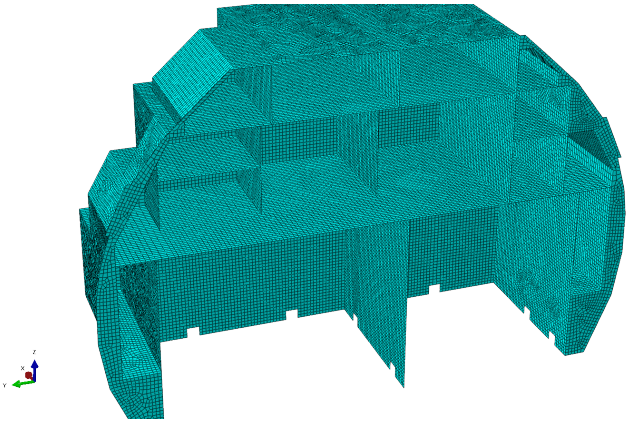

Figure 4.8: Quad mesh | no. of nodes = 209139 | no. of elements = 209521.

OBJECTIVE

As described in Section 2.2, the maximum inertial loads in the 6 principal directions form the load cases from the loading requirements of the Galley. Since each of the six load cases (LC) is unique and dissimilar in magnitude and direction, the structural response of the galley is unique in each case. Therefore, the optimization of the G5 requires all 6 load cases to be considered. Therefore, multiobjective optimization is best suited for the G5 galley. As described in Section 3.4, the objectives can be combined through various methods. Since each of the load cases is independent, the structural response to each case can be considered equally important. Consequently, a straightforward compliance(C) sum formulation can be employed as the objective to be minimized. Within

ABAQUS the compliance is represented through its analytical equivalent, the strain energy(SE). It is to be noted, although Strain energy is essentially any integral over the strain and elasticity field over the entire domain, within the TOSCA toolbox itself the SE is computed based on the external loading [1].

Therefore the optimization objective can be stated as (4.3).

$$\min Objective = \sum_{LC=1}^{LC=6} C_{LC} = \sum_{LC=1}^{LC=6} SE_{LC} \qquad \text{where, } C = SE = \sum u^T K u \tag{4.3}$$

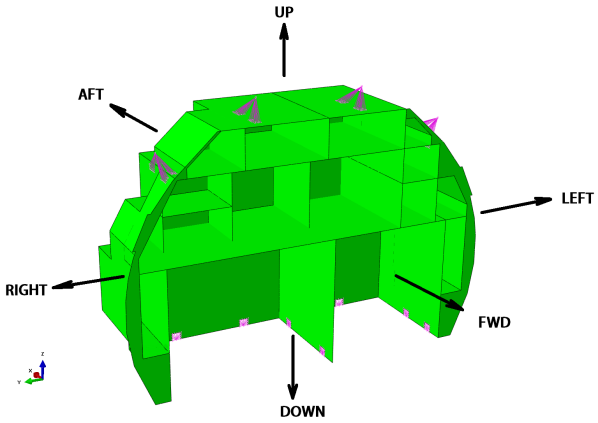

Table 4.2: Inertial load factors

Load case ID	Direction	Inertial Load Factors
1	AFT	L_{AFT}
2	DWN	L_{DWN}
3	FWD	L_{FWD}
4	LEFT	L_L
5	RIGHT	L_R
6	UP	L_{UP}

Figure 4.9: Load case description

4.2.1. DESIGN CONSTRAINTS

Assuming a constant thickness of 12.5mm throughout the galley, the weight of a fully metal galley would have a mass of W_m. To achieve a structural weight equal to that of the current composite design (W_g) a mass constraint is to be imposed. This is formulated as a volume constraint of (35%) and supplemented into the optimization routine.

4.2.2. REACTION FORCE CONSTRAINT

The interface load limits as prescribed in Section 2.2 are limitations on the connection points and can be posed as reaction force constraints. Considering each of the 13 interfaces and the 6 load cases a total of 186 reaction forces are to be considered and 352 constraints are to be employed(Maximum and minimum limits). The addition of con-

[1] It should be noted that the accurate formulation for C/SE is $0.5 \times \sum u^T K u$. Within ABAQUS for TO based on linear FEM, the 0.5 coefficient can be neglected without affecting the optimization result.

straints to an already fine-mesh model increases the computational expense of the optimization problem significantly[2]. Hence, to reduce the number of constraints max and min unification is applied over the reaction forces at each interface. The specific limits are as tabulated in Table 2.2.

$$RF_{i_{min}} \leq RF_i \leq RF_{i_{max}} \tag{4.4}$$

$$\begin{aligned} \min\left(\{RF_i\,(LC) : LC = 1 \text{ to } 6\}\right) &\geq RF_{i_{min}} \\ \max\left(\{RF_i\,(LC) : LC = 1 \text{ to } 6\}\right) &\leq RF_{i_{max}} \end{aligned} \tag{4.5}$$

4.2.3. OPTIMIZATION ALGORITHM

The use of a discretized domain in pairing with interpolation schemes such as SIMP essentially converts the optimal topology problem into a continuous sizing problem thus allowing for the use of continuous optimization strategies. The standard continuous structural optimization strategies rely on the use of the value/values of design variables and their associated displacement profile from the previous iteration to update the corresponding design variables suitably for the next step [89]. This sensitivity-based approach in pairing with suitable optimality criteria(OC) allows for the identification of the optimized solution. Consider the continuous form of the minimum compliance problem from Section 3.1 coupled with the SIMP material interpolation model given by [3] (4.6). As an alternative to computing the objective sensitivity directly, the Lagrange multiplier strategy can be utilized to encompass the constraints within a unified objective. The unified unconstrained objective or the Lagrange function is given by (4.7).

$$\begin{array}{ll} \min_{u\in U,\rho} & l(u) \\ \text{s.t.} & a_E(u,v) = l(v), \quad \text{for all } v \in U \\ & E_{ijkl}(x) = \rho(x)^p E^0_{ijkl} \\ & \int_\Omega \rho(x)\mathrm{d}\Omega \leq V; \quad 0 < \rho_{\min} \leq \rho \leq 1 \end{array} \tag{4.6}$$

$$\begin{aligned} \mathscr{L} = l(u) - \{a_E(u,\bar{u}) - l(\bar{u})\} + \Lambda\left(\int_\Omega \rho(x)\mathrm{d}\Omega - V\right) + \\ \int_\Omega \lambda^+(x)(\rho(x)-1)\mathrm{d}\Omega + \int_\Omega \lambda^-(x)\left(\rho_{\min} - \rho(x)\right)\mathrm{d}\Omega \end{aligned} \tag{4.7}$$

$\Lambda, \Lambda^-(x)$, and $\Lambda^+(x)$ are the Lagrange multipliers for the constraints in (4.6) and the necessary conditions for the optimal sizing variable ρ are an subset of the stationary conditions for the Lagrange function given by 4.8. For intermediate densities ($0 \leq \rho \leq 1$), the Lagrange multiplier Λ is given by (4.9) based on which an update strategy is proposed by Bendøse and Sigmund given in (4.10). The update strategy attempts to either add

[2] The choice of aggregating was for no other reason than to hasten the optimization process.
[3] The minimum value of ρ is limited to $\rho_{min} = 10^{-3}$ to avoid singularities occurring at $\rho = 0$.

or reduce the density based on the the parameter B_k ($B_k = 1$ implies optimality). The parameters ζ and η are tuning parameters where ζ controls the aggressiveness of the update scheme and η sets the limiting update magnitude.

$$\frac{\partial E_{ijkl}}{\partial \rho}\varepsilon_{ij}(u)\varepsilon_{kl}(u) = \Lambda + \lambda^{+} - \lambda^{-} \tag{4.8}$$

$$p\rho(x)^{p-1}E^{0}_{ijkl}\varepsilon_{ij}(u)\varepsilon_{kl}(u) = \Lambda \tag{4.9}$$

$$\rho_{K+1} = \begin{cases} \max\{(1-\zeta)\rho_K, \rho_{\min}\} & \text{if } \rho_K B_K^{\eta} \le \max\{(1-\zeta)\rho_K, \rho_{\min}\} \\ \min\{(1+\zeta)\rho_K, 1\} & \text{if } \min\{(1+\zeta)\rho_K, 1\} \le \rho_K B_K^{\eta} \\ \rho_K B_K^{\eta} & \text{otherwise} \end{cases} \tag{4.10}$$
$$B_K = \Lambda_K^{-1} p\rho(x)^{p-1} E^{0}_{ijkl}\varepsilon_{ij}(u_K)\varepsilon_{kl}(u_K)$$

The update strategy described by (4.10) represents a traditional OC-based gradient descent approach applied to the topology optimization problem. However, a key limitation of the Lagrange multiplier method is its functioning limited to self-adjoint problems. Specifically, within the scope of TO, non-structural constraints such as size constraints cannot be included within the optimality criteria scheme. To this extent, mathematical programming strategies provide a suitable alternative to the OC-based strategy. Nonetheless, a distinguishing feature of TO is the customary large number of design variables, leading to large computational expenses if indiscriminately implemented in conjunction with mathematical programming. Hence, programming strategies implemented for TO are required to be capable of handling a large number of variables and constraints. Within the field of TO, one such method is predominantly employed, it is the method of moving asymptotes (MMA)[105][17]. Belonging to the group of convex approximation methods, MMA optimizes the given problem by solving a convex subproblem in each iteration. Given an objective function $F(x_1, x_2, x_3 ... x_n)$ to be minimized, the convex sub-problem at iteration j has the form:

$$F^j(x) = F\left(x^j\right) + \sum_{i=1}^{n}\left(\frac{r_i}{U_i - x_i} + \frac{s_i}{x_i - L_i}\right)$$
$$L_i^j \le x_i^j \le U_i^j \tag{4.11}$$

Where r_i, s_i are chosen as,

$$\text{if } \frac{\partial F}{\partial x_i}\left(x^j\right) > 0 \text{ then } r_i = \left(U_i - x_i^j\right)^2 \frac{\partial F}{\partial x_i}\left(x^j\right) \text{ and } s_i = 0$$
$$\text{if } \frac{\partial F}{\partial x_i}\left(x^j\right) < 0 \text{ then } r_i = 0 \text{ and } s_i = -\left(x_i^j - L_i\right)^2 \frac{\partial F}{\partial x_i}\left(x^j\right) \tag{4.12}$$

Here, L_i and U_i are the so-called asymptotes. In the case of MMA, both L_i and U_i are finite in magnitude leading to F^j being strictly convex (except when $(\frac{\partial F}{\partial x_i})^j = 0$) [4]. This allows for the optimizer to sequentially move towards the optimized solution similar to the OC strategy. In the implementations for straightforward minimum compliance, the MMA does not perform significantly superior to the OC method; However, the distinguishing feature of the MMA is in its capability to incorporate more complex objectives and the capability of handling a large number of constraints as well as its excellent convergence properties[17]. Therefore, considering the large FEM model of the G5 galley as well as the significant number of constraints, the MMA optimizer within ABAQUS/Tosca can be deemed acceptable for the G5 optimization application[5].

Material Interpolation technique	SIMP | p = 3
Maximum - Minimum Density	0.001 - 1.00
Convergence criteria : Objective Δ	0.0001
Convergence critera : Element Density Δ	0.0001
Frozen regions	Loading & BC regions
MMA - Density update Strategy	Normal

[4] The values for the asymptotes are dependant on the constraints posed on x_i. As a general recommendation, if the process tends to oscillate the asymptotes are to be moved closer to x^k and if the process is slow the asymptote gap can be relaxed and moved apart. This is incorporated in ABAQUS as a 'CONSERVATIVE' and 'AGGRESSIVE' setting respectively

[5] Within the Abaqus optimization toolbox MMA is the sole optimizer available, however, the author prefers to underline its capabilities and proven track record within TO.

4.3. RIGID INTERFACE OPTIMIZATION

Keeping in mind that the G5 galley domain has been previously designed to handle the interface loading requirements albeit, with composite panel material, it is best to build the optimization complexity in 2 steps. Therefore, the first TO study will be conducted without consideration of interface load transfer. This reduces the optimization to a classic volume-constrained minimum compliance problem. The optimization problem statement is as described in statement 4.13 [6]

$$\begin{aligned} \min_{\rho} SE &= \sum_{LC=1}^{LC=6} SE_{LC} \\ \text{subject to}: &\int_{\Omega} \rho \delta v \leq V_{lim} \end{aligned} \tag{4.13}$$

The results of the optimization routine described by (4.13) is illustrated in Figure 4.10 [7]. The optimization has been successful in reducing the volume. However, it must be noted that much of the upper part of the galley has been eliminated. This can be attributed due to the lack of stiffness offered by the upper joints (12,13,14,15). Due to the absence of load-carrying capability in 2 of 3 directions of these joints the optimizer demonstrates a preference to redirect material towards the load-capable interface points at the bottom to achieve larger compliance reduction. Consequently, much of the limited fraction of material available is directed towards retaining the stiffness offered by the lower interface points leading to non-uniform material retention over the entire structure resulting in some panels almost entirely eliminated and some entirely retained. Although this is an expected outcome from topology optimization, panels in their entirety cannot be eliminated without losing the functionality of the Galley. Consequently, additional constraints are necessary for achieving/retaining functionality.

[6] Henceforth any optimization problem statement implicitly includes 1) A static equilibrium constraint for all the load cases and 2) Design variable $\rho \in [0,1]$.

[7] All thresholded for a minimum value of 0.3. The contour description of all subsequent TO results will follow the same legend as Figure 4.4.

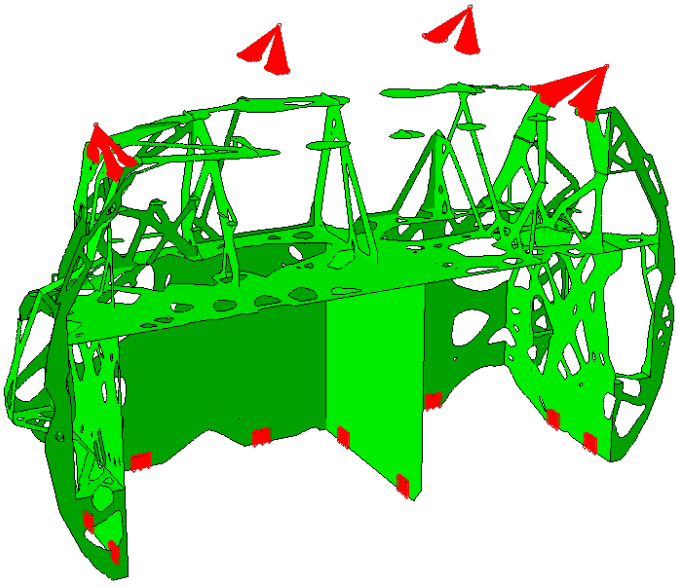

(a) 3D view

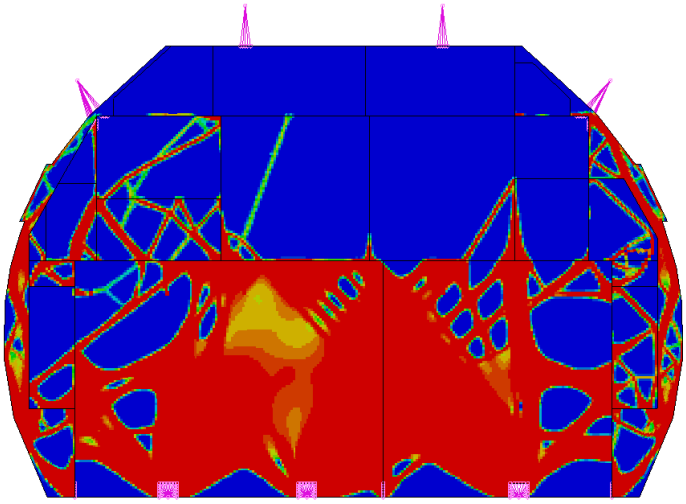

(b) Front view

(c) Panel 38

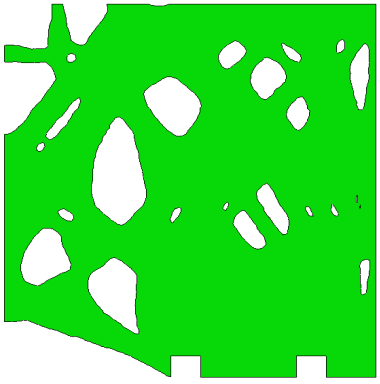

(d) Panel 42

Figure 4.10: Rigid interface G5 TO result. $V_{lim} = 0.35V_0$. $SE_{optimized} = 84.43J$

4.3.1. BANDED GEOMETRIC CONSTRAINT

The generated topology in Figure 4.10 contains fully eliminated panels, fully retained panels, and everything in between. Ideally, any material removal must not incur a complete loss in the partitioning and any material retention must not create a disproportionate shortage of material in other regions i.e. an entire panel must not be eliminated and no panel must be fully retained. As already observed, all the panels on the upper region of the galley have been eliminated and the center trolley partition wall has almost entirely been retained. Figure 4.10c and Figure 4.10d illustrate other intermediate topologies. Of the two panels, the former is preferable, as it maintains a practical partition and at the same time depicts large volume reduction. Whereas, the latter depicts more scope for material removal. The key identifying feature of Panel 38 is the features are limited in their geometrical dimension. Hence, a dimensional constraint could offer an alternate preferable solution.

Adding a geometric constraint to constrain topology dimensions to a given range results in a more standardized topology. In the G5 study case, a geometric constraint of 2cm to 4cm is employed. It can be argued that the constraint range is much larger than the plate thickness (12.5mm). But the constraint was set keeping in mind that the element size adopted for the mesh is 1cm (average) and TO size constraints must be larger than 2 times the mesh size to avoid checkerboards and a 2 element gap between the lower and upper dimension limit is advisable. The chosen geometric limits are the most reasonable form of the dimension constraint while keeping in mind the plate thickness, mesh size, and TO filter properties ($R_{filter} = 1.3 d_{el}$).

The generated topology is presented in Figure 4.13. Compared to the topology without geometric constraint, the material retention is more suitable and retains the functionality of the galley. It can also be observed that this constraint has countered the preference of entirely disregarding the upper anchors. The webbed structure obtained in the rear panel displayed in Figure 4.11a is an ideal topology for low weight as well as maintaining functionality. The topology can be described/characterized by branches growing from the anchor locations and spreading in such a way so as to possess a large volume of coverage while maintaining the required resource limitations. Interestingly, the obtained structure is reminiscent of iso-grid or grid stiffened structures as illustrated in Figure 4.11. Figure 4.11a showcases the localization of stress within the branches analogous to the tailored stress paths of grid stiffened structures similar to Figure 4.11b.

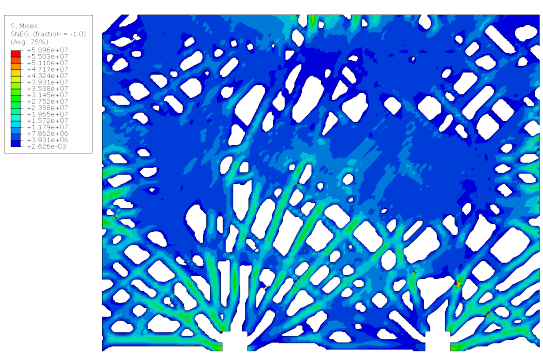

(a) Stress flow through discrete branches leading to the interface locations.

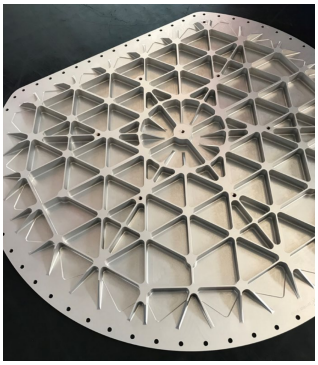

(b) Grid stiffened structure (Sanmiguel [96]).

Figure 4.11: Grid stiffened structure-esque topology obtained through addition of geometry constraints.

Comparing the strain energies an expected outcome of added additional constraints is observed. The minimized compliance increases from $SE_{G5} = 84.43J$ to $SE_{G5_Z} = 209J$. This translates to roughly a 2.5x increase in the deformation at the loading points. A similar trend is noticed in the maximum displacement tabulated in Table 4.3 with a maximum displacement of 26mm observed in FWD.

The generated topology in Figure 4.13 contain localized checkerboard regions, which as described in Section 3.2.1 are artificially stiffening regions which are numerical anomalies and undesirable in TO. Unfortunately, due to the chosen mesh size and filter radius, these regions cannot be entirely eliminated. A possible mitigation strategy is through a reduction of the desired final volume fraction, leading to a contraction of the checkerboard regions as displayed in Figure 4.14. However, this reduction in volume constraint affects both checkerboard and relevant regions alike, therefore also eliminating relevant material branches and generating floating regions. A possible cause is due to the conflicting scenario created by the mesh size, filter sizes, and the banded dimension constraint.

Considering the adopted mesh size of 10mm and checkerboard filter size of 13mm ($R_{filter} = 1.3d_{el}$) the geometric size constraint of 20mm to 40 mm is questionable. The minimum geometry size constraint implementation within ABAQUS follows a similar filtering strategy to the checkerboard filtering. As a consequence of filtering the already filtered variable, the checkerboards are induced within the solution. Figure 4.12 illustrates an identical situation of filter conflict in a cantilever beam. Ideally, the mesh size is to be much finer than the geometrical constraints implemented. Unfortunately, the computational limitations are already tested with a mesh size of 0.01.

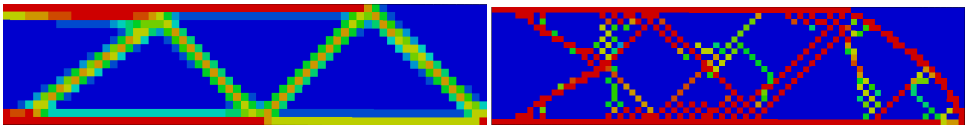

(a) Without size constraint.

(b) With size constraint $d_{minimum}$ = 0.02

Figure 4.12: Cantilever beam TO solution with mesh size of 0.01m and checkerboard filter 0.013m.

Load Case	Min SE + Vol.C		Min SE + Vol.C + Size.C	
	Opt. objective = 84.43 J		Opt. objective = 209 J	
AFT	1.869 mm	Bottom Trolley Rear Panel	4.992 mm	
DWN	1.710 mm	Upper Appliance deck	1.669 mm	
FWD	0.488 mm	Upper deck	central deck	0.996 mm
LEFT	9.100 mm	Trolley mid panel		25.870 mm
RIGHT	6.863 mm			19.480 mm
UP	2.564 mm	central horizontal panel		5.884 mm

Table 4.3: Max. displacement magnitude and location change due to additional size constraint.

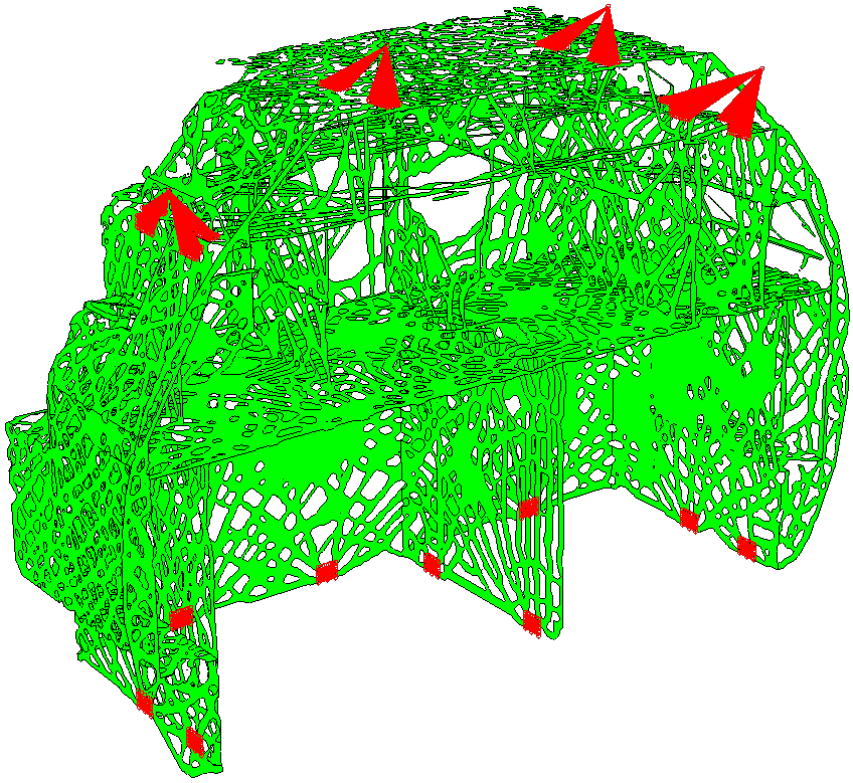

(a) 3D view

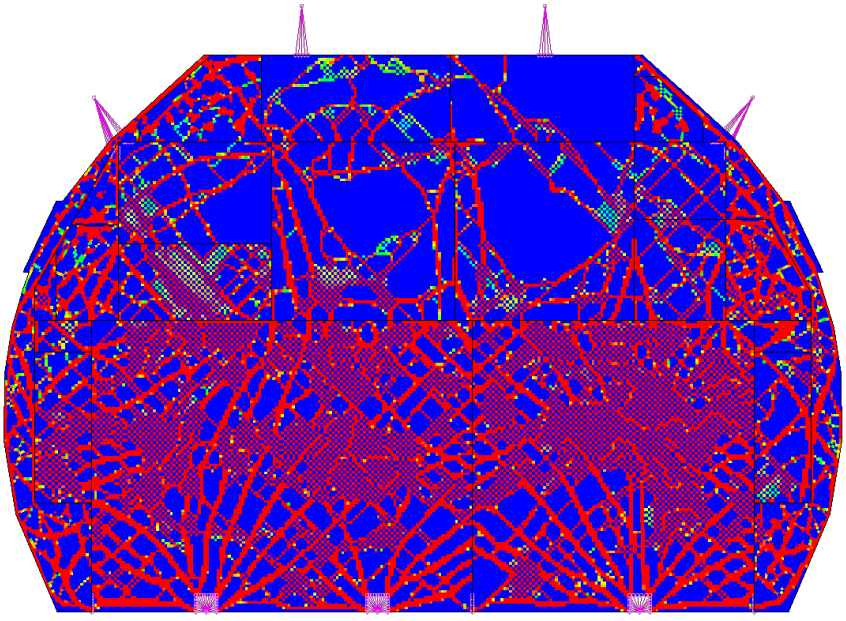

(b) Front view (Checkerboards observed)

Figure 4.13: Rigid interface banded dimension constrained G5 TO result. $V_{lim} = 0.35V_0$. $SE_{optimized} = 209J$.

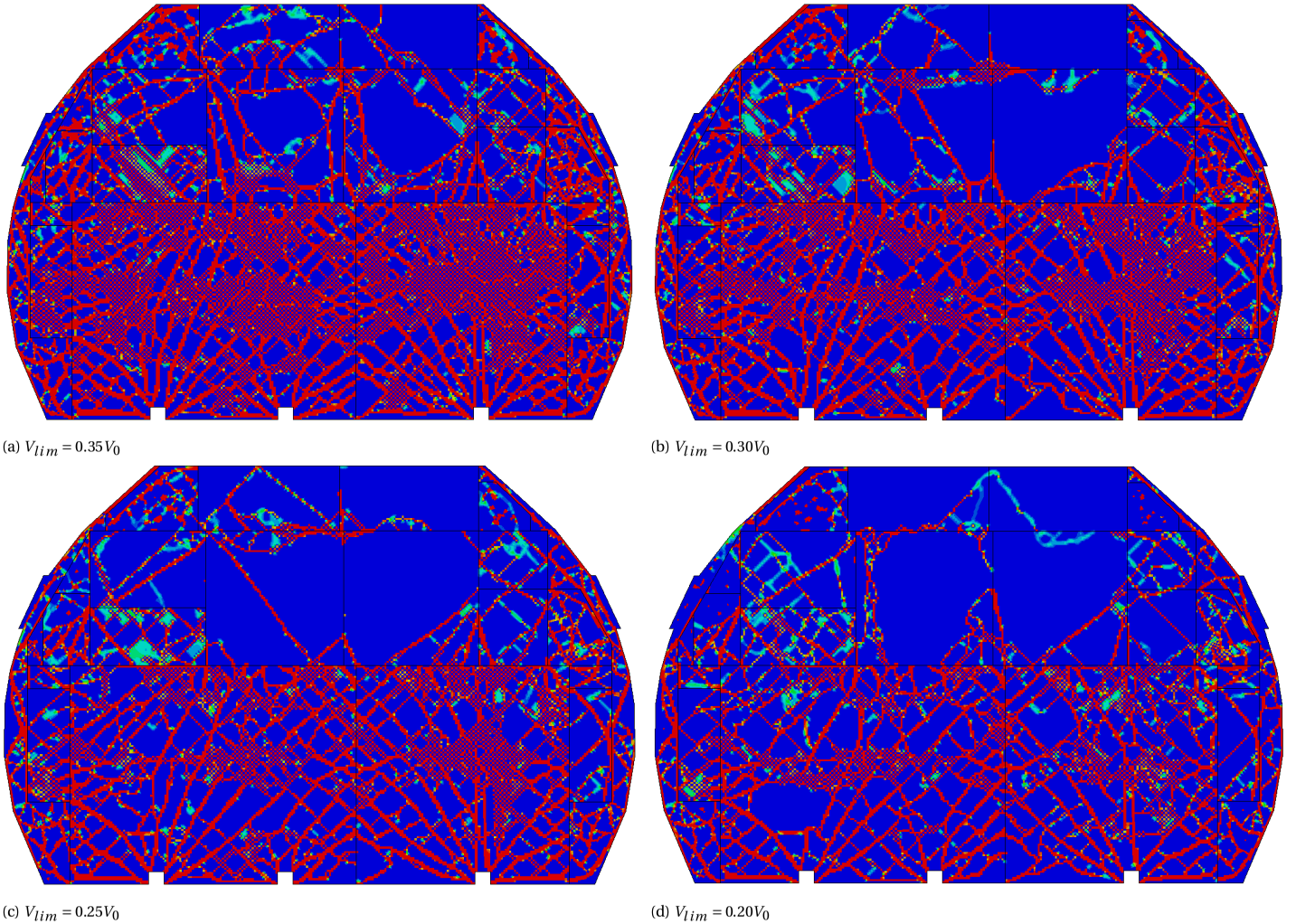

(a) $V_{lim} = 0.35V_0$

(b) $V_{lim} = 0.30V_0$

(c) $V_{lim} = 0.25V_0$

(d) $V_{lim} = 0.20V_0$

Figure 4.14: Volume fraction reduction to reduce checkerboards.

4.3.2. MAX GEOMETRY CONSTRAINT

As observed in Section 4.3.1, the most intuitive form of the geometry constraint yields checkerboards due to the conflicts with the filtering strategies employed. Therefore, the geometric constraint requires relaxation. Consequently, with the motivation of retaining slender members, it is advisable to retain the upper limit on the dimensions, and to avoid the numerical anomalies caused due to the mesh size and the filtering radius, the lower limit is eliminated. Therefore, the original banded constraint of limiting dimensions to 2cm-4cm is replaced with a new constraint of a maximum feature size of 3cm. The corresponding results are illustrated in Figure 4.15. A clear improvement can be observed in the features in comparison to Figure 4.13. The checkerboard regions are almost entirely eliminated and simultaneously the branched structures are expanded.

It is to be noted that although in this case, the results are promising, the stiffness of the interface is assumed to be rigid. But, as specified in the Section 2.2, AIRBUS stipulates limitations on the strengths of the joints. On observation, joints 5, 12, and 13 have violated these limitations and few other locations trail very close to these limits as well. Hence in the interest of satisfying current interface requirements, additional reaction force constraints need to be introduced.

Joint ID	RF_X (kN)		RF_Y (kN)		RF_Z (kN)	
	min	max	min	max	min	max
1	-1.988	7.869	-1.929	0.171	-5.268	16.228
2	-2.056	11.034	-0.253	0.0112	-9.414	10.433
3	-0.717	0.103	-11.782	7.876	-14.24	13.293
4	-0.561	0.365	-11.666	11.662	-7.108	4.510
5	-0.594	0.163	-11.687	14.372	-16.572	17.133
6	-1.496	7.937	-0.067	0.319	-10.429	10.503
7	-2.421	6.486	-0.113	1.914	-4.181	8.862
8	-2.364	14.986	-2.006	2.673	-3.174	19.837
9	-1.557	6.995	-1.315	1.751	-4.818	3.060
12	-3.964	16.600				
13	-4.415	19.125				
14	-1.248	0.959				
15	-0.290	0.248				

Table 4.4: Max interface load transferred of 6 load cases for TO result. $v_{lim} = 35\% V_0$.

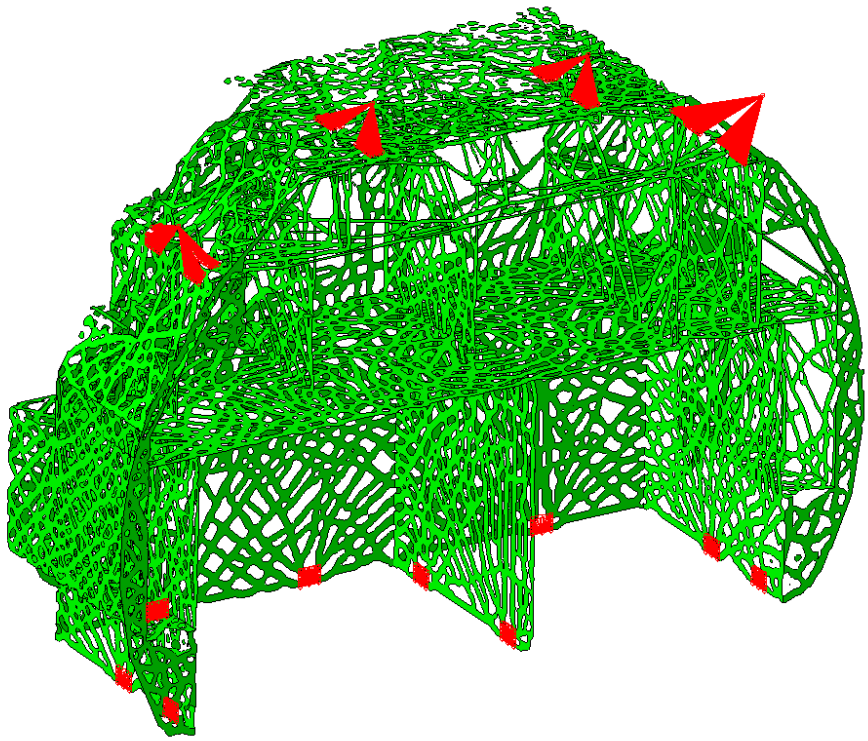

(a) 3D view.

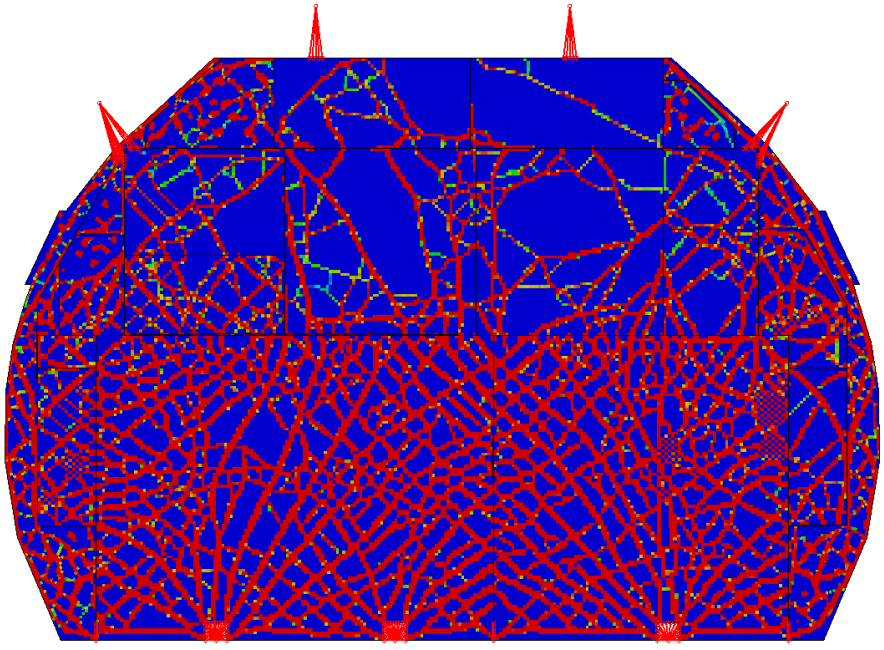

(b) Front view

Figure 4.15: Rigid interface maximum dimension constrained G5 TO result. $V_{lim} = 0.35V_0$. $SE_{optimized} = 203J$.

4.4. FINITE STRENGTH INTERFACE OPTIMIZATION

Although the current galley architecture was designed to handle the interface load limitations, the reduction in volume and change in material proved to violate these limits. To this extent, the interface load limitations are introduced as reaction force limits to the optimization routine. Also, to avoid panel eliminations, the use of maximum feature size constraint as described in Section 4.3.2 is retained. The modified optimization problem is as stated as in statement 4.14.

$$
\begin{aligned}
&\min_{\rho} SE = \sum_{LC=1}^{LC=6} SE_{LC} \\
&\text{subject to :} \\
&\int_{\Omega} \rho \delta v \leq 0.35 V_0 \\
&\min\left(\{RF_i\,(LC) : LC = 1 \text{ to } 6\}\right) \geq RF_{i_{min}} \\
&\max\left(\{RF_i\,(LC) : LC = 1 \text{ to } 6\}\right) \leq RF_{i_{max}}
\end{aligned}
\tag{4.14}
$$

The resulting TO outcome is presented in Figure 4.17. The webbed structure is retained from the optimization case without the RF constraints. The key distinguishing feature of the RF constrained case is the localization of material towards one of the support points. Specifically, in comparison with the TO result without RF constraints support point 3 draws more load. This can be observed in comparison of Tables 4.4 and 4.5, leading to more number of branches connecting interface point 3 as illustrated in Figure 4.16 . This preference of localization resulted in the overlapping/merging of the branches and a netted region on the rear panel above support point 3.

The addition of the RF constraints has also ensured that the interface load limitations are satisfied. As tabulated in Table 4.5, the reaction forces in all the joints are within or equal to the required limits. Joints 5, 12, and 13 which previously violated these requirements were alleviated of the additional load and these loads were redirected to other joints. Noticeably to joints 14 and 15(from 12 and 13) in the upper region and: 3 and 4 (from 5) in the lower region. This phenomenon is replicated in the case with lowered resource constraint (30%) as well, as illustrated in Figure 4.18.

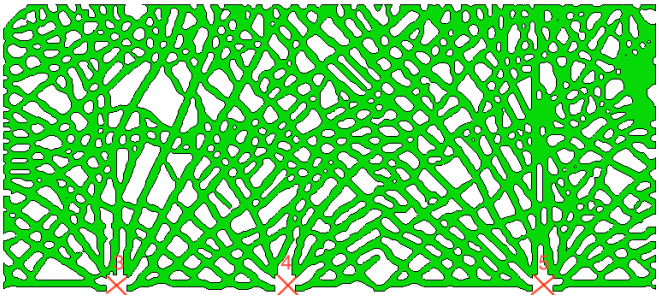

(a) Without RF constraints.

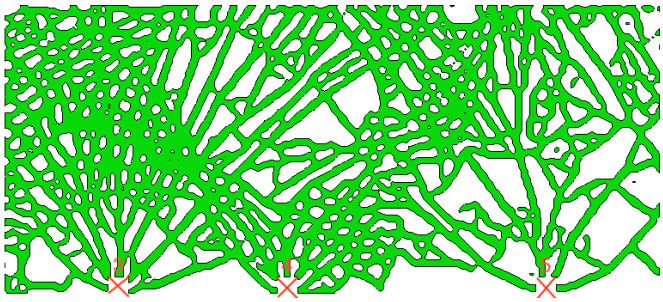

(b) with RF constraints.

Figure 4.16: TO rear panel comparison with and without RF constraints.

Joint ID	RF_X (kN)		RF_Y (kN)		RF_Z (kN)	
	min	max	min	max	min	max
1	-2.907	10.991	-2.842	0.337	-8.675	21.264
2	-1.740	9.001	-0.119	0.005	-10.360	10.534
3	-0.675	0.112	-12	9.435	-19.663	22.039
4	-0.589	0.314	-12	12	-11.870	5.825
5	-0.546	0.125	-10.381	12	-18.261	17.785
6	-2.631	12.646	-0.043	0.334	-10.765	8.55
7	-1.110	5.319	-0.152	2.328	-5.675	20.816
8	-2.462	16	-2.075	2.765	-4.778	27.888
9	-2.586	11.631	-1.181	1.567	-6.459	2.937
12	-2.483	9.887				
13	-2. 234	10.000				
14	-2.554	3.765				
15	-0.536	2.282				

Table 4.5: Max Interface loads of 6 load cases for G5 TO solution with Reaction force constraints

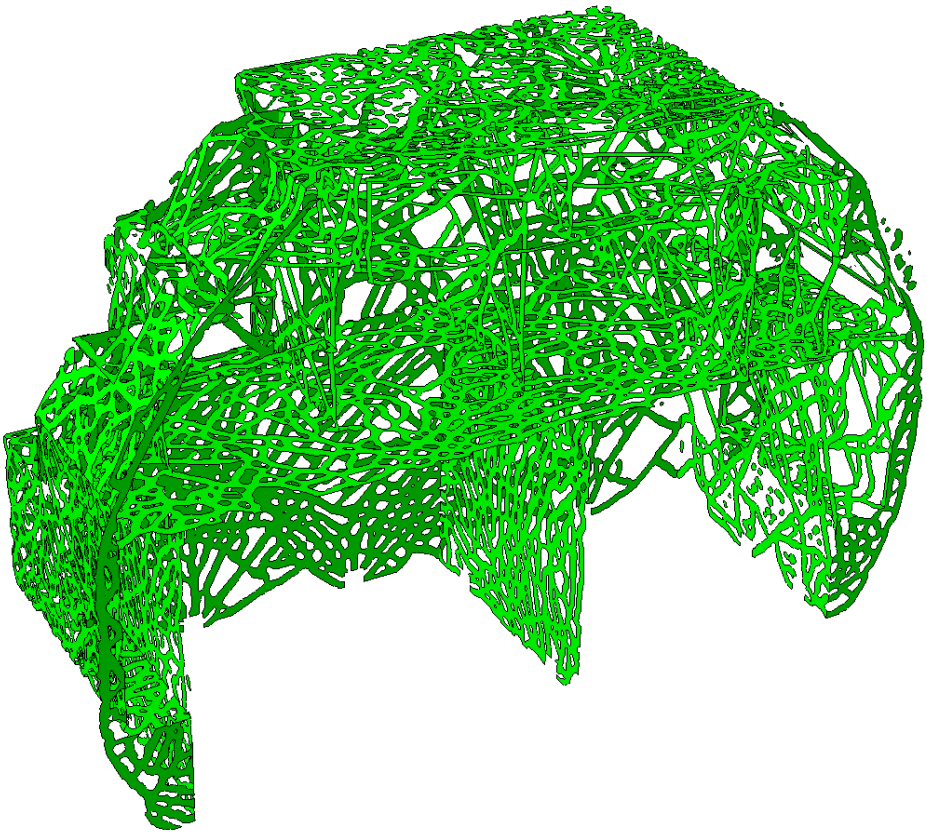

(a) 3D view.

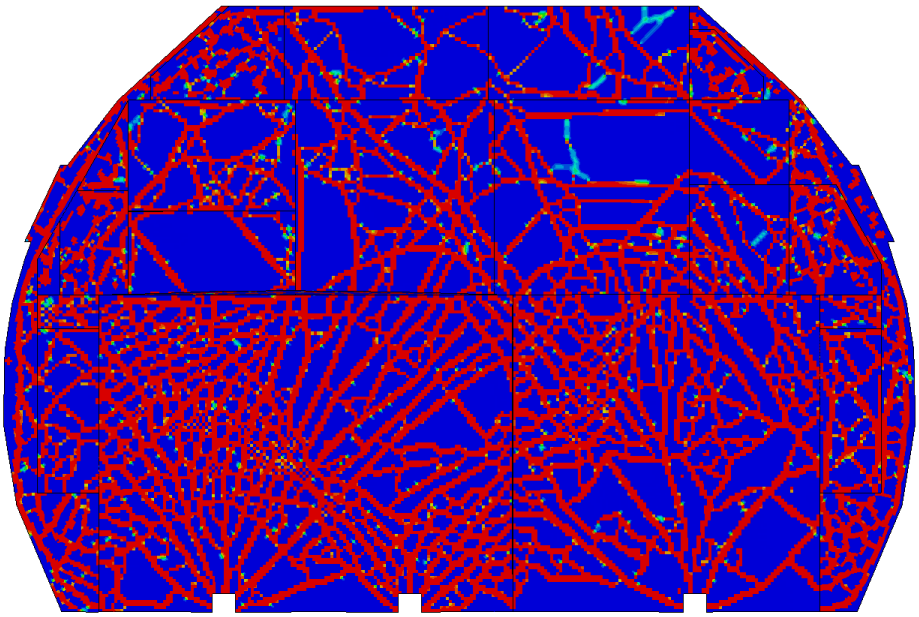

(b) Front view

Figure 4.17: Reaction force and maximum dimension constrained G5 TO result. $V_{lim} = 0.35V_0$. $SE_{optimized} = 277J$.

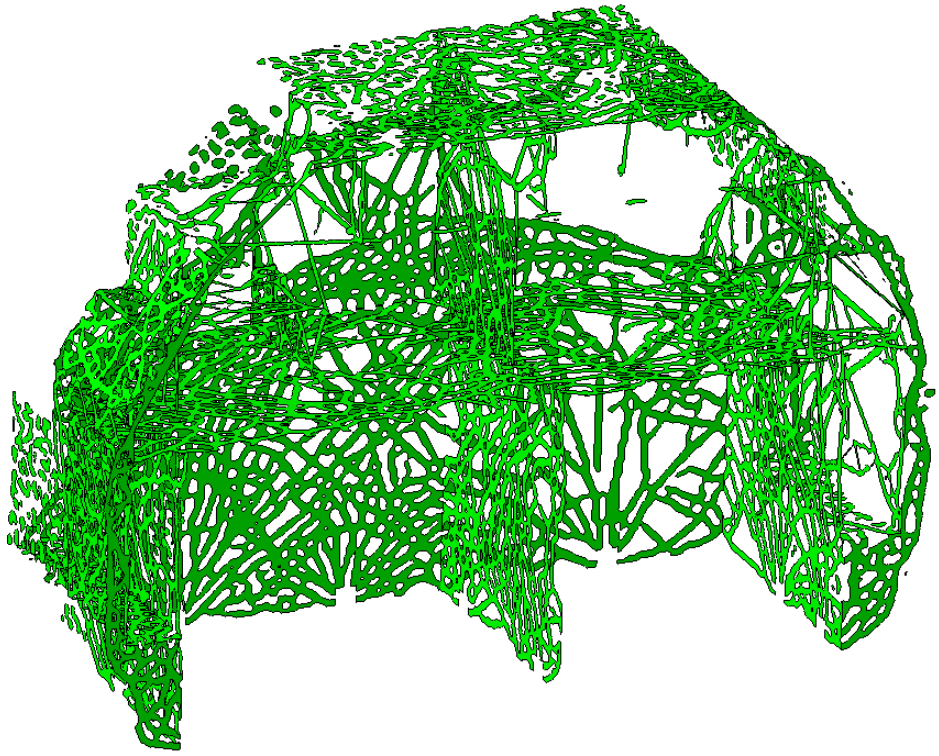

(a) 3D view.

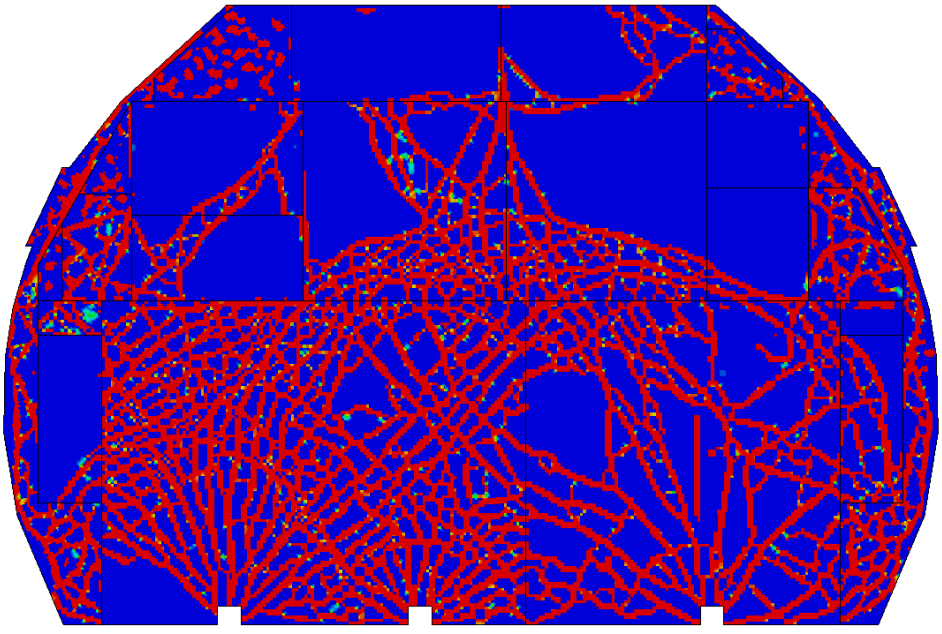

(b) Front view

Figure 4.18: Reaction force and maximum dimension constrained G5 TO result. $V_{lim} = 0.30V_0$. $SE_{optimized} = 313.23J$.

4.5. CONCLUSIONS

This chapter summarizes the modeling and optimization strategy employed for TO of a G5 galley and therefore the outcomes of the investigation of the first research question for the project.

> *How can topology optimization be employed on a galley structure? How can a suitable/practical structure be generated ?*

For the employment of TO on the G5 galley, its most barebones form is modeled within ABAQUS devoid of any inserts, fixtures, and fasteners as an assembly of S4 plate elements. This form of modeling is analogous to the strategy employed currently in house; however, a distinguishing feature of the employed TO model is the use of Aluminium as the comprising material of the galley. The use of the isotropic material allows for the use of the SIMP interpolation model for the sensitivity analysis as well as adapts the TO framework to function within the limitations of ABAQUS. To compensate for the change in material, a volume constraint is imposed on the TO objective to limit the mass of the optimized structure to the mass of the current composite galley. The volume constraint is posed on the compliance minimization objective comprising of the sum of the structural compliance under the 6 distinct loading cases. Preliminary investigations displayed a lack of functionality in the TO solutions due to the vanishing of complete panels. To this extent, suitable geometric constraints are posed to alleviate the non-uniform material removal throughout the galley and to retain a functional galley structure. The TO study is concluded with the addition of aircraft interface limitations in the form of reaction force constraints on the minimum compliance objective. The investigated modeling strategy and the assembled optimization objectives and constraints form a capable framework for the initial development of any galley. Table 4.6 describes the Author's proposition for preliminary development of TO galley solutions and represents the recommendations based on the outcomes of the investigation into the implementation of TO on the galley structure.

Element type | Mesh size	Quad Shell : S4 | 10mm
Shell Thickness	12.5 mm
Objective	minimum compliance | sum of all 6 load cases
Volume constraint	0.35 (Results in final mass equivalent to weight of current composite G5)
Material | Interpolation model	Aluminium (E=70GPa, $\nu = 0.25$) | SIMP ($0.001 \leq \rho \leq 1.000$))
Optimizer	Sensitivity based MMA | NORMAL Density update strategy
Geometric restriction	$d_{feature} \leq 30mm$
Checkerboard filter	13mm (Default for a mesh size of 10mm)
Reaction force constraints	MIN and MAX aggregation to identify critical load cases for each interface

Table 4.6: Proposed parameters for TO of galleys.

At this point, the author would like to acknowledge two critical assumptions made in the TO study. Firstly, due to the incapability of the utilized toolbox, the self-weight induced inertial forces of the galley are absent in the compliance calculations. Due to

the continually varying mass and topology of the structure, the location, as well as magnitude of the galley inertial load, do not remain constant. Therefore any pseudo inertial load applied would rather behave as an external load rather than the galley's own inertial load. Hence, once the TO solution is obtained a secondary analysis comprising of the galley inertial load is essential in validating the efficacy of the optimized solution. Secondly, material strength limitations of any form are absent in the employed optimization scheme. The Author would like to mention that, a preliminary study with stress limitations was conducted and is available in the Appendix. However, in the interest of computational expense and keeping within the scope of the project, this aspect has been omitted and is proposed for further study.

5

MODULARITY

This chapter briefly introduces the concept of modularity and its influence. Section 5.1 and Section 5.2 describe the studied effects of modularity on performance and cost respectively. The common strategies to extract features from TO-generated solutions are explored in Section 5.3 and Section 5.4 briefly describes the concept of shape matching using image moments.

Although the term 'Modularity' is used in various forms, in its most basic form it refers to the ability of a structure to be broken down into smaller parts that are independent of each other [66]. The most notable influence of the modular design approach in the commercial market was encountered in the automotive industry. Both Ford and GM augmented their manufacturing tactics to modular assembly strategies to allow for more efficient manufacturing in 1999. Although primarily used as a measure to simplify manufacturing and offer cost-effective products to the market an added customer benefit was realized: customization. Hence, modularization became a suitable method for large-scale production while simultaneously offering variety. However, the modular design philosophy is not limited to structural division and assembly. In its more prevalent form modularization implies the utilization of sub-structures that are similar to each other. As defined by Kamrani and Nasr, modular design is a design technique that can be used to develop complex products using similar components [60]. This form of modularization is best represented by the iconic LEGO^{TM} blocks which are infamous for their portfolio of similar blocks and their capability to achieve complex macro structures [1].

The set of LEGO blocks is an ideal example of the capability of similar substructures and their inherent manufacturing advantages. The product has not only been a source of various designs, but also an interesting case of manufacturing quality control. All products manufactured from 1958 to date are compatible and are manufactured with a tolerance of 0.01mm [6]. This can be attributed to the focus of design being constrained to a limited set of smaller, simpler, and similar parts. The minimization of focus on manufacturing limited to a set of identical parts avails the opportunity to focus efforts on mitigating auxiliary costs induced by part variety. Within the scope of this project, this more evolved definition of modularity will be adopted.

Within the scope of TO, the generated structures are typically monolithic in nature and their complex topologies require specialized manufacturing strategies. This is predominantly achieved through machining of a single block of material [64] ,casting [59] or 3D printing [15]. These manufacturing strategies considering the complex topologies of the structures limit the manufacturing quantities to a large extent due to the economic consequences. Although the geometric constraints described in Section 3.1 allows for some degree of control on the topological complexities, from a mass production perspective TO solutions require a more rigorous augmentation methodology.

Modularity offers a possible solution to bridge this gap of complexity over quantity. The high-performing TO monoliths if augmented into similar/identical substructures can provide efficient manufacturing capabilities. However, the diminishing influence of modularity of performance cannot be ignored. Therefore, the modular philosophy becomes a balancing act between performance and cost. The functional variables being, the size of the sub-components, their variety, and their individual quantity.

5.1. MODULARITY AND PERFORMANCE

The performance of any assembled structure is inferior to its parent-monolithic structure, this effect is well embodied in the comparison of welded and bolted joints [71]. However, to study the effect of the modules on the performance of the assembled structures, this drop in performance needs to be solely attributed to the modules themselves rather than the interfacing consequences. A relevant case to study to understand this influence of modules on the monolith is truss optimization.

The use of a limited variety of design variables in construction is analogous to truss topology design with discrete variables [126][73]. This constrained version of the truss sizing problem naturally results in sub-optimal solutions in comparison to free sizing solutions; However, it is more representative of a practical truss sizing where truss or beam dimensions are limited. Enrique Herencia et al. showed that for a given load case, the weight of a truss increase as the number of discrete variables is reduced [45]. Thus illustrating a decrease in specific performance as the number of distinct modules is reduced. This behavior is illustrated in Figure 5.1, where the decaying effect of weight decrease with respect to an increased number of discrete variables is an interesting finding. This behavior allows possibilities for standardization of parts without increasing the weight significantly above the optimal, in this case limiting to 3-4 design variants.

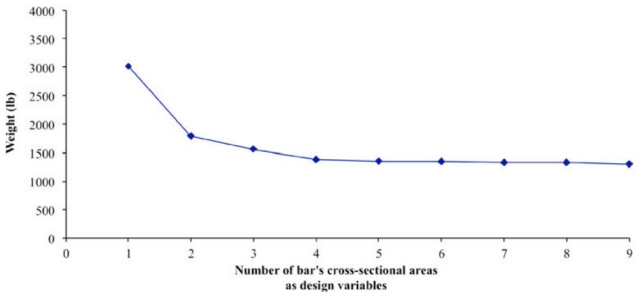

Figure 5.1: Weight of weight-optimized 10 bar truss structure vs the number of allowed cross-section areas (Enrique Herencia et al. [45]).

The effect of module scale on global optimal is not easily measured in truss optimization but can be inferred in periodicity studies in TO. This phenomenon is represented in the TO of periodic materials [55] and in the design of material microstructures [122]. As the scale of the modules decreases, it is observed that the stiffness reduces rapidly (compliance increases). Similar behavior is observed in the design of macro structures [81][58]. Jiang and Wu utilized this methodology to design modular energy storage flywheels [58]. As the periodicity in the domain is increased, a progressive drop in performance (increase in compliance) is exhibited and over a point of division, the compliance approaches a constant value. This implies, if the initial monolithic design is over-designed, the modularized design can be adapted to fall within required performance metrics. Analogous behavior was noted by Hao Zuo et al. in the influence of

periodicity on the natural frequency of periodic topologies. The natural frequency initially drops as the periodicity is increased and approaches a constant value for further increase [52]. This reiterates the detrimental effect of modularity on performance as well as the decaying effect of the increase in performance with an increase in available design variables.

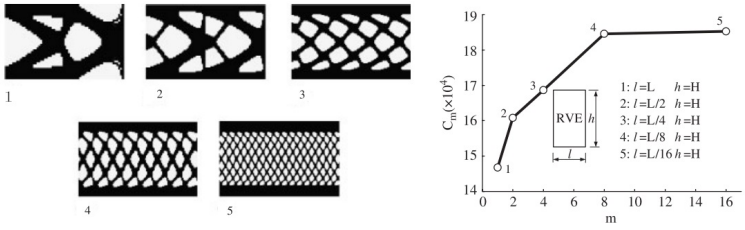

(a) Compliance increase with size decrease (or increased modularity) (Zhang and Sun [122]).

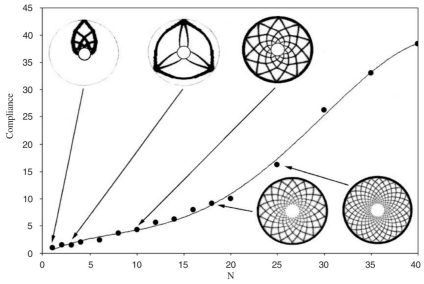

(b) Decaying effect of drop in performance with increase in modularity (Moses et al. [81]).

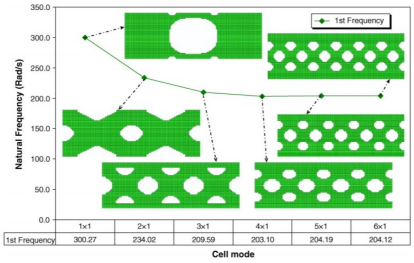

(c) Decaying effect of drop in natural frequency with increase in modularity (Hao Zuo et al. [52]).

Figure 5.2: Illustration of influence of constructional modularity on performance (compliance) and natural frequency.

It is interesting to note that modular variety itself has a secondary variation within it where the number of modules of each type themselves can decide the performance. An increase in the variety of parts allows for better performance due to being closer to the free sizing optima. If instead of the size and variety of modules, the total number of a module itself were studied, intuitively we can predict that the performance must increase with the increase in the number of allowed modules. This phenomenon was studied by Asadpoure et al., with a fixed ground structure, the performance of the optimum truss was compared for varying numbers of allowed members [14]. The study showed an initial increase in performance(decrease in max deflection) and as the allowable members were increased the performance increase decays, as illustrated in Figure 5.3. A similar study with respect to the number of parts to be replaced by a common module was conducted by Van Gent and Kassapoglou. The study provides a practical example of an airframe structure, where its weight is studied as the number of unique stiffeners are replaced by common designs, shown in Figure 5.4. The weight of the fuselage is shown to increase as the number of unique stiffeners are increased.

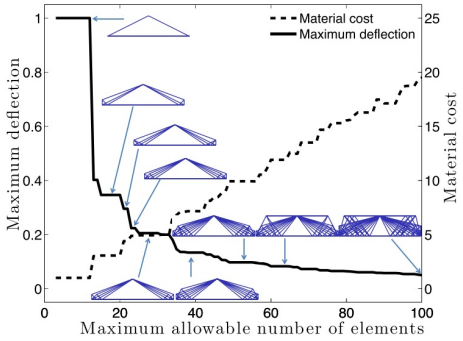

Figure 5.3: Opposing behaviour of maximum deflection and cost(material) with respect to number of truss elements allowed (Asadpoure et al. [14]).

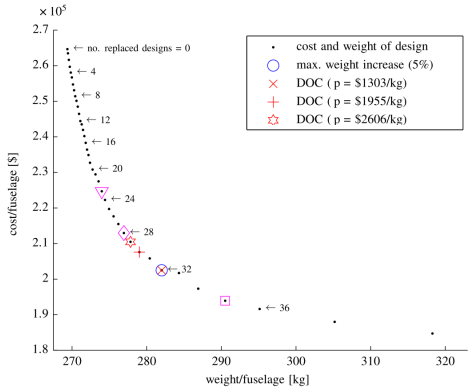

Figure 5.4: cost vs weight vs no. of replaced designs for constant load requirements for fuselage stiffener designs. DOC : Direct operating cost (Van Gent and Kassapoglou [110]).

Figure 5.4 is an ideal depiction of the break-even analysis required in any modularization intention. The increase in weight is accompanied by a noticeable decrease in manufacturing cost, the possibility of economic advantage is one of the key motivations for any modularization campaign apart from the ease in manufacturing. Modularization can thus be a useful strategy when the loss in performance can be outweighed by the economic advantage in manufacturing.

5.2. MODULARITY AND COST

Modularity in design if performed responsibly can lead to simple design architectures without a significant drop in performance. But, the major interest in modularity is in its ability to reduce manufacturing costs. The major manufacturing costs can broadly be

defined into 3 parts: labor, tooling, and material. The relation between modularity and labor cost is explained through the quantity and cost relationship. As quantity increases, the mode of manufacturing is modified from manual labor to more automated systems which leads to long term cost savings [31], see figure 5.5a.

It is to be noted that although a unit cost reduction exists a conglomeration of the modular units is what is required to manufacture an entire structure. Hence, it is only discretization over a break-even point that allows for the labor cost to be regained.

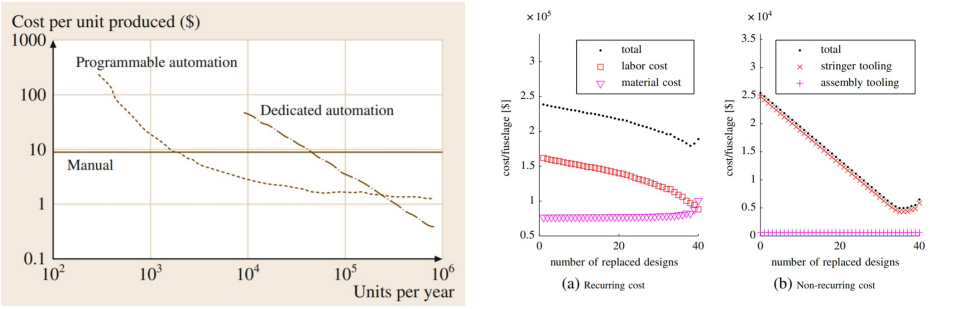

(a) Comparision of manufacturing costs per unit for different manufacturing methods (Ceroni [31]).

(b) Influence of modularity on labour and tooling cost (Van Gent and Kassapoglou [110]).

Figure 5.5: Manufacturing cost variation with respect to production volume.

Van Gent and Kassapoglou illustrated the influence of modularity on labor and tooling costs. The increased modularity is shown to reduce labor costs as well as reduce tooling costs. Interestingly, the converse argument of using an objective function that mimics the cost increase due to extra parts is shown to produce designs with a fewer number of part variants [14]. Apostolopoulos and Kassapoglou showed that for a given composite laminate the cost of manufacturing is minimized when the laminate is constructed through an assembly of smaller laminates. The reduction in cost is attributed to the learning curve resulting in a reduced cost with each successive module. For a specific size of modules, the decrease in cost bypasses the increased cost of assembly, hence achieving profits through low size constructional modularity [13]. Axillary costs such as certification and maintenance are also reduced through constructional modularization. When coupled with automated non-destructive testing methods, the minimum flaw size for detection and the scanning probe travel dimensions optimum module size can be estimated [61].

A good description of the variation of the cost breakdown with modularity is provided by Van Gent and Kassapoglou for the design of fuselage stiffeners (see figure 5.6). The major contribution is taken over by the material cost due to the increase in material and the accompanying costs of labor and assembly decrease. A decrease in tooling cost can be attributed to the requirement of simpler or fewer tools for manufacturing fewer variants of modules. In this case learning curve effects also contributed to the decrease in manufacturing costs. As the modularity becomes excessive, the material costs over-

take the tooling and labor costs. At higher levels of modularity, the tool life and other maintenance costs are also factors to be considered. This allows for a cost-weight trade off analysis to be performed as illustrated in Figure 5.4. However, under more complex loading cases, the drop in cost with increase in modularity is not consistent. This is illustrated in Figure 5.7, where the material cost increase is larger than the tooling cost drop leading to an increase in cost as well as weight. Therefore, a range of modularity can be identified within which the increase in weight can be countered with the cost reduction. Specifically in Figure 5.7, 6 to 21 replaced designs are the limited region within which a cost reduction can be obtained.

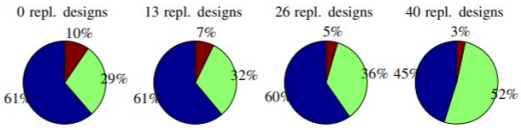

Figure 5.6: Cost breakdown at different levels of modularity (blue: labor, green: material, red: tooling) (Van Gent and Kassapoglou [110]).

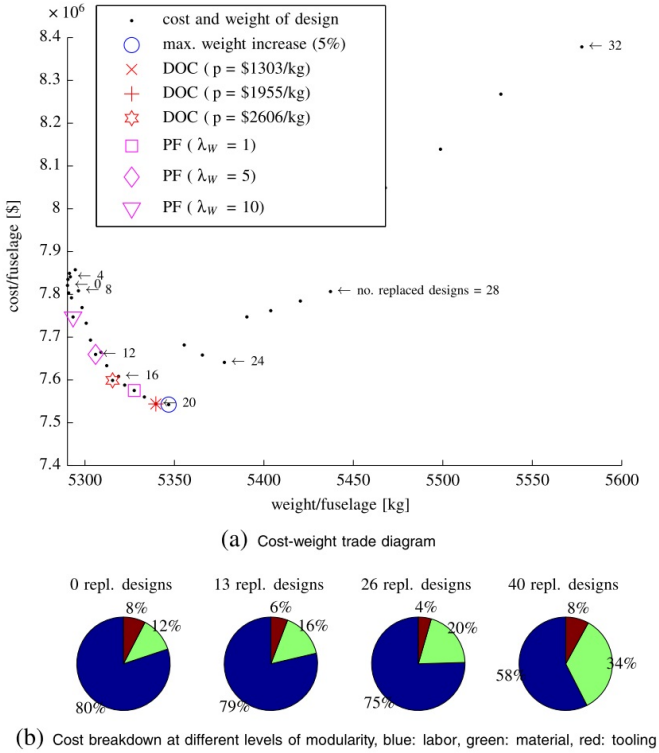

Figure 5.7: Cost-weight trade diagram (Van Gent and Kassapoglou [110]).

5.3. MODULARIZATION OF TOPOLOGY OPTIMIZED STRUCTURES

As described in Section 3.1, TO is the global optimization of a domain leading to a design that assumes a highly flexible manufacturing method, capable of realizing structures with any configuration of material distribution. In practice, manufacturing limitations such as tool accessibility, tool maneuverability, etc limit the capabilities to achieve such designs. In most cases, the complexities can be simplified with additional constraints on the optimization routine (dimensional, curvature, etc). Nonetheless, this inevitably leads to a drop in performance and in most cases remains inaccessible for mass production due to the higher cost incurred. Therefore, the fragmentation of such complex structures is an essential postprocessing operation to relax manufacturing as well as economic constraints.

An ideal example of fragmentation of complex structures is the partition wall designed by Nagy et al. in collaboration with AIRBUS [83] [5]. The crisscross truss design generated was initially modeled as a uni-body structure, however, it was then broken down into multiple pieces and manufactured individually. The process of the division was entirely manual and each piece was further shape and size optimized with a mammal bone-based internal structure [3], leading to 3D printing of each individual piece.

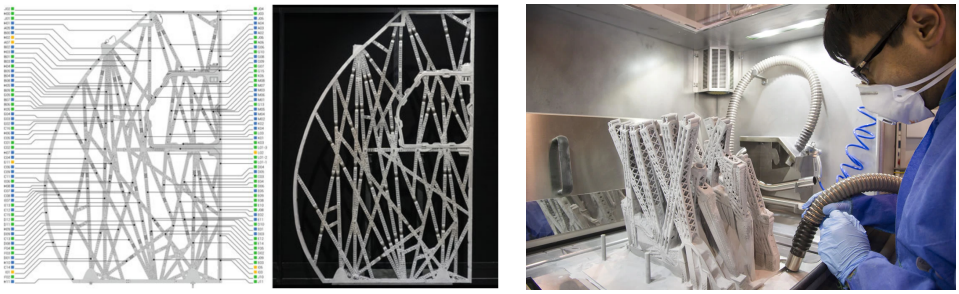

(a) Modularization of the complex partition wall structure.

(b) 3D printing of fragments.

Figure 5.8: Modularization of complex partition structure (Nagy et al. [83]).

Although it is quite pleasing to visualize an industry where everything is 3D printed, the technology is currently still in its infancy from a mass production perspective. Nevertheless, fragmentation does allow for TO solutions to be utilized as initial design ideas to be post-processed for conventional manufacturing. The most simple method commonly used to extract features from TO solutions is the image interpretation approach where features are drawn by experienced designers over TO results [86]. However, such a method requires manual interactions which are followed by further shape optimization which is a complex optimization feat on its own. A more general image interpretation method was proposed by Lin and Chao where thresholded topologies are used to identify boundaries of internal holes [34][76]. However, methods employing feature identi-

fication methods require frequent interaction and in most cases rely on experience for successful extraction [120]. Other automated reconstruction methods focus on matching boundaries using free form surfaces such as B-Spline curves [87]. Although such methods can be used to describe complex surfaces suitable for additive manufacturing, the obtained designs remain expensive for manufacturing with traditional subtractive manufacturing or even assembly-based manufacturing [120]. Additionally, these strategies do not execute fragmentation of any kind, therefore the TO solution is simplified while retaining a single-piece structure.

One of the frequently employed methods which achieve manufacturing simplicity as well as modularization to some extent is the extraction of truss/frame designs from low volume fraction TO solutions. Commonly employed in Civil Engineering [116], TO is used to generate suitable Strut and Tie models(STM) for the design of reinforcements for concrete structures. The typical strategy involves a thinning process, where a single pixel/element skeleton of the obtained TO solution is generated followed by the node identification method where the endpoints of the truss elements are identified and connected through suitably sized truss elements. By limiting the truss profiles to a set of discrete design variables, the STM embodies to a large extent the modular design philosophy.

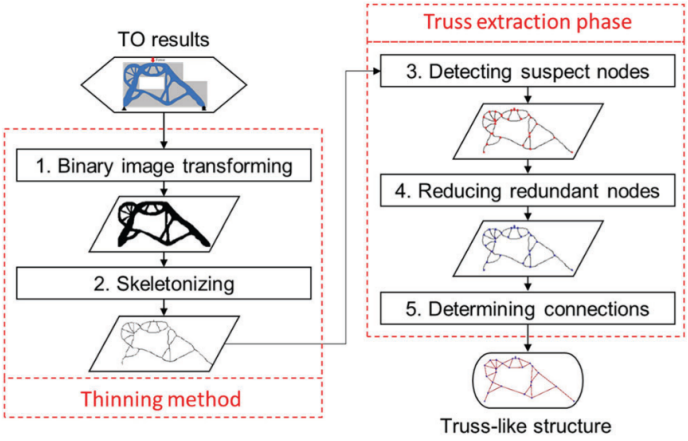

Figure 5.9: Strut and Tie model extraction process using thinning (Xia et al. [116]).

Truss/frame structures are by their very nature fragmented and within the realm of structural engineering, their design represents the most iconic form of design optimization. Researched extensively for over a decade [80], truss optimization has undergone significant evolution [22]. In the pioneering works of Dorn et al., a method to evaluate optimal truss topologies was established, which is still employed [37]. The methodology is often called the ground structure(GS) approach which employs a grid of points in the domain which are interconnected by truss members to varying degrees. The optimal truss solution is obtained through sizing of the connecting truss members, which also

allows for the vanishing of the truss members. To obtain a solution closer to the global optimal, a large number of points are required in the GS leading to a drastic increase in the computational requirements. An alternate route is through a fixed interconnected set of points and the optimization of the coordinates of said points often referred to as truss geometry optimization [36]. However, from a broader perspective, the most practical form of truss optimization is one where both sizing and geometry are simultaneously optimized and where truss sizes are discrete in variety[10]. This broader form of the problem is one that could theoretically provide the best truss, yet its complexity limits its usage to fairly simple employments. However, topology optimization provides the capability to simultaneously obtain the optimal size and topology and is computationally more efficient to truss optimization, and offers versatility to be adapted to a wide range of structures. Nevertheless, the modularity offered by truss optimization is not retained through TO.

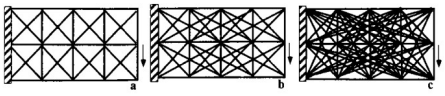

(a) Varying levels of ground structure connectivity.

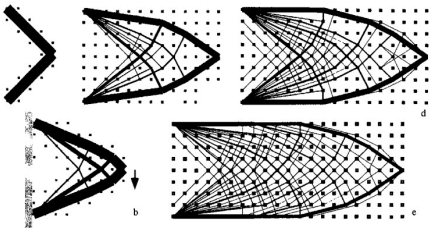

(b) Influence of initial ground-structure on the solution obtained to the optimization problem.

Figure 5.10: Ground structure approach to truss optimization (Bendøse and Sigmund[17]).

Studying the G5 TO solution from chapter 4, a noticeable similarity is found between the low volume fraction TO solution and skeletal truss/frame-based architectures. Therefore, an intuitive leap can be made that truss/frame-based design could prove to be a suitable translation of the TO solution to a modular design. However, one could question if a truss/frame-based structure can perform on par with Panel based designs, especially within the context of the project study case of an aircraft galley. However, the partition wall designed by AIRBUS represents an example of the very same [83][3]. The frame like design was 45% lighter than previous designs while simultaneously increasing its performance. Although the parts themselves were manufactured through additive manufacturing, the structure itself proves the capability of a truss/frame structure to replace a panel-based cabin structure.

The standard STM extraction strategy functions based on regular quad meshing and on simple design domains [116]. As the domain complexity increases and meshing varies, this method can fall short. Additionally from a broader perspective, the use of mesh dependant strategies largely limits the scope of module identification. The very act of identifying skeletal truss/frame architectures in a TO solution is analogous to shape identification in images. The identification of shapes embodies the same philosophy as modularization where a number of simpler modules suitably arranged can achieve the

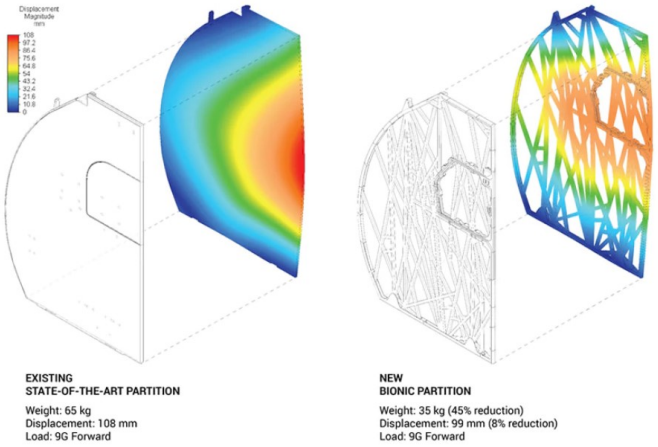

Figure 5.11: Performance of truss-based bionic partition as compared to initial panel-based structure [3]

same goal as the assembly as a whole. Therefore, image processing-based shape matching could provide an alternate route to the modularization of TO solutions.

5.4. IMAGE MOMENT BASED SHAPE MATCHING

The piece-wise density distribution of TO solutions largely resembles the pixel-wise intensity distribution of digital images. Therefore, an intuitive proposition can be made that methods developed within image processing can be adopted suitably for processing TO solutions. Within the context of this project, the requirement of the process involves the extraction of the position and shapes of simple modules within a TO solution. This can be visualized as identifying the best fitting shapes and their positions within an image. Or if the modules themselves are fixed in shape/feature this can be equated to the best fitting positions of a set of shapes within a domain to approximate the underlying image. The prevalent methods employed for shape/ object identification and detection either rely on Machine learning or Deep learning-based approaches [115]. Such systems rely on large data banks as a source of information to train the computational model. In the interest of using a data-independent methodology, a purely mathematical comparison formulation is preferred. One such method is through image moments.

Image moments are a set of descriptors of 2D/3D images. The concept was first put forward by Hu. The Hu-moments are a set of descriptors that are invariant to translation, scale, rotation, and mirroring [54]. The Hu moments are based on geometric moments. The geometric moments are capable of identifying features such as area, centroid, and orientation but they are incapable of direct image reconstruction and the contributions of higher-order geometric moments are not easily comprehendible [107]. Teague proposed the use of orthogonal functional moments in place of geometric moments for the

first time. Their orthogonal properties allow for reconstruction of the image and also for each moment to capture unique non-overlapping information from the image. The two continuous orthogonal functions proposed were Zernike polynomials and Legendre polynomials[107]. Since then, image moments have been developed and studied for their image characterizing capabilities[108].

Figure 5.12: Image reconstruction using Legendre polynomials (Chiang and Liao [33]).

Legendre polynomials are ideal in this case since their rectangular orthogonality domain follows the shapes of the panels in the structure. Each panel can be considered as an individual image and the corresponding Legendre moments can be used for their modularization. Since we aim to investigate the presence of certain similar modules within each panel, the question becomes what kind of modules. In this case, as obtained in Chapter 4, the TO solution obtained is one with slender members. This is quite analogous to truss structures or more specifically a frame structure. Therefore a bar/beam-based module identification would be well suited for the initial study. Additionally, although the lengths of the bar elements can vary, their cross sections if enforced to be constant can still embody a very basic form of modularity.

In summary, modularization of complex monoliths allows for simplification in manufacturing and additional profitability. Therefore, the TO solution if adapted into a modularized design can prove to be competent for large-scale employment. The congruence of TO solutions to digital images allows for shape matching strategies to be translated into modularization techniques for TO solutions. Therefore based on the Legendre image moments from image processing, a framework will be investigated to extract bar/beam-based modularized designs from TO solutions.

6

MODULE IDENTIFICATION IN TOPOLOGY OPTIMIZATION SOLUTIONS USING IMAGE MOMENTS

This chapter comprises an investigation into the image moment-based modularization strategy. Section 6.1 describes the principle of Legendre image moments followed by Section 6.2 which describes the moment matching strategy proposed to identify bar positions within a domain. Section 6.3 and 6.4 describe the results from the global bar matching. The nature of the objective and its nonlinearities is studied in detail in Section 6.5. Section 6.6, 6.7 and 6.8 describe the sequential augmentation of the moment matching strategy.

6.1. LEGENDRE MOMENTS

Topology optimization performed using FEM, results in a structure being described by a piece-wise intensity distribution described by the finite element mesh. This is analogous to digital images where an image is described in pixelated form. As described in Section 5.4, within the field of image processing a common method used to represent an image is using image moments. Image moments are a finite set of image descriptors that are used to describe an image [9]. These image moments are not only capable of describing and reconstructing an image but are also capable of distinguishing images. Of this subsidiary technique of image processing, Legendre moments are a 2D equivalent of the 1D-Legendre polynomial curve fitting method. Similar to which, an image can be approximated using a set of Legendre polynomials(in 2D). Based on the Legendre polynomials, the Legendre moments for 2D images are given by (6.1) where Δx and Δy are the sampling intervals within a pixel.

$$\lambda_{mn} = \frac{(2m+1)(2n+1)}{4} \sum_{x} \sum_{y} P_m(x) P_n(y) f(x,y) \Delta x \Delta y \tag{6.1}$$

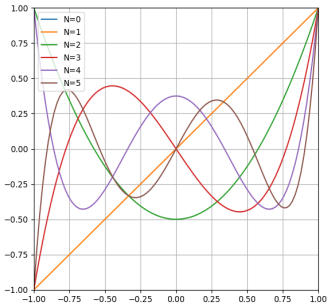

Figure 6.1: Legendre curves

Table 6.1: Legendre polynomials

n	$P_n(x)$
0	1
1	x
2	$(3x^2-1)/2$
3	$(5x^3-3x)/2$
4	$(35x^4-30x^2+3)/8$
5	$(63x^5-70x^3+15x)/8$

The digital image can be reconstructed using the Legendre moments as a continuous function given by:

$$f_{reconstructed} \approx \sum_{i=0}^{i=m} \sum_{j=0}^{j=n} \lambda_{ij} P_i(x) P_j(y) \tag{6.2}$$

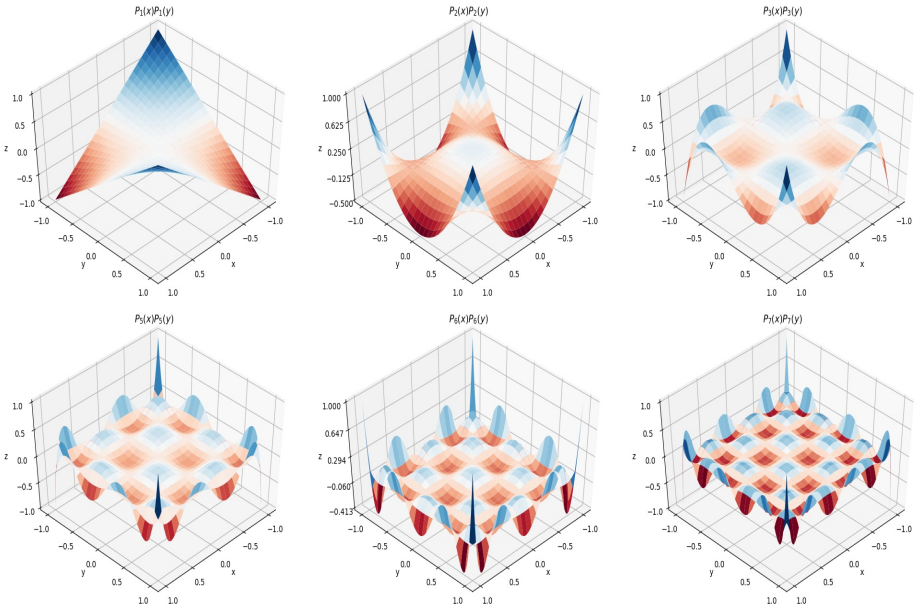

Figure 6.2: 2D Legendre functions $P_1(x)P_1(y)$, $P_2(x)P_2(y)$, $P_3(x)P_3(y)$, $P_5(x)P_5(y)$, $P_6(x)P_6(y)$, and $P_7(x)P_7(y)$

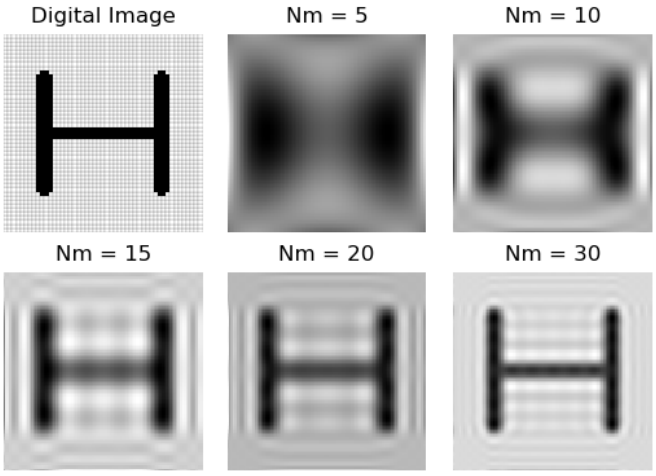

Figure 6.3: 2400 pixel image reconstruction using Legendre moments up-to order 5, 10, 15, 20, and 30.

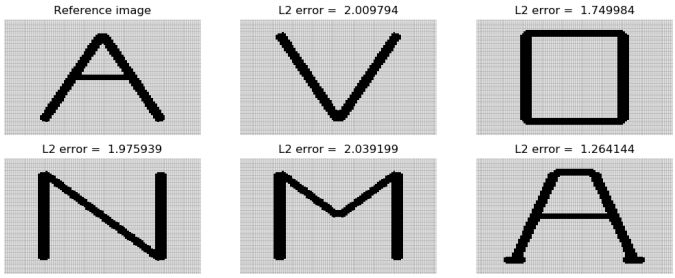

Figure 6.4: L2 error in comparison to the reference image:A for letters V, O, N, M, and a slightly different A. Moment matrix size utilized = 10x10

Through the use of these moments, the information from a multi-pixel image is stored as a set of image descriptors. These moments can not only be used to reconstruct an image as illustrated in Figure 6.3 but can also be used to compare images as illustrated in Figure 6.4. The difference between the Legendre moments of the two cases is maximized with the difference between the images. Consider the letter A and V which are approximate mirror images about the X axis, hence the error is maximized. And of course, as the similarities increase, the error is minimized. This is observed in the comparison of the two different forms of the letter 'A'.

6

ORTHOGONALITY

Since the Legendre polynomials are orthogonal in nature, this implies that any image can be reproduced theoretically by the Legendre polynomial set and must theoretically be complete. This also ensures that any 2 complete Legendre moment sets must not be identical unless the images are identical. However, in the context of digital images a truly complete set of moments is not possible due to its piece-wise nature. Therefore, as a corollary: In the case of incomplete or limited sets of Legendre moments, identical moments implies that images must be similar.

Following along these lines, it is hypothesized:

> *Given the Legendre moments of a TO solution, and the Legendre moments of a bar as a function of its coordinates, orientation, and dimensions, by matching the corresponding moments, the equivalent/approximate positions of the bars can be identified.*

To this extent, the following sections investigate a methodology to use Legendre moments to extract the positions of a set of bars within a work space to approximate a structure obtained from topology optimization.

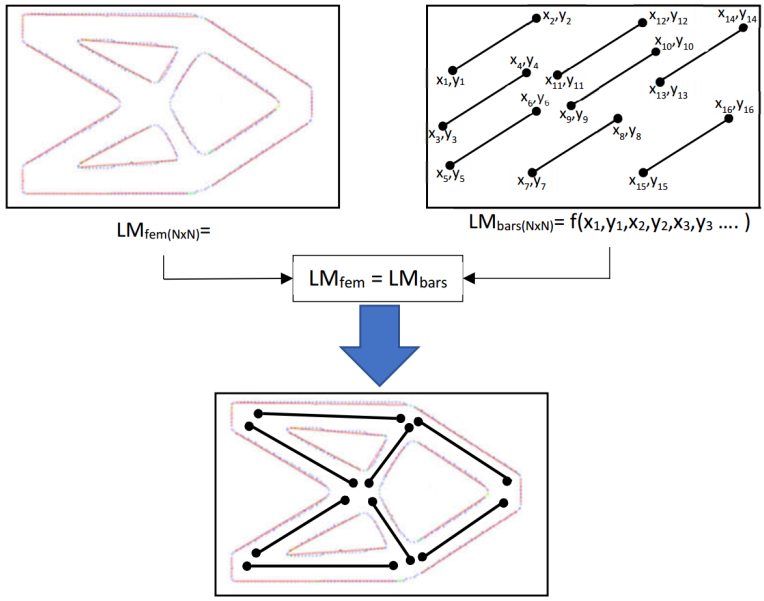

Figure 6.5: Moment matching hypothesis

6.2. MOMENT MATCHING

The results from TO using FEM, although results in a similar illustration as that of digital images, the latter are entirely limited to identically sized grid-based pixels in high resolution. Equation 6.1 is an approximation which is suited for digital images. To suit all possible mesh schemes, the more accurate integral form is utilized to compute the Legendre moments given by Equation 6.3.

$$\lambda_{mn} = \frac{(2m+1)(2n+1)}{4} \int_{-1}^{1}\int_{-1}^{1} P_m(x)P_n(y)f(x,y)dxdy \tag{6.3}$$

The Legendre moment for the bar is calculated similarly by limiting the integration domain within the bar. Given the central coordinate of the bar of thickness W is given by x_0, y_0, length L and inclined at an angle θ. The Legendre moment for the bar is given by Equation 6.4. The analytical expressions for bar moment value up to $\lambda_{10,10}$ are obtained as a function of the bar properties using Sympy[79]. A subset of which are tabulated in Table 6.2. A reconstruction of a sample bar is conducted in Figure 6.6.

$$\lambda_{mn} = \frac{(2m+1)(2n+1)}{4} \int_{-\frac{W}{2}}^{\frac{W}{2}}\int_{-\frac{L}{2}}^{\frac{L}{2}} P_m(x_0 + l\cos\theta - w\sin\theta)P_n(y_0 + l\sin\theta + w\cos\theta)dldw \tag{6.4}$$

m	n	$\lambda_{mn}(x_0, y_0, L, W, \theta)$
0	0	$0.25LW$
0	1	$0.75LWy_0$
1	0	$0.75LWx_0$
1	1	$0.1875L^3W\sin\theta\ cos\theta + L(-0.1875W^3\sin\theta\cos\theta + 2.25Wx_0y_0)$
1	2	$L^3(1.875Wx_0\sin^2\theta + 3.75Wy_0\sin\theta\cos\theta)/4 + L(0.46875W^3x_0\cos^2\theta$ $-0.9375W^3y_0\sin\theta\cos\theta + 5.625Wx_0y_0^2 - 1.875Wx_0)$
1	3	$0.1640625L^5W\sin^3\theta\cos\theta + L^3(-1.09375W^3\sin^3\theta\cos\theta + 1.09375W^3\sin\theta\cos^3\theta$ $+13.125Wx_0y_0\sin^2\theta + 13.125Wy_0^2 * \sin\theta\cos\theta - 2.625W\sin\theta\cos\theta)/4$ $+L(-0.1640625W^5\sin\theta\cos^3\theta + 3.28125W^3x_0y_0\cos^2\theta$ $-3.28125W^3y_0^2\sin\theta\cos\theta + 0.65625W^3\sin\theta\cos\theta + 13.125Wx_0y_0^3 - 7.875Wx_0y_0)$

Table 6.2: Bar Legendre moments

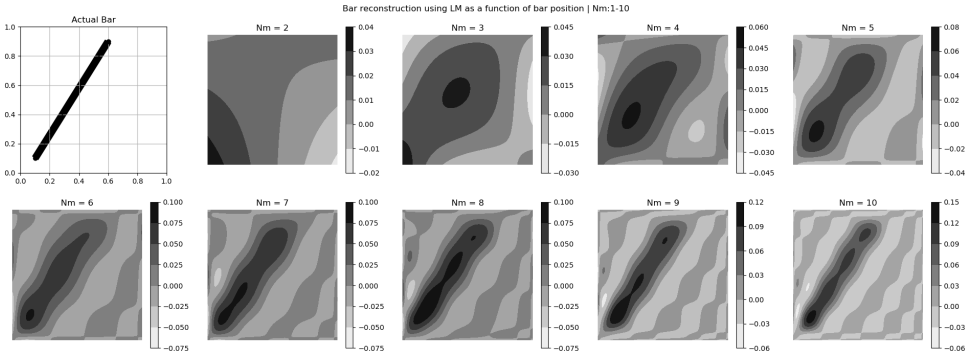

Figure 6.6: Bar reconstruction using bar moment equations : Nm = 2 ⇒4 terms , Nm=10 ⇒ 100 terms

It is to be noted that to ensure that the Legendre polynomials are utilized only within their orthogonal regions(-1,1), the functions are remapped from a [-1,1] bounding box to a D[$(X_L, X_U), (Y_L, Y_U)$] bounding box for general FEM solution. This is done to maintain a direct relationship between the dimensions of the structure and its elements(bars). All the expressions in table 6.2 are limited to variables which result in the bar entirely being within the [(-1,1),(1,1)] bounding box. Hence to convert them to a more general and convenient form, the variables are transformed to an endpoint formulation and are multiplied by suitable Jacobians. Given a general bounding box D[$(X_L, X_U), (Y_L, Y_U)$], a linear remapping is performed to obtain the corresponding location in the D[(-1,1),(-1,1)] Legendre domain.

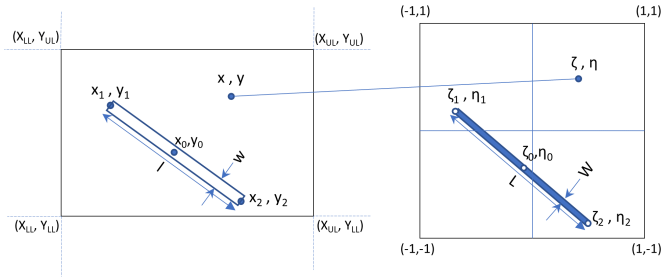

Figure 6.7: Mapping for generalized Legendre moment calculation.

$$\zeta = \frac{2x - X_{UL} - X_{LL}}{X_{UL} - X_{LL}}, \eta = \frac{2y - Y_{UL} - Y_{LL}}{Y_{UL} - Y_{LL}} \tag{6.5}$$

$$\lambda_{mn} = \frac{(2m+1)(2n+1)}{4} \int_{X_L}^{X_U} \int_{Y_L}^{Y_U} P_m\left(\frac{2x - X_L - X_U}{X_U - X_L}\right) P_n\left(\frac{2y - Y_L - Y_U}{Y_U - Y_L}\right) f(x,y)\,dx\,dy \tag{6.6}$$

The variables for the bar$(\zeta_0, \eta_0, L, W, \theta)$ are converted to an endpoint formulation(x_1, y_1, x_2, y_2, w) using (eqendp).

$$\begin{aligned}
\zeta_0 &= \frac{\zeta_1 + \zeta_2}{2}, \eta_0 = \frac{\eta_1 + \eta_2}{2} \\
L &= \sqrt{(\zeta_2 - \zeta_1)^2 + (\eta_2 - \eta_1)^2} \\
\alpha &= \tan^{-1}\left(\frac{y_2 - y_1}{x_2 - x_1}\right), \theta = \tan^{-1}\left(\frac{\eta_2 - \eta_1}{\zeta_2 - \zeta_1}\right) \\
J_W &= \frac{1}{2\sqrt{\frac{\sin^2\alpha}{(X_{UL} - X_{LL})^2} + \frac{\cos^2\alpha}{(Y_{UL} - Y_{LL})^2}}} \\
J_L &= \frac{1}{2\sqrt{\frac{\cos^2\alpha}{(X_{UL} - X_{LL})^2} + \frac{\sin^2\alpha}{(Y_{UL} - Y_{LL})^2}}} \\
W &= \frac{w}{J_W}
\end{aligned} \tag{6.7}$$

The generalized bar moment is given by Equation 6.8.

$$\Lambda_{mn}(x_1, y_1, x_2, y_2, w) = J_W \times J_L \times \lambda_{mn}(\zeta_0, \eta_0, L, W, \theta) \tag{6.8}$$

The computed set of Legendre moments are operated and analyzed in the form of a Legendre moment matrix(LM). The moment matrix of size $N_m = 3$ is given by Equation 6.9.

$$\left[LM_{3\times3}\right] = \begin{bmatrix} \Lambda_{0,0} & \Lambda_{0,1} & \Lambda_{0,2} \\ \Lambda_{1,0} & \Lambda_{1,1} & \Lambda_{1,2} \\ \Lambda_{2,0} & \Lambda_{2,1} & \Lambda_{2,2} \end{bmatrix} \tag{6.9}$$

A common method to compare two matrices is using the Euclidean distance or the L2 norm of the difference matrix(L2E) given by Equation 6.10, i.e, the L2 norm is to be minimized for two matrices to be similar. This is the error formulation utilized in Figure 6.4. A preliminary study is conducted to assess the viability of using L2 norm distribution for comparison of the moments of a free-length bar anchored at (0,0), in comparison to a bar position B[0,0,0.707,0.707]. The results illustrate that for all moment matrix sizes above 1×1, a clear minimal is indicated at the position of the reference bar as expected. The Ring contour obtained for $LM_{1\times1}$ can be explained by what the unitary matrix represents. The first term in the matrix is proportional to the area of the bar. Hence, all points which result in a bar of the same length as the reference bar produce a minimal L2E.

$$L2E\left(LM_{fem}, LM_{bar}\right) = \sqrt{\sum_{i=0}^{N-1}\sum_{j=0}^{N-1}\left(LM_{fem_{j,i}} - LM_{bar_{j,i}}\right)^2} \tag{6.10}$$

The results also indicate that by increasing the moment matrix size, the valley leading to the contour's minimal contracts. This is due to the increase in the L2E norm for dissimilar positions, i.e. the L2E value approaches 0 only when the position is much closer to the reference position (as compared to the L2E for the same position for a smaller LM size).

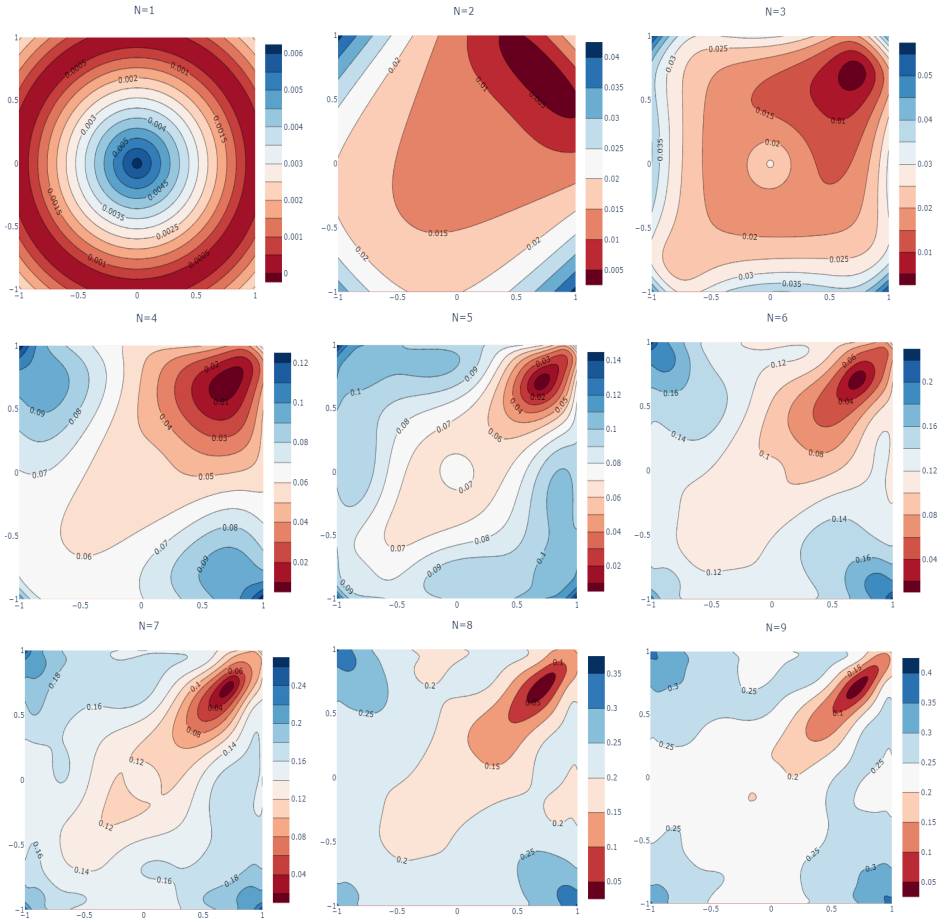

Figure 6.8: L2 norm contour for anchored bar at 0,0 with reference bar B[0,0,0.707,0.707] within domain D[(-1,1),(-1,1)] for moment matrix size N = 1 to 9.

6.3. GLOBAL OBJECTIVE OPTIMIZATION USING BOUNDING BOX CONSTRAINED BARS

The simplest form of the bar match optimization is one in which the bars are allowed to move freely within the image domain. The matching optimization statement is given by 6.11 where n bars are matched within an image domain D[(X_{LL}, X_{UL}),(Y_{LL}, Y_{UL})] with the moment matrix of the TO solution given by LM_{fem}.

$$\begin{aligned} \min_{x_1,y_1,x_2,y_2 \ldots x_{2n},y_{2n}} \quad & L2E\left(LM_{fem}, \sum_{i=1}^{n} LM_{bi}\right) \\ \text{s.t.} \quad & X_{LL} < x_i < X_{UL} \\ & Y_{LL} < y_i < Y_{UL} \\ \text{where,} \quad & LM_{bi_{mn}} = \Lambda_{mn}(x_{2i-1}, y_{2i-1}, x_{2i}, y_{2i}, w) \end{aligned} \tag{6.11}$$

A simple form of this is investigated for a trial case where 4 bars are attempted to be matched to a X shape. The reference bars are Bars B[0.85,0.85,0.15,0.15] , B[0.52,0.48,0.85,0.15] and B[0.48,0.52,0.15,0.85] with widths 0.04. The accurate reference LM is used based on the end points with the bounding domain D[(0,1),(0,1)]. The optimization problem is specified as:

$$\begin{aligned} \min_{x_1,y_1,x_2,y_2 \ldots x_{2n},y_{2n}} \quad & L2E\left(LM_X, \sum_{i=1}^{N} LM_{bi}\right) \\ \text{s.t.} \quad & 0 < x_i < 1, \quad 0 < y_i < 1 \\ \text{where,} \quad & LM_{bi_{mn}} = \Lambda_{mn}(x_{2i-1}, y_{2i-1}, x_{2i}, y_{2i}, w) \\ & N = 4 \\ & LM_{X_{mn}} = \Lambda_{mn}(0.85, 0.85, 0.15, 0.15, 0.04) + \\ & \Lambda_{mn}(0.52, 0.48, 0.85, 0.15, 0.04) + \\ & \Lambda_{mn}(0.48, 0.52, 0.15, 0.85, 0.04) \end{aligned}$$

(a) Xshape optimization problem

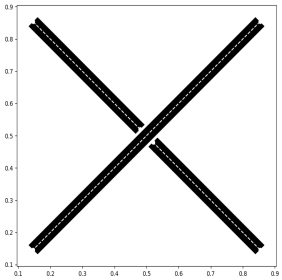

(b) Reference X Image

Figure 6.9: X shape optimization problem

A gradient descent optimizer (scipy-trust-const) [113] is employed for varying sizes of LM to obtain the results in Figure 6.10. The results illustrate the incapability of moment matrices lesser than size 3 to provide a viable optimal. The result clearly illustrates the absence of any definite improvement with an increase in moment matrix size. It is observed that with each additional term either noise or relevancy is added to the objective. But $N_m = 9$ (or 10) illustrates some amount of consistency.

Although the bar positions were identified with the largest moment matrix size, this

is a fairly trivial case. The bar positions are very straightforward and the closed-form expressions were used to obtain the reference moment matrix. For the TO case itself, the moment matrix of the TO result is to be obtained. Therefore unlike an image with uniform identical pixels a general arbitrary quadrilateral mesh needs to be considered. This requires a general form of computation of the Legendre moments for the finite element mesh.

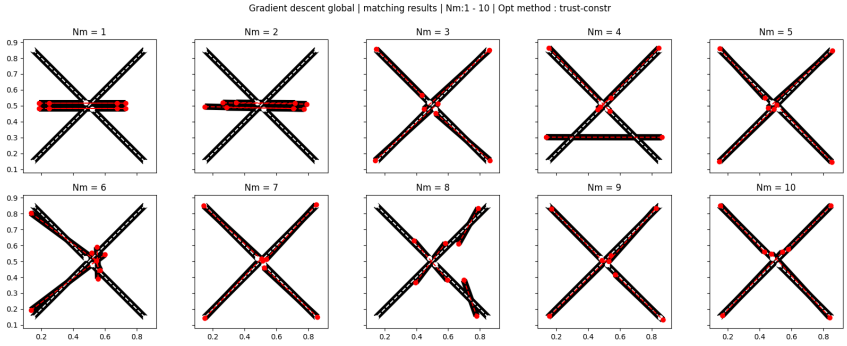

Figure 6.10: Analytical gradient descent optimizer for X shape 4 bars

6.4. TOPOLOGY OPTIMIZATION LEGENDRE MOMENT

The Legendre moments for the TO solutions are computed based on the integral form of the Legendre moment. Limited to quad elements, the Legendre moment for the TO element is computed using the 2D form of the Gaussian quadrature.

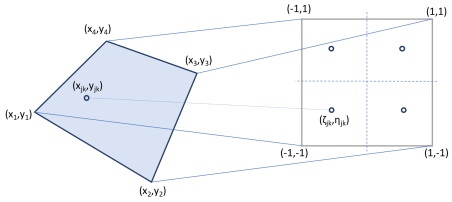

Figure 6.11: Mapping quad-element to the 2D Gaussian quadrature domain.

Table 6.3: Gaussian quadrature coordinates and weights

n	x	w
1	0	2
2	$\pm\frac{1}{\sqrt{3}}$	1
3	$-\sqrt{\frac{3}{5}}, 0, \sqrt{\frac{3}{5}}$	$\frac{5}{9}, \frac{8}{9}, \frac{5}{9}$
4	$\pm\sqrt{\frac{3}{7}-\frac{2}{7}\sqrt{\frac{6}{5}}}, \pm\sqrt{\frac{3}{7}+\frac{2}{7}\sqrt{\frac{6}{5}}}$	$\frac{18+\sqrt{30}}{36}, \frac{18-\sqrt{30}}{36}$

The mapping between the quadrilateral and the 2D Gaussian integration domain is performed using a bi-linear interpolation function given by:

$$
\begin{aligned}
x &= \frac{1}{4}\left((1-\zeta)(1-\eta)x_1 + (1+\zeta)(1-\eta)x_2 + (1+\zeta)(1+\eta)x_3 + (1-\zeta)(1+\eta)x_4\right) \\
y &= \frac{1}{4}\left((1-\zeta)(1-\eta)y_1 + (1+\zeta)(1-\eta)y_2 + (1+\zeta)(1+\eta)y_3 + (1-\zeta)(1+\eta)y_4\right)
\end{aligned}
\tag{6.12}
$$

The 2D Gaussian quadrature of a TO solution is given by a summation over all the elements and is given as:

$$\Lambda_{mn} = \frac{(2m+1)(2n+1)}{4} \sum_{i=1}^{N} \int_{A_{el_i}}^{m} P_m\left(\frac{2x - X_{UL} - X_{LL}}{X_{UL} - X_{LL}}\right) P_n\left(\frac{2y - Y_{UL} - Y_{LL}}{Y_{UL} - Y_{LL}}\right) dxdy \tag{6.13}$$

$$\Lambda_{mn} \approx \frac{(2m+1)(2n+1)}{4} \sum_{i=1}^{N} \sum_{j=1}^{r} \sum_{k=1}^{s} w_j w_k P_m\left(\frac{2x_{jk} - X_{UL} - X_{LL}}{X_{UL} - X_{LL}}\right) P_n\left(\frac{2y_{jk} - Y_{UL} - Y_{LL}}{Y_{UL} - Y_{LL}}\right) \times \left|\det J\left(x_{jk}, y_{jk}\right)\right| \tag{6.14}$$

where the Jacobian for the mapping is given by:

$$\begin{aligned} J(\zeta,\eta) = \frac{\partial(x,y)}{\partial(\zeta,\eta)} &= \begin{bmatrix} \frac{\partial x}{\partial \zeta} & \frac{\partial x}{\partial \eta} \\ \frac{\partial y}{\partial \zeta} & \frac{\partial y}{\partial \eta} \end{bmatrix} \\ = \frac{1}{4} \begin{bmatrix} \left(-(1-\eta)x_1 + (1-\eta)x_2 + (1+\eta)x_3 - (1+\eta)x_4\right) & \left(-(1-\zeta)x_1 - (1+\zeta)x_2 + (1+\zeta)x_3 + (1-\zeta)x_4\right) \\ \left(-(1-\eta)y_1 + (1-\eta)y_2 + (1+\eta)y_3 - (1+\eta)y_4\right) & \left(-(1-\zeta)y_1 - (1+\zeta)y_2 + (1+\zeta)y_3 + (1-\zeta)y_4\right) \end{bmatrix} \\ = \frac{1}{4} \begin{bmatrix} -(1-\eta) & (1-\eta) & (1+\eta) & -(1+\eta) \\ -(1-\zeta) & -(1+\zeta) & (1+\zeta) & (1-\zeta) \end{bmatrix} \begin{bmatrix} x_1 & y_1 \\ x_2 & y_2 \\ x_3 & y_3 \\ x_4 & y_4 \end{bmatrix}^T \end{aligned} \tag{6.15}$$

Utilizing the summation in (6.14), a topology optimization solution is reconstructed using moment matrices of varying sizes. Figure 6.12 illustrates the capability of the methodology in reconstructing a TO solution as well as the possibility to use arbitrary FEM mesh rather than a structured mesh such as a digital image.

Thus, repeating the X shape optimization from Figure 6.9 but with a mesh equivalent of the same bar positions, and calculating the reference moment using the numerical integration scheme, the gradient descent optimization was repeated. The resulting converged solution for varying sizes of reference *LM*, is illustrated in Figure 6.14a . The pixelated reference is an ideal parallel to the eventual TO solution. The gradient descent-based bar matching results in noisy results, frequently resulting in only partial matches. The incapability of lower-order moment matrices is maintained. However, contrary to the previous observations in Figure 6.10 where the matching is improved at specific LM size, the bar match results do not change/ improve at these specific LM sizes. But this could be attributed to a coarse mesh. Hence, Figure 6.14b illustrates the result with a finer mesh for the same pixelated shape. Since the finer elements allow for a larger number of numerical integration points, the resulting reference moment approaches the analytical solution as the elements become finer. But, the finer elements do not assure an accurate match. What can be inferred is that as the number of moments increases each additional moment is not ensured to carry more information i.e improve the objectives

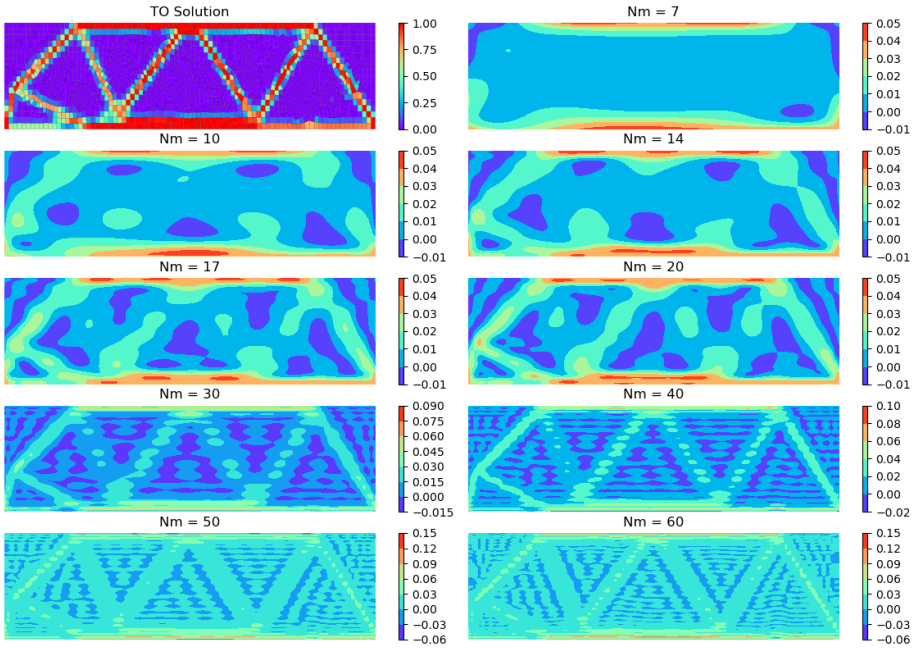

Figure 6.12: Reconstruction of a FEM solution using a generalized LM calculation.

ability to identify the optimal. Studying the magnitudes of the moment matrix itself in Figure 6.13, it can be noted that there are a large number of moments that carry almost no magnitudes. This implies that the choice of adding more terms does not ensure accuracy. This is contrary to the computational mindset, where more number of terms assures more accuracy or a convergent phenomenon can be observed. Hence in the case of a TO solution, the selection of moment matrix order is one to be made carefully. This can be further studied with a TO case study.

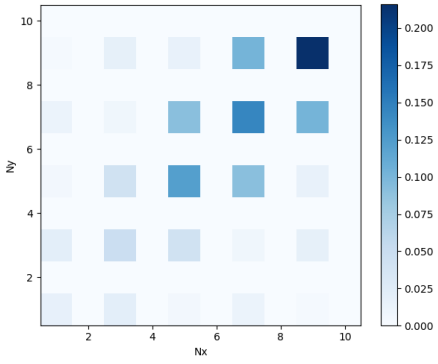

Figure 6.13: X shape LM_{10x10} magnitudes.

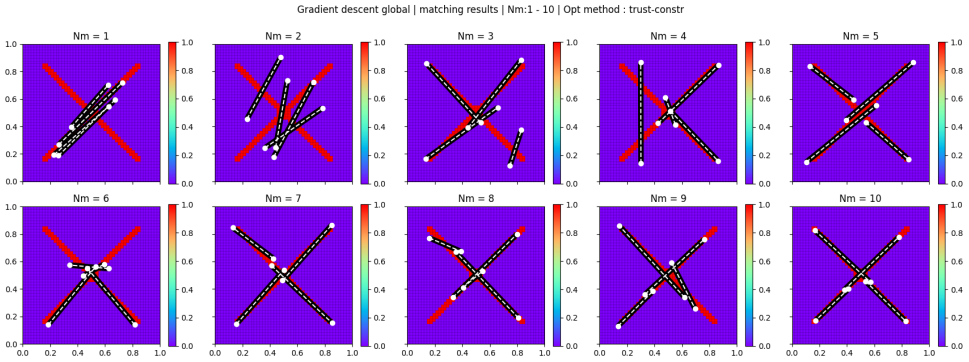

(a) Coarse

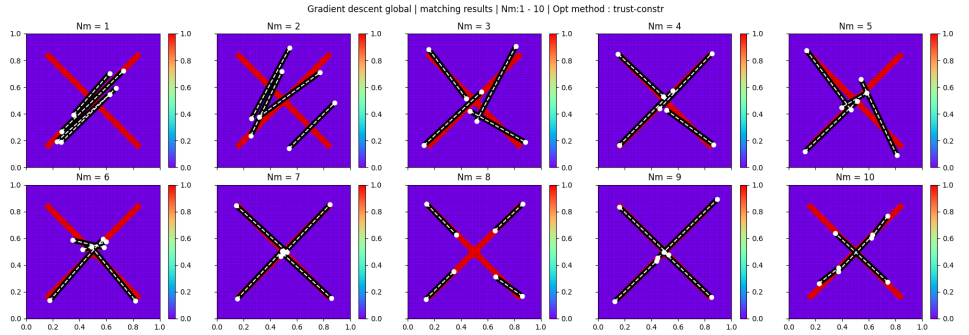

(b) Fine

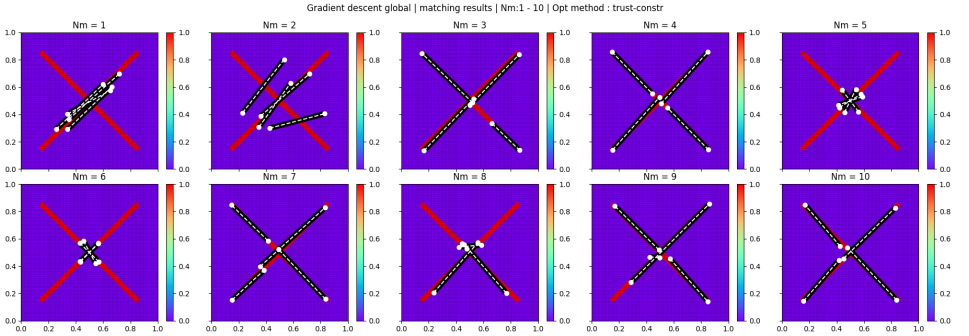

(c) Finer

Figure 6.14: Pixelated X shape bar matching.

GLOBAL BAR MATCHING OF TOPOLOGY OPTIMIZATION SOLUTION

The cantilever beam is an ideal example of typical TO results (see figure 6.15) and shall be used for the preliminary study of the moment matching methodology. Therefore with the same objective formulation as before the new optimization process can be stated as in Statement 6.16. The results of the 2 cases are presented in Figure 6.16. A clear sub-optimal matching is noticed in both cases. It is to be noted here, that the idea of sub optimal matching is a subjective one. Essentially what is desired is a bar position which approximates the underlying TO solution. A sub-optimal match refers to matching where any semblance to an approximation is lacking. From visual inspection, it is observed that the material coverage of none of the bars is as good as it can be. In some cases, the bars approach good positions but do not move further. Thus it can be inferred that the objective is highly nonlinear and non-convex and possesses local stationary points in the solution space. Therefore, it is essential to understand the nature of the objective so as to suitably modify and augment the optimization statement.

$$
\begin{aligned}
\min_{(x_1,y_1,x_2,y_2)\ldots(x_{2n-1},y_{2n-1},x_{2n},y_{2n})} \quad & L2E\left(LM_{FEM_{cantilever}}, \sum_{i=1}^{n} LM_{bi}\right) \\
\text{s.t.} \quad & 0 < x_i < 1 \\
& 0 < y_i < 0.25 \\
\text{where,} \quad & LM_{bi_{mn}} = \Lambda_{mn}(x_{2i-1}, y_{2i-1}, x_{2i}, y_{2i}, 0.025)
\end{aligned}
\tag{6.16}
$$

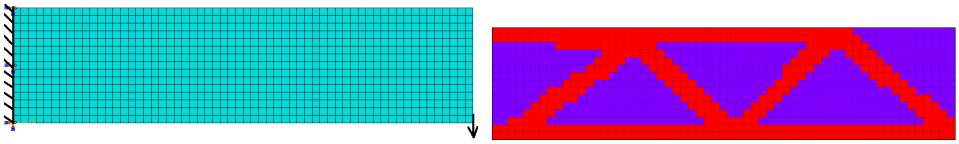

(a) mesh and loading.

(b) TO solution.

Figure 6.15: Cantilever case study

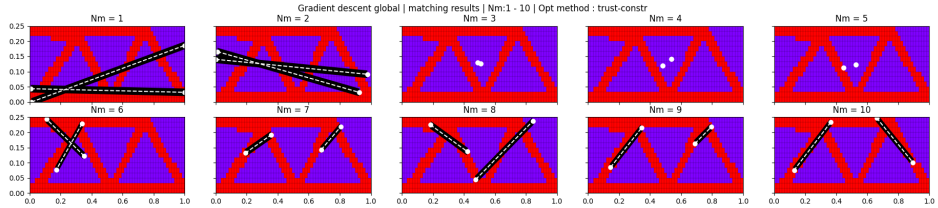

(a) 2 bar match.

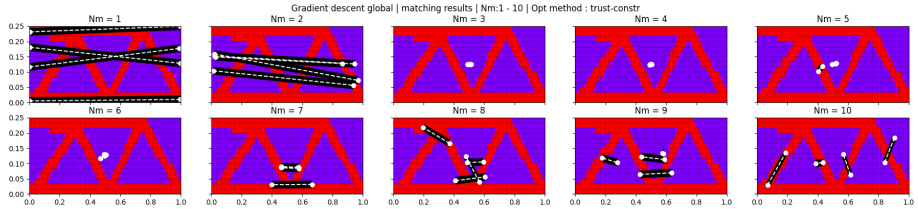

(b) 4 bar match.

Figure 6.16: Global GD match on cantilever beam TO result.

6

6.5. MOMENT MATCHING CONVEXITY STUDY

As observed in Section 6.4, the matching through the *L2E* is not ideal. It is observed that often the bars settle in positions dissimilar to the underlying FEM solution. This leads to a conclusion of an inherent non-convexity and non-linearity existing in the objective chosen. Therefore to investigate these characteristics, this section provides a study conducted to gain an understanding of the objective characteristics. Specifically, the influence of *LM* size, the width, and length of a test bar with respect to a fixed reference bar, and the influence of matching of multiple bars.

6.5.1. INFLUENCE OF MOMENT MATRIX SIZE

A basic understanding of the objective profile is obtained by monitoring the L2E for a bar rotated about a position and compared to a particular angular position and for a bar translated along a direction and compared to a particular position. These are referred to as an angle and translation study respectively. For simplicity, the analytical expressions are used for the reference matrix as well as the test matrix. The results in Figure 6.19 indicate that as the LM size increases, the nonlinearity increases as well, although the global minimal becomes more significant. It can be conclusively stated that the objective characteristics are non-convex for moment matrix sizes above N = 2. Coupled with the fact that relevant moment matching is possible only with LM size above $2x2$, this implies that any moment matching will always be non-convex.

In both the angle and translation study, the local minima and saddle points are observed on either side of the optimal position. In the translation case, the number of local

minimal increases in numbers as the size of the moment matrix increases. This when coupled with the narrowing of the global optimal valley, the ability of the multiple local minimal to settle the descent-based optimizers is inflated.

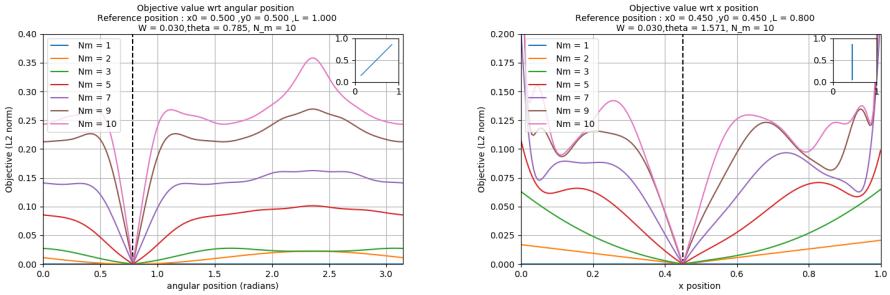

(a) Angle Study

(b) Translation Study

Figure 6.17: Effect of moment matrix size on non-linearity.

6

6.5.2. INFLUENCE OF MATCHING BAR WIDTH

The width study analyzes the scenarios where the width of the matching bar does not match the width of the underlying topology. The generated TO solution does not always contain members of the same size as being matched. Therefore when bar width is chosen for matching, cases where the width can be larger or smaller than the feature width, are not uncommon. Therefore, an understanding of the influence of the moment matrix on the objective of matching varying width bars to a fixed-width reference bar is obtained using an angle and translation study, illustrated in Figure 6.18.

Considering a case where a reference bar of width 0.05 is attempted to be matched with bars with varying widths of 0.025 - 0.1, the use of a larger moment matrix is supported. It is observed that at lower LM sizes, when thinner bars are attempted to be matched to thicker bars, the optimal position obtained is the same as the reference but as the matching thickness increases, the optimal location shifts. In the case of rotation matching the singular optimal location is replaced by twin troughs on either side, leading to an angular offset and in the case of translation, a unidirectional offset is observed in the global optimal. This can be visualized as a slightly angular and translatory offset when thick bars are matched to thin bars. The mismatch also yields multiple local minimal with respect to the angle. At larger LM size, no angular offset is observed when both smaller or larger bars are matched, which can be attributed to the narrower optimal object valley. But, the saddle regions and smaller valleys on either side are still maintained and are in some cases aggravated.

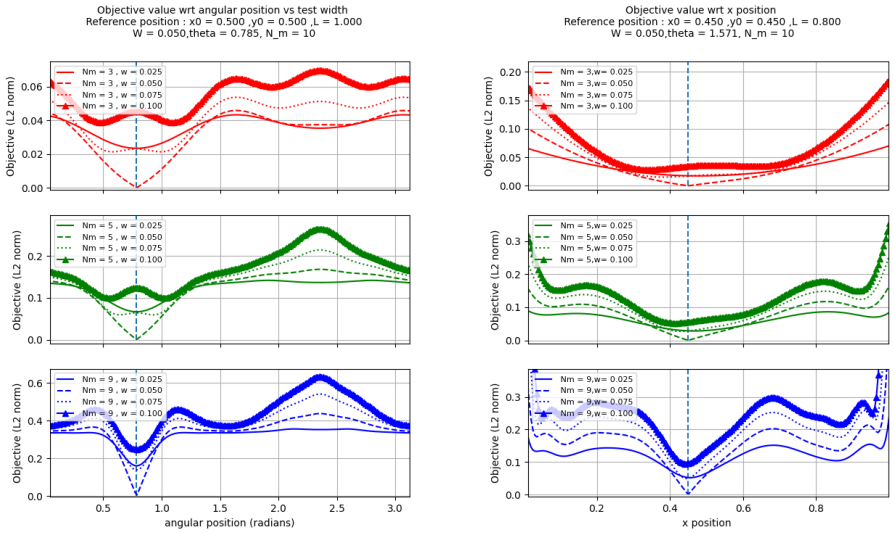

(a) Angle Study

(b) Translation Study

Figure 6.18: Effect of matching width on non-linearity.

6

6.5.3. INFLUENCE OF MATCHING BAR LENGTH

The length study is the most telling of the occurrences of bars settling in local stationary points. It is best to associate the lengths with the search locations of the bars. Consider a gradient descent optimization routine attempting to match a bar of length 0.8m at 45 degrees with $N_m = 5$, which reaches the position of 1.7 radians with a length of 1.1. As illustrated in Figure 6.19c, at this position, any attempt to increase or decrease the length[1] or change the angular position leads to an increase in the objective. Hence, the optimization routine has no option but to settle at the stationary point.

Hence, undoubtedly if the optimizer is allowed to vary both angular positions as well as spatial positions of the bar, the occurrences of many more of such local stationary points increase the probability of sub-optimal matching solutions. Therefore, a case can be made for the use of a smaller N_m, since the increase of N_m yields increase in local valleys. Therefore, using smaller N_m partially reduces the non-linearity in the objective.

[1] A limit exists to the lengths of the bar i.e. a bar can exist only inside the bounding box, therefore the length is limited by what is allowable by the edges of the domain

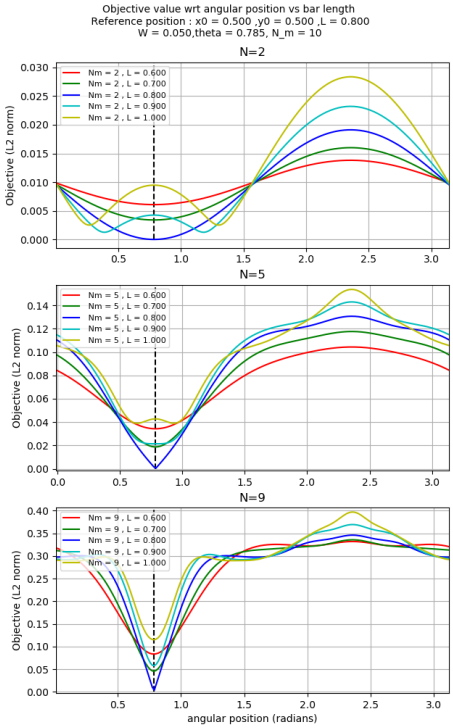

(a) Angle Study

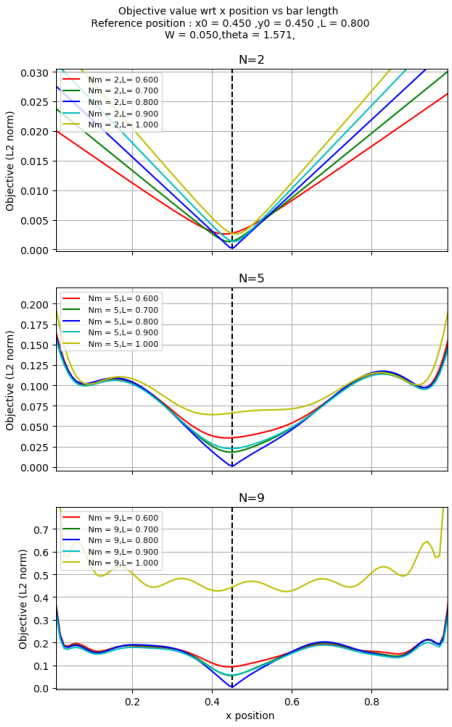

(b) Translation Study

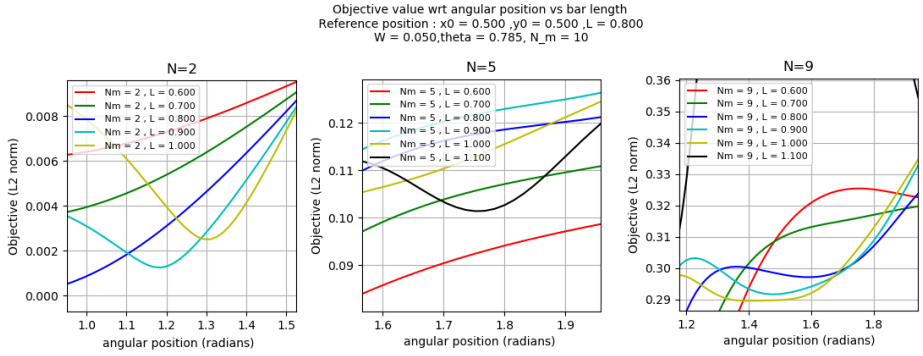

(c) Local stationary points.[a]

[a] A D[(0,0),(1,1)] is used for the L2E study

Figure 6.19: Effect of matching length on non-linearity for N_m=2, 5, and 9.

6

6.5.4. INFLUENCE OF MULTIPLE BARS

Since the global match approach attempts to match multiple bars simultaneously, there can be instances where a bar is attempting to be matched to multiple features in the underlying image. This phenomenon is already observed in the cantilever beam case in Figure 6.16. Although the number of bars is far fewer than necessary it is observed that the bar positions do line up with the underlying material in many instances. This is studied independently with respect to angular and translatory variation through the use of reference matrices with 2 bars of different widths at different angular and translatory positions respectively. The resulting L2E curves are illustrated in Figure 6.20. The curves clearly indicate that in the case of multiple features, the corresponding angle and translation values respectively depict individual local minimal. This implies that the search bar will descend onto the first one it comes across. This is contrary to intuition which would expect that an intermediary position would be generated as an optimal. Therefore, this implies that multiple bars can cause secondary local minimal which further hinder the matching process.

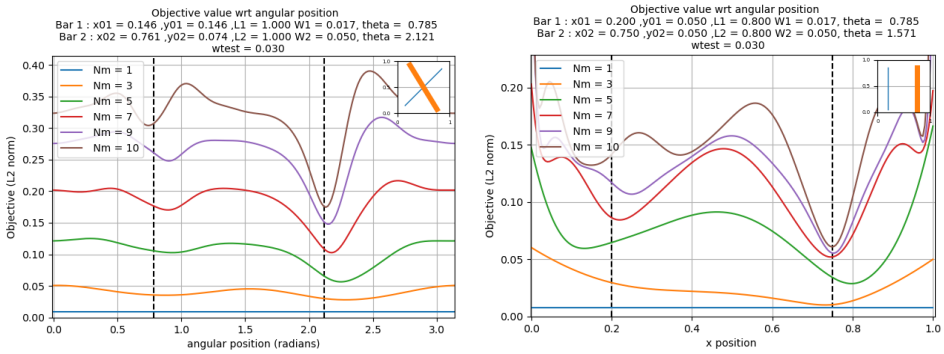

(a) Angular study.

(b) Translation study.

Figure 6.20: Multiple feature - single bar match study

Therefore, in the case of far fewer than required bars being attempted to match, the bars will not only be hindered by the inherent non-linearities in the L2E but will also face the issues of mismatching in width, in length, and the additional local minima. When taking into consideration the large number of possible positions bars can take in a domain, and the nonlinearity of the solution space, it is logical to constrain the solution space in some form.

6.6. FRAGMENT CONSTRAINED OPTIMIZATION

The convexity studies indicate that local stationary points exist in various positions across the solution space. If the solution space were to be divided to allow for matching to occur locally within each space individually and not allow any movement of the bars across spaces, the nonlinearities arising from the interaction of bars belonging to one space with the other design space is reduced.

This can be achieved by allowing bars to operate within localized regions, which shall henceforth be called fragments resulting in a optimization problem in the form represented by (6.17). Hence a modified form of global optimization is investigated where bars are allowed to move within corresponding fragments. Consider the case of the cantilever beam matching with each bar being constrained to a quarter of the domain, the optimization statement is modified to (6.18).

$$\begin{aligned} \min_{x_1,y_1,x_2,y_2\ldots x_{2n},y_{2n}} \quad & L2E\left(LM_{fem}, \sum_{i=1}^{n} LM_{bi}\right) \\ \text{s.t.} \quad & X_{LL_i} < x_{2i-1,2i} < X_{UL_i} \\ & Y_{LL_i} < y_{2i-1,2i} < Y_{UL_i} \\ \text{where,} \quad & LM_{bi_{mn}} = \Lambda_{mn}(x_{2i-1}, y_{2i-1}, x_{2i}, y_{2i}, w) \end{aligned} \tag{6.17}$$

$$\begin{aligned} \min_{x_1,y_1,x_2,y_2\ldots x_{2n},y_{2n}} \quad & L2E\left(LM_{fem}, \sum_{i=1}^{n} LM_{bi}\right) \\ \text{s.t.} \quad & 0 < x_{0,1} < 0.25 \\ & 0.25 < x_{2,3} < 0.5 \\ & 0.5 < x_{4,5} < 0.75 \\ & 0.75 < x_{6,7} < 1 \\ & 0 < y_{0-7} < 0.25 \\ \text{where,} \quad & LM_{bi_{mn}} = \Lambda_{mn}(x_{2i-1}, y_{2i-1}, x_{2i}, y_{2i}, w) \end{aligned} \tag{6.18}$$

Figure 6.22a illustrates the results for the fragment constrained bar match with 4 fragments. It can be observed that the best solutions appear with an LM size larger than $7x7$. This is well explained by the $LM_{cantilever}$ magnitudes in Figure 6.21. The largest contributor is $LM_{7,4}$, therefore only after its inclusion into the L2E do the results improve. But, again any additional LM terms do not retain the same converged position. This implies, that the localization of the bars does not entirely eliminate the possibilities of local minimal. It can also be observed that the use of smaller domains and a larger number of bars does not ensure better results. Figure 6.22b illustrates the cantilever match with $4x4$ fragmentation. Although it is intuitive to assume that allowing a larger number of bars to move around to match the image would provide far improved results, the L2E objective does not prove to be influenced positively by an increase in the num-

ber of bars. This could be attributed to the incapability of bars, moving around within small fragments to cause large-scale improvements in the objective.

The L2E objective is computed with respect to the LM of the TO solution inside the bounding domain and the LM of the bars within smaller domains but still in reference to the Legendre polynomials stretching to the bounding domain. Although the LM function is linear i.e. the moment of the bars altogether is the sum of the individual moments of the bar ($LM_{m,n}(b_1, b_2) = LM_{m,n}(b_1) + LM_{m,n}(b_2)$), as the size of the bars/fragments is reduced, the sensitivities of the design variables (bar endpoint coordinates) constrained to these fragments are insufficient to effectively move all of the bars. This could explain the incapability of the descent optimizer to match the bars in the case of smaller fragments.

Hence, it is advisable to not reduce fragments to sizes much smaller than the domain itself. But, this works against the requirement of complex topologies requiring more straight bars to approximate curved features in the underlying TO solution. Hence a method to satisfy structural resolution, as well as L2E capability, is required. Since the LM can be calculated with respect to any domain size and the number of bars themselves are dependant on the underlying TO solution, the use of smaller reference domains to be matched is a possible middle ground. Thus, a localized matching is preferable rather than global TO domain matching. This allows for bars to be of relative size to the domain itself and simultaneously allows for a larger number of bars to be matched independently.

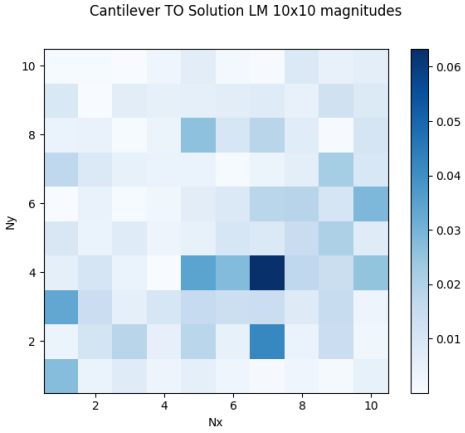

Figure 6.21: Cantilever beam TO solution LM magnitudes.

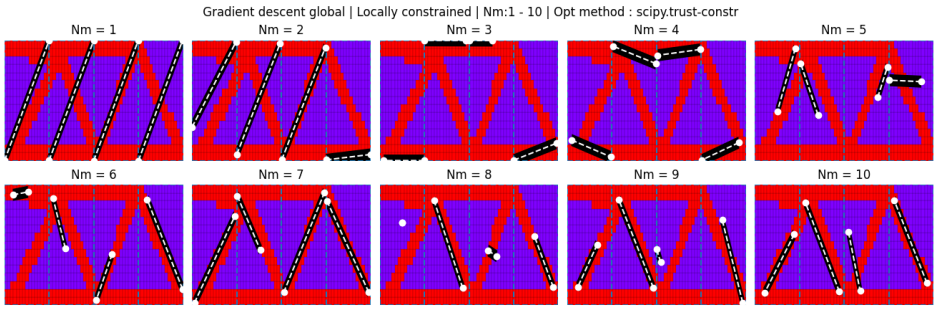

(a) 4x1 match.

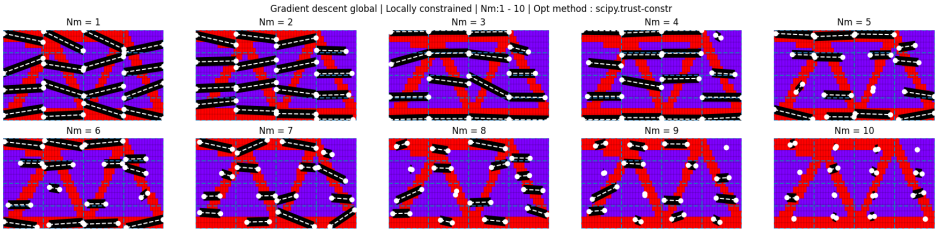

(b) 4x4 match.

Figure 6.22: Fragment constrained cantilever matching

6.7. FRAGMENT-WISE OPTIMIZATION

Studying the reconstruction of bars of varying widths in Figure 6.25, it is observed that an increase in the width results in an increase in the precision of reconstruction for the same N_m. This implies that as the proportion of the bar region in the moment calculation domain increases, the magnitude for the moment values increase as well. This behavior is quite intuitive and is well illustrated for varying bar widths at the same position in Figure 6.23 and Figure 6.24[2]. A clear movement of the relevant moments to higher orders is noticed as the width is reduced. This implies that as the domain sizes increase with respect to the bar size, the relevancy of lower-order moments is lost.

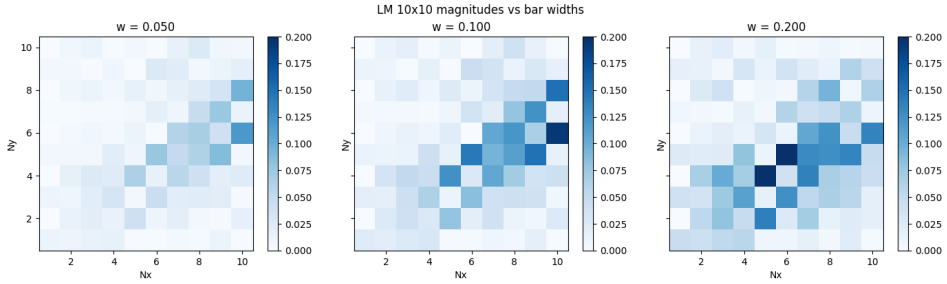

Figure 6.23: LM 10x10 magnitudes with increase in bar width.

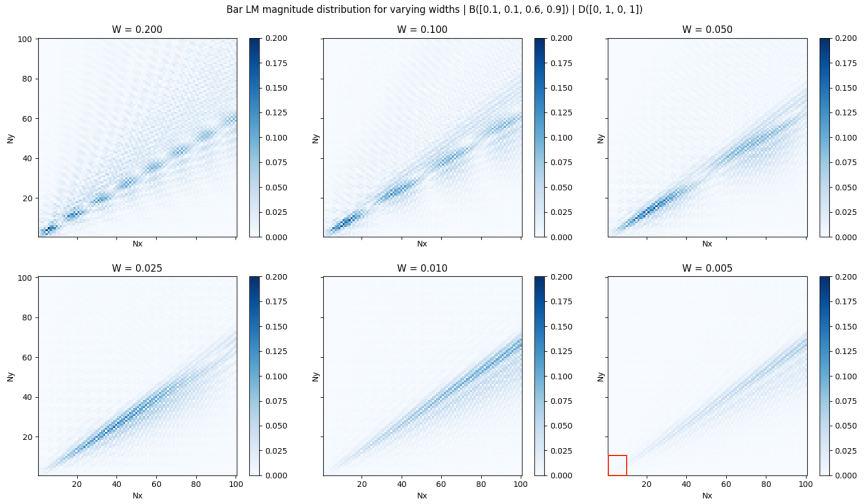

Figure 6.24: Bar Legendre moment (Λ_{mn}) magnitude change for varying widths (moment matrix size : 100x100). B[0.1, 0.1, 0.6, 0.9] in D[0, 1, 0, 1]. (Note : The Red box indicates the bar moments available as closed-form expressions).

[2]The analytical expression for the bar moments are available only up to 10x10, in this case, the comparatively expensive numerical integration was used to obtain $LM_{100x100}$.

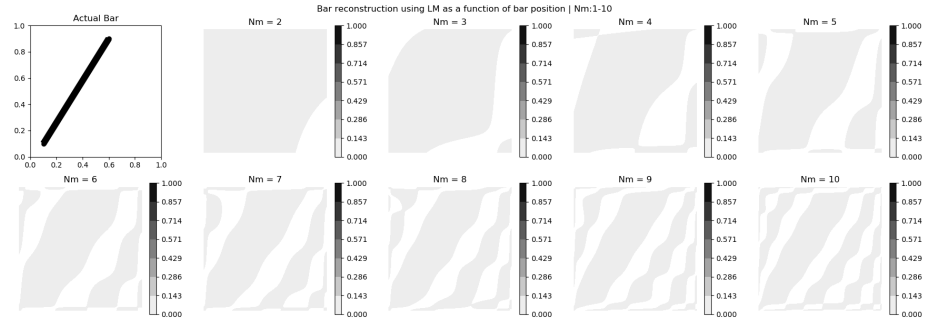

(a) Bar width = 0.05

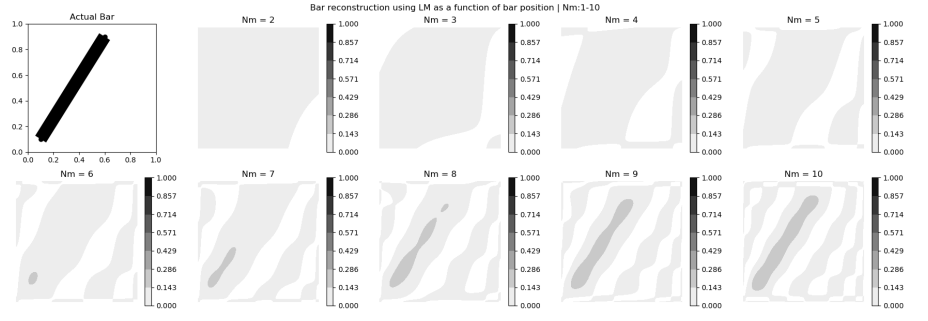

(b) Bar width = 0.1

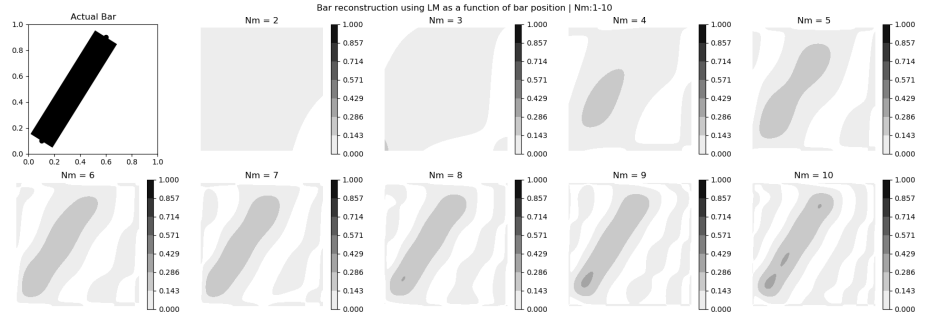

(c) Bar width = 0.20

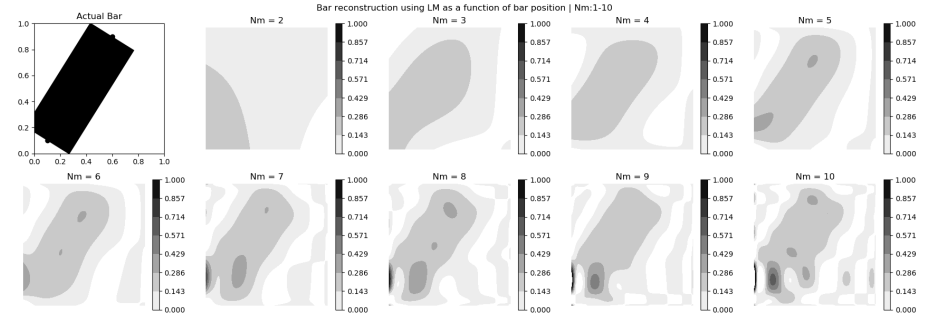

(d) Bar width = 0.40

Figure 6.25: Bar reconstruction of varying widths using varying size *LM*

Hence, to enhance the efficacy of matching as well as to simplify the optimization routine, it is best to perform the moment matching with fragment sizes that are compatible with the width of the matching bars. Consider the cantilever beam with 4×1 fragment-wise matching in Figure 6.27b. The fragment match is noticeably improved by reducing the scope to specific fragments. This can be attributed to the larger amount of relevant moments present within the $LM_{10\times10}$. But, at the same time, the smaller fragment sizes have also illustrated the noise introduction by additional terms. Consider the 4×1 case itself, post LM size of 5×5, the additional terms have not added any relevancy to improve positioning, instead, the positions have been diminished. This implies that post a minimum number of terms, additional terms can be detrimental to the matching. An argument could be made to use the largest terms within the corresponding LM to identify positions. However, it must be noted that relevancy (magnitudes) of moments and descriptive capabilities are not complementary. This will be revisited in Section 6.9 with a magnitude weighted norm.

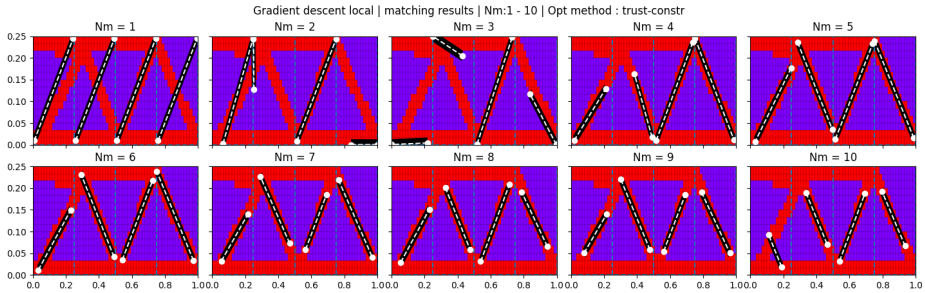

(a) Match

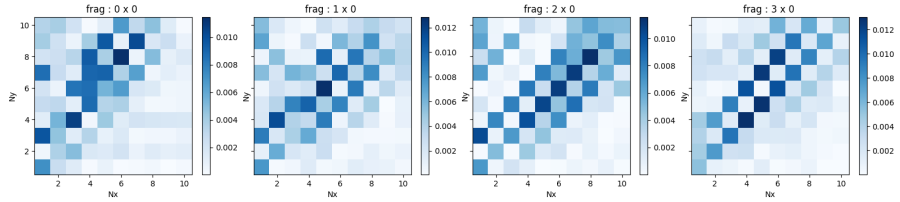

(b) Fragment moment magnitudes

Figure 6.26: Cantilever 4×1 fragment-wise matching.

As the width approaches the fragment size itself, the magnitudes of the relevant moments approach the amplitudes of the non-significant moments. Hence, the descriptive ability of the moments is lost. This is well noticed in the comparison of the cantilever fragment-wise matching with 4×1 and 8×4 fragmentation. The latter has a large number of bars disappearing due to the fact that the corresponding LM of the fragments comprises lower amplitudes. Hence, any difference in the moments computed within

the L2E is not significant enough to identify positions, rather the bars themselves vanish. This effect is magnified at larger LM sizes. Up to $LM_{3\times3}$, the matching within the smaller fragments can actually be deemed reasonable. But in many cases, due to the inherent non-linearity of the objective itself, the vanishing of bars, as well as mismatches, are still possible. Therefore, although fragmentation allows for better-localized matching, it does not completely eliminate mismatches.

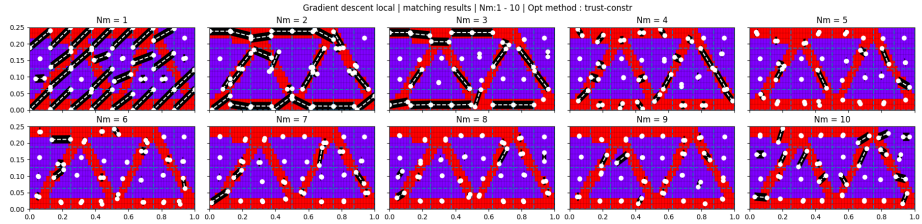

(a) Match

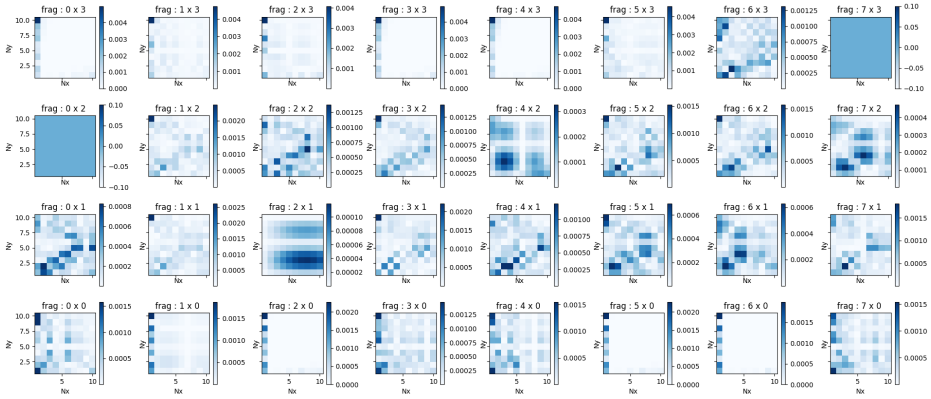

(b) Fragment moment magnitudes

Figure 6.27: Cantilever 8 × 4 fragment-wise matching.

To summarize, fragment-wise matching is more capable when compared to the former method of global matching. The smaller fragments allow for more relevant moments to be captured at lower moments and as the fragment sizes reduce, the importance of larger order moments decays. With smaller fragment sizes, the lower order moments are capable of identifying bar positions. A *LM* size of 3 appears to be ideal for application. But, the presence of localized minimal still inhibits matching. Therefore, to further improve accuracy, a reduction of the solution space is necessary.

6.8. BOUNDARY SEARCH

Unlike images where floating regions can exist, TO is limited (in preferable cases) to structures that are capable of carrying loads, and hence, no floating members and hanging members must exist unless the latter is carrying a load or is a boundary condition. Hence it is analytical to predict that a member in one fragment must connect to a member in a neighboring fragment. Hence the endpoints must lie along the fragment boundary. Therefore, taking advantage of the properties of the underlying TO solution, an additional constraint can be added to the moment matching optimizer. Given by Statement 6.19, the solution space is limited to bar endpoints lying only along the fragment boundary.

$$\begin{aligned} \min_{x_1,y_1,x_2,y_2 \ldots x_{2n},y_{2n}} \quad & L2E\left(LM_{fem}, \sum_{i=1}^{n} LM_{bi}\right) \\ \text{s.t.} \quad & X_{LL_i} < x_{2i-1,2i} < X_{UL_i} \\ & Y_{LL_i} < y_{2i-1,2i} < Y_{UL_i} \\ & (x_i - X_{LL_i})(x_i - XUL_i)(y_i - Y_{LL_i})(y_i - YUL_i) = 0 \\ \text{where,} \quad & LM_{bi_{mn}} = \Lambda_{mn}(x_{2i-1}, y_{2i-1}, x_{2i}, y_{2i}, w) \end{aligned} \tag{6.19}$$

However, in this form the constraint is non-differentiable at the corners. Therefore, a straightforward gradient descent optimizer cannot be employed. Nevertheless, constraining the optimization to the boundary, the search domain has been drastically reduced, hence any use of an optimizer can be replaced with an explicit search of the domain. Hence, with a limited set of points on the boundary, a brute-force analysis conducted to obtain the most suitable bar within the set is a good alternative to the former gradient descent algorithm. This partially alleviates the mismatches due to the non-linearities in the objective.

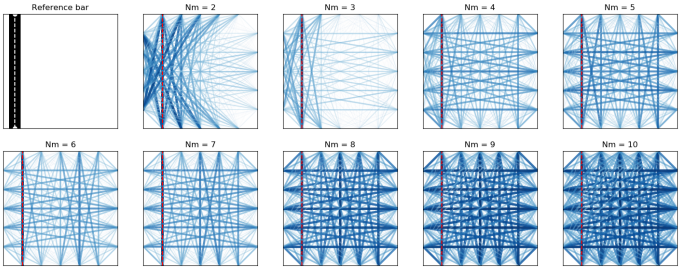

(a) Boundary constrained brute force match for single bar.

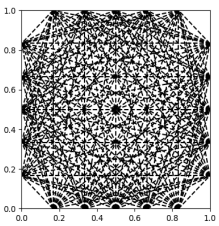

(b) Brute force search bars for 5 points on each side (set size:150)

Figure 6.28: Boundary constrained matching

Figure 6.28a illustrates the brute-force analysis conducted for varying N_m. The opacity and thickness indicating how close the L2E for the bar is to the search set minimal L2E(dashed red). It is observed that in this case, the closest position is identifiable for all N_m. The figure is also indicative of why any boundary-constrained optimizer

would fail if reliant on gradient descent methods since local stationary points exist along the boundary as well. Figure 6.29 depicts the boundary search employed for variable fragment sizes of the cantilever TO solution.

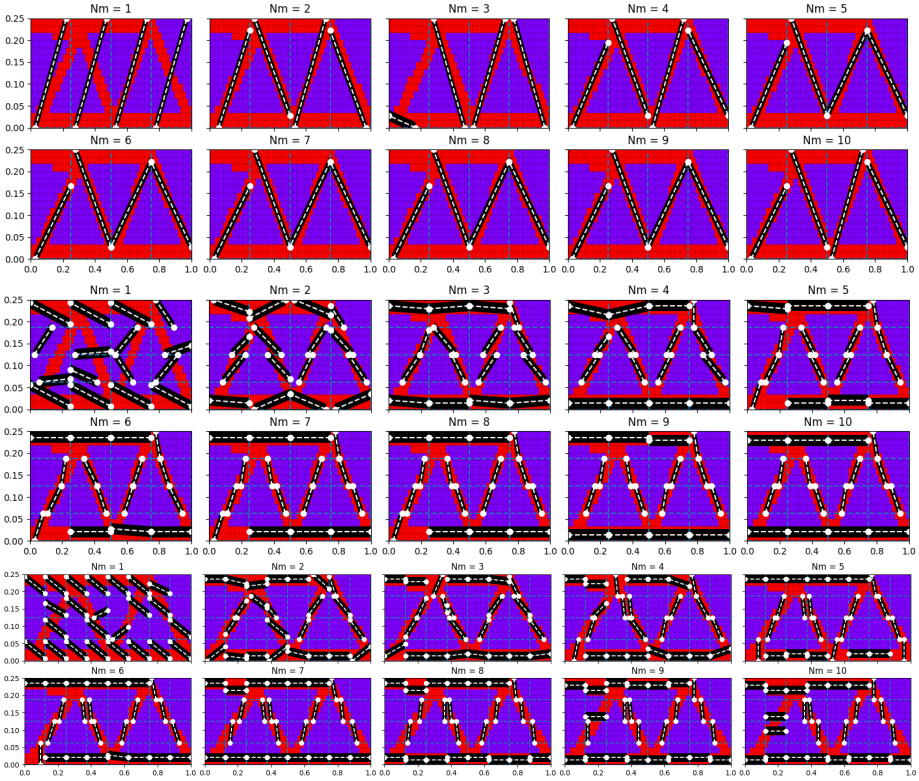

Figure 6.29: TO cantilever beam bar matching using fragment-wise boundary search.

6.8.1. ALIASING

Similar to its namesake in signal processing, if far fewer points than required are used to estimate the position of the bar, an erroneous result is possible. This is illustrated in Figure 6.30. As the number of search points increases, the aliasing reduces to a discernible extent. Figure 6.31 depicts a similar mismatch in the case of a TO result. To counteract the increased number of search points it is best to limit the size of the LM. This is also aided by the fact that in smaller fragment sizes, the lower order elements carry most of the information, hence any additional terms add more noise than information. This is reflected in the quality of the matches at larger LM. Even with larger sampling, the quality of results either is inferior or does not improve. Therefore, it is best advised to use a combination of larger sampling with lower-order LM by limiting to $N_m = 5$.

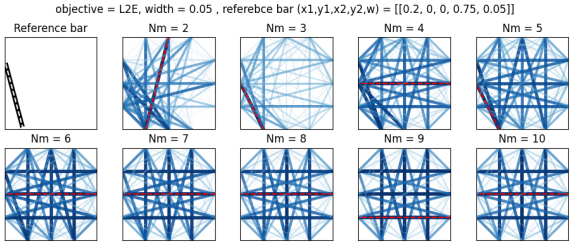

(a) Aliasing in boundary bounded optimization with 3x3 points.

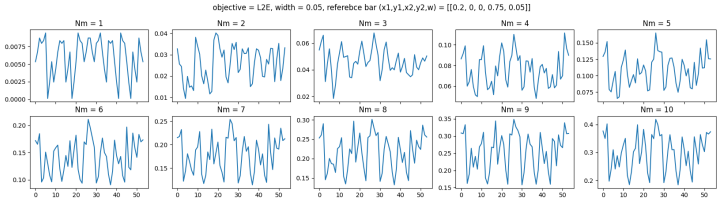

(b) Objective 3x3 points.

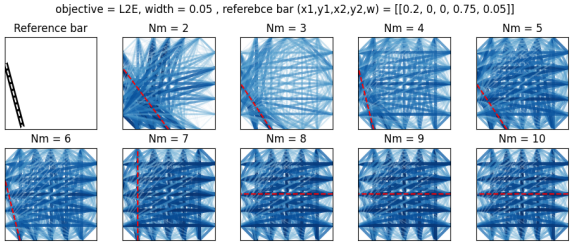

(c) Aliasing in boundary bounded optimization with 5x5 points.

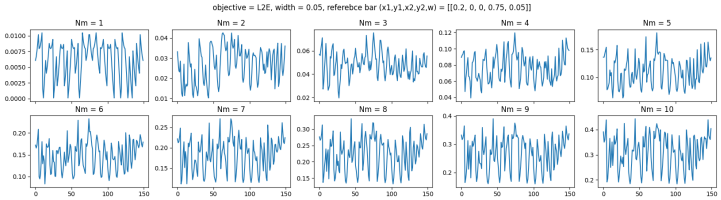

(d) Objective 5x5 points.

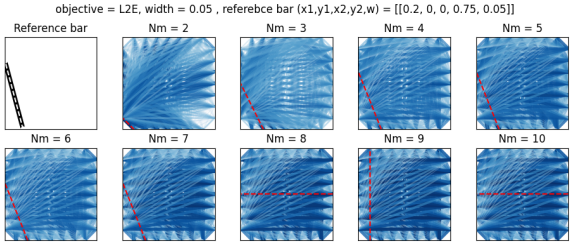

(e) Aliasing in boundary bounded optimization with 7x7 points.

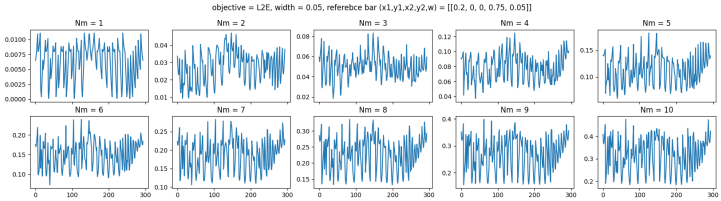

(f) Objective 7x7 points.

Figure 6.30: Aliasing illustration

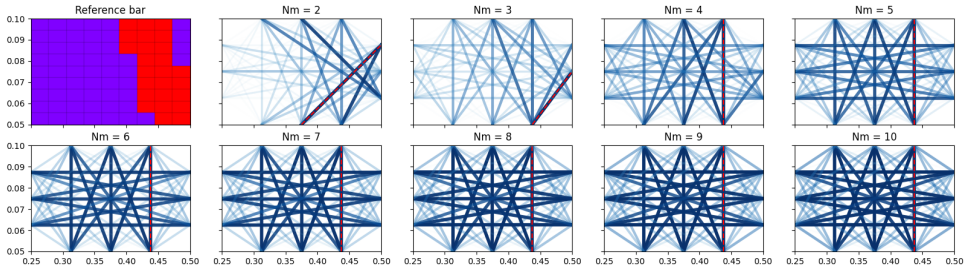

(a) 3x3

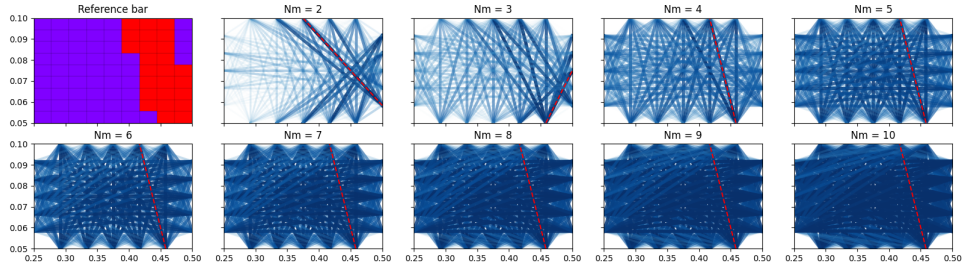

(b) 5x5

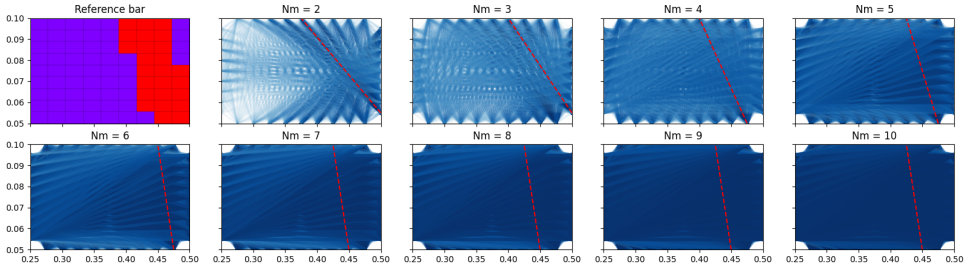

(c) 9x9

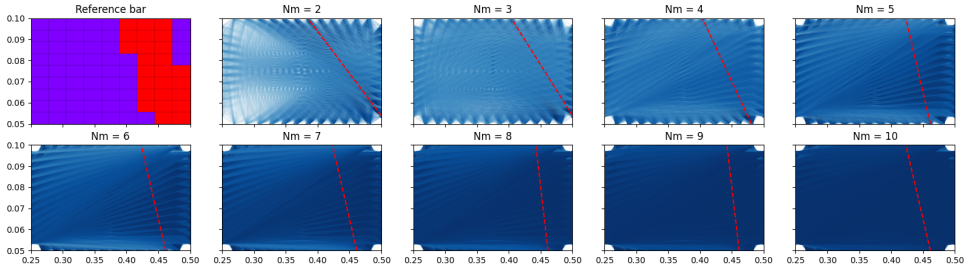

(d) 12x12

Figure 6.31: Aliasing in a TO match

MATERIAL LEAKAGE

Although boundary bounded search reduces the search domain significantly, an inaccuracy is introduced in the moment calculation due to a portion of the bars falling outside the domain. This is illustrated in Figure 6.32a. It is also observable in Figure 6.25, where the bar is reconstructed with moment values with a portion of it falling outside the domain. Close to the locations of the bar leakage, local high amplitudes are observed. This is due to the orthogonal properties of the Legendre polynomials terminating after the boundary and to reconstruct an image only information within the image domains is to be considered. Hence, as the portion of the bar lying outside the domain increases, the noise increases accordingly.

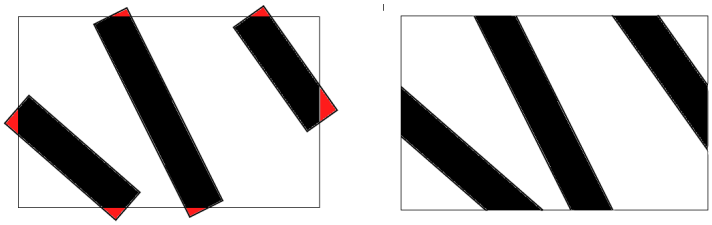

(a) Material leakage in boundary bounded bars (b) Equivalent quad region with no leakage

Figure 6.32: Leakage illustration

Thus, since the derived analytical moment equations of the bars are computed over the entire area of the bar, the expressions can lead to inaccuracies in the boundary bounded case. Hence, as an alternative, it is possible to use the discrete integration technique employed for the FEM elements as described in Section 6.4. The latter reduces the included noise in the matching and hence, the distinctness of the optimal is increased to a notable extent. This is apparent on examining Figure 6.30 and Figure 6.33. The number of minimal spikes which are in the range of magnitude of the global minimum is significantly reduced.

It could be argued that if the latter is superior why it was not the preferred choice. However, the former is computationally far more efficient as tabulated in Table 6.4. The use of discrete integration requires an increasing number of function calculations as the order of the moment increases. In comparison, the compounding length of the analytical expression for the moments as order is increased is still much quicker to execute, therefore when a smaller number of fragments are present, the quadrilateral form can prove to be more useful, but when the number of fragments increases, the bar form with an increased number of sampling points can be preferred.

N_m	Numerical	Analytical
3	7.6 ms	0.07 ms
4	14.5ms	0.096 ms
5	21.6 ms	1.8 ms
6	32.4 ms	2.6 ms

Table 6.4: Execution time for *LM* computation of Numerical-quad vs Analytical-bar formulation.

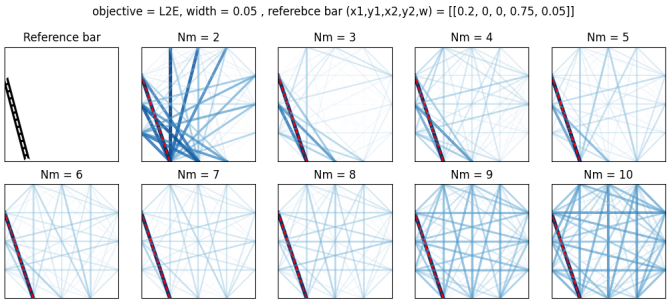

(a) No leakage boundary-bounded matching with 3x3 points.

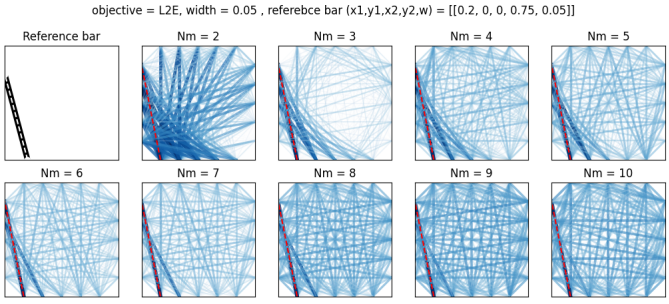

(b) No leakage boundary-bounded matching with 5x5 points.

Figure 6.33: No leakage matching.

6.9. ALTERNATIVE OBJECTIVE FORMULATIONS

Of the various other objectives which were investigated during the course of the project, two candidates which could be a suitable alternative to L2E are described below. These objectives if further developed could prove superior to the L2E.

COSINE SIMILARITY

Commonly used in large-scale data analysis, the cosine is a measure of similarity between large data sets. The cosine can be visualized by its origin in 2D/3D by the angle between 2 unit vectors. A value of 1 implies that there is a 0-degree angle between the vectors which implies maximum similarity(identical) and a value of -1 implies that there is a 180-degree angle between the vectors, which implies absolute dissimilarity. The cosine for a multi-dimensional data array is given by (6.20).

$$\cos(\theta) = \frac{\mathbf{A}\cdot\mathbf{B}}{\|\mathbf{A}\|\|\mathbf{B}\|} = \frac{\sum_{i=1}^{n} A_i B_i}{\sqrt{\sum_{i=1}^{n} A_i^2}\sqrt{\sum_{i=1}^{n} B_i^2}} \tag{6.20}$$

The key distinction from L2E objective is the cosine similarity is a maximization formulation. Otherwise, from the angle and translation study using the cosine formulation it can be seen that the non-convexity and non-linearity is still retained. However one superiority is visible in the Figure 6.35, where irrespective of mismatching the width of the matching bar and the reference bar, the objective characteristics are entirely identical. This allows the cos formulation to be a capable candidate in matching cases where the mesh is very coarse or single-pixel width cases. However, from a broader perspective this could also lead to erroneous results in the case of TO solutions without well defined features with stray strings of elements with $\rho = 1$.

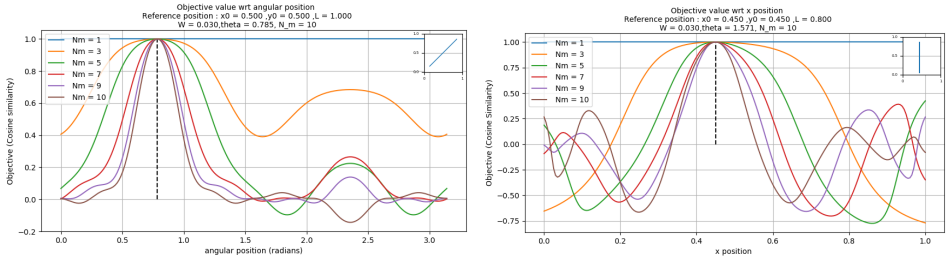

(a) Angle study

(b) x study

Figure 6.34: Cosine similarity angle and x position study for varying N_m.

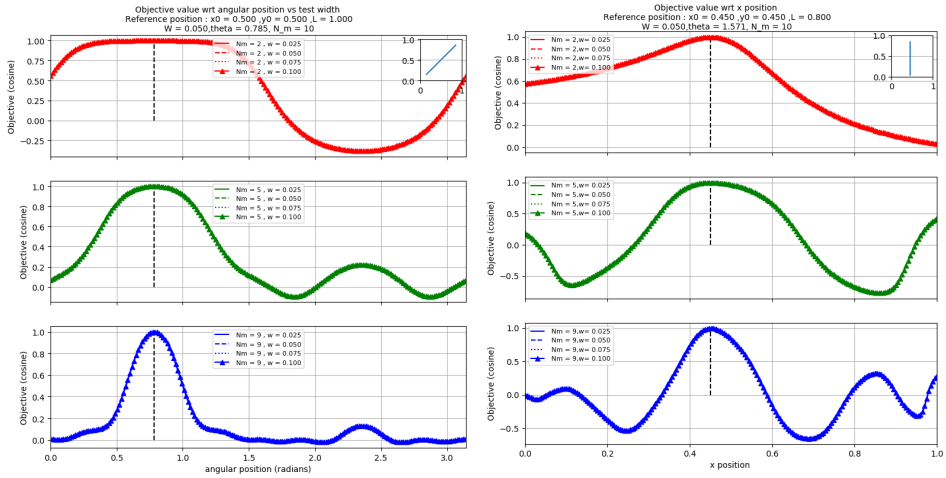

(a) Angle study

(b) x study

Figure 6.35: Cosine similarity angle and translation study for varying width reference bars.

6

MAGNITUDE WEIGHTED NORM

Section 6.3 and Section 6.4 illustrated the relatively unequal contribution of moments in a moment matrix. Thus it can be argued that the contributions for similarity measurement must be proportional to their magnitudes. Naturally, a weighted norm is a possible implementation of this principle. The weighted norm is given by Equation 6.21 and its application in multi-bar matching is illustrated in Figure 6.36. The modified objective is capable of enhancing convexity in smaller LM but is not significantly superior to its unweighted counterpart.

$$L2E\left(L_{fem}, L_{bar}\right) = \sqrt{\sum_{i=0}^{N-1}\sum_{j=0}^{N-1}\left(L_{fem_{j,i}} - L_{bar_{j,i}}\right)^2 \times w_{i,j}}$$
$$\text{where,} \quad w = abs\left(\frac{L_{fem} - \min(L_{fem})}{\max(L_{fem}) - \min(L_{fem})}\right)^p \tag{6.21}$$

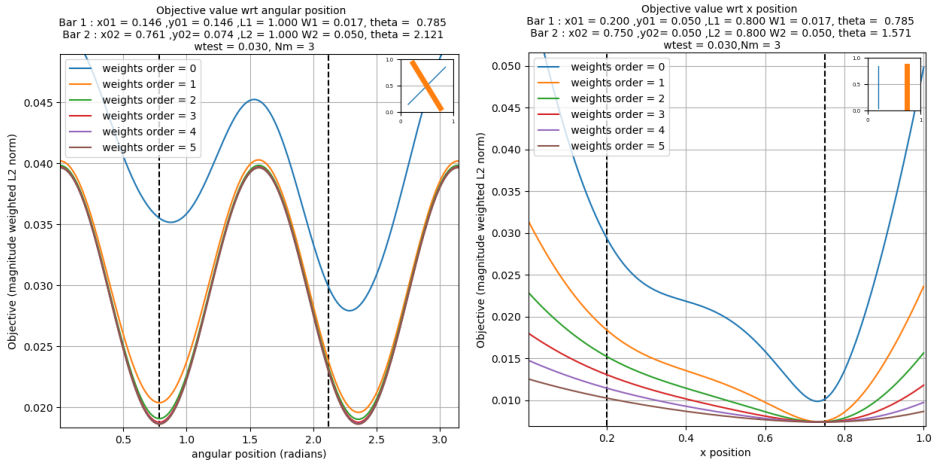

(a) $N_m = 3$

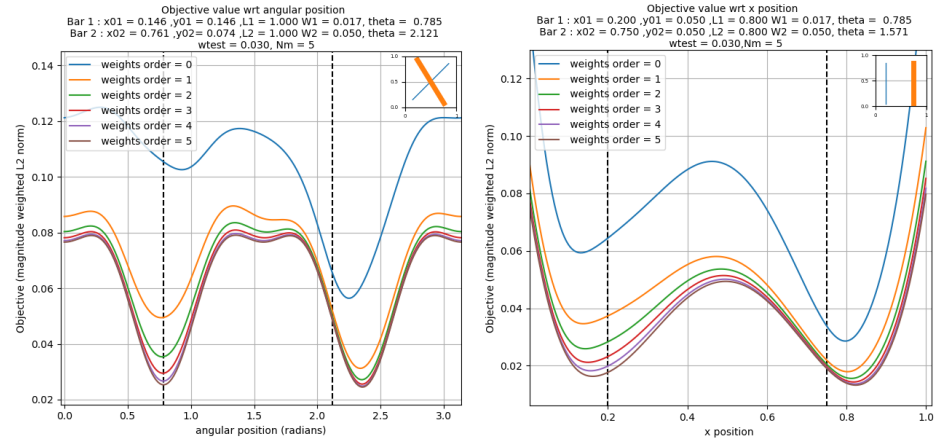

(b) $N_m = 5$

Figure 6.36: Magnitude weighted L2 Norm

6.10. SUMMARY

This chapter investigates the image processing based matching of a TO solution to a set of bars based on the initially posed hypothesis,

"Given the Legendre moments of a TO solution, and the Legendre moments of a bar as a function of its coordinates, orientation, and dimensions, by matching the corresponding moments, the equivalent/approximate positions of the bars can be identified."

Using the L2E as an objective to measure the similarity between the moments of the TO solution and the bars, a clear global minimal is observed where the position of the bar and the TO solution match. Therefore, the initially posed hypothesis can be deemed as one of merit. However, the employment of a gradient descent optimizer does not yield a suitable identification of the bar positions due to the nature of the L2E. This is because L2E does not distinguish between a certain magnitude of difference in $LM_{a,b}$ and $LM_{c,d}$ due to their identical contribution to the L2E, but their influence on the underlying positions of the bar itself is significant. Additionally, the interaction of multiple bars within an open domain, leads to large number of local stationary points. Hence, the design domain is constrained to limited regions called fragments to reduce the design space and simplify the matching to a single bar in each fragment. Using an explicit search strategy, approximate bar positions can be swiftly identified from a limited set of possible positions based on the L2E. Table 6.5 tabulates the essential recommendations for bar matching through the L2E based on the proposed fragment-wise bar match (FWBM) methodology. However, the fragmenting is required to be further enhanced to eliminate redundant locations and accommodate simpler topologies within larger fragments. Additionally, the matched bars require further processing to be converted into a load capable structures. Therefore, a more advanced fragmenting strategy, as well as post-processing strategies, will be investigated in the subsequent chapter.

Fragment dimension : bar width	1.5 - 2.5
Recommended LM size	$LM_{3\times3}$ to $LM_{5\times5}$
no. of integration points within an element for Legendre polynomial $L_p(x)L_q(y)$	$(p+1)(q+1)$
no. of sampling points per edge for boundary search	5 - 9
TO. density threshold	0.15

Table 6.5: Recommended parameters for LM based bar matching.

7

FRAGMENTATION AND POST-PROCESSING

This chapter describes the fragmentation and post-processing strategies proposed to generate suitable solutions from the fragment-match process described in Chapter 6. Section 7.1 describes the developed fragmentation strategies followed by Section 7.2 describing the set of post-processing operations proposed to generate an interconnected structure from the results of the bar matching. Section 7.3 showcases the cumulative capabilities in generating desirable structures by employing the framework on case studies from literature as well as panels from the optimized G5 galley.

As recognized in Chapter 6, the most suitable method for the moment-based bar matching algorithm is for it to be implemented locally and using solitary bars. Hence in this section, a localized matching algorithm is proposed based on the boundary constrained search strategy, an attempt is made to convert results from topology optimization to skeletal structures with bars of the same widths. The question arises, how the said regions can be identified where the bars will be matched. Two such methods are proposed, a uniform fragmentation approach and an adaptive fragmentation approach.

7.1. UNIFORM AND ADAPTIVE FRAGMENTATION

The most straightforward method to fragment an image is along the Cartesian axes. This is the most intuitive method of dividing any domain and is very straightforward in its implementation. But, the ideal size of the fragment itself is not uniform throughout the domain. Since the fragment size is to remain uniform and simultaneously provide globally ideal results, this requires a fragmentation study to be conducted where the sizes of the fragments are changed sequentially. Figure 7.17 illustrates this mismatch of fragment size preference across the domain. Thus, in the scope of streamlining the matching process, the uniform fragmentation method is not preferable.

Due to the complex topologies that can be generated in TO, the uniform fragmentation strategy is a very blunt tool to identify suitable fragment sizes. It is preferable to identify the fragments such that they satisfy requirements locally without largely varying neighboring fragment sizes. To this extent, a Quad tree-based adaptive fragmentation (AF) strategy is developed. Typically Quadtree based methods identify, meshing capabilities based on data present, but in the case of a matching operation, the goal is to match only where possible and to fragment only when the resulting children are suitable as well.

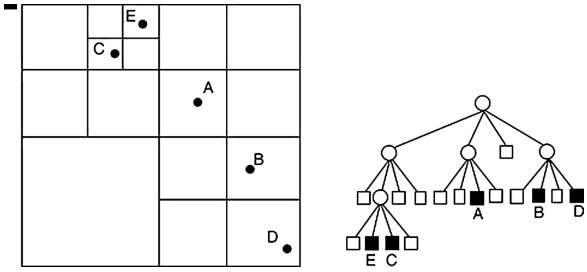

Figure 7.1: Regular Quad-Tree based fragmentation.Borrowed from [111]

Typically quadtree-based meshing utilizes a rooted tree with each node comprising of 4 children where each child represents a quadrant of the parent node/fragment. Generally, the fragmentation in each generation is decided based on the information from the current generation. This can be information such as the number of points in the fragment and size of the fragments etc. But in the scope of fragmentation for bar match-

ing, empty fragments are of no interest and any almost fully filled fragment cannot be suitably matched. Therefore a check is required to ensure that the fragmentation of a parent yields suitable children. Therefore two forward evaluation-based fragmentation methodologies are developed.

7.1.1. VOLUME FRACTION LIMITED FRAGMENTATION

Since fragments possessing excess or minimal material are not relevant for matching. The first AF strategy proposed evaluates the volume fractions of the possible children fragments and conducts fragmentation only if the resulting fragments possess material within the stipulated volume fractions. However, if an empty fragment is observed, the fragmentation is performed but no further fragmentation is allowed on the empty fragment. This is in an effort to discard any redundant regions. It is to be noted that, unlike the regular quadtree, fragments are not quartered in one step. To provide the best chance for fragmentation, the fragmentation is performed in two steps in the decreasing order of the dimensions. If the primary direction fragmenting is deemed suitable then, the secondary fragmentation checks 2 intermediate fragments individually for their fragmentation capability in the second direction. Therefore increasing the capability of fragmentation by yielding either 1, 2, or 4 children fragments instead of the normally 1 or 4 fragments. Therefore, the tree for a fragment P, when the direction of division is first X and then Y is given by:

- P if $vf_{x1}, vf_{x2} \in (0, vf_{min})$ or $vf_{x1}, vf_{x2} \in (vf_{max}, 1]$. Followed by:
  - P if $vf_{y1}, vf_{y2} \in (0, vf_{min})$ or $vf_{y1}, vf_{y2} \in (vf_{max}, 1]$.
  - a tree with children the trees for $P_{y1} and P_{y2}$.
- A tree with as children the trees for P_{x1}, P_{x2}. With the tree of P_{xi} being
  - P_{xi} if $vf_{xi_{y1}}, vf_{xi_{y2}} \in (0, vf_{min})$ or $vf_{xi_{y1}}, vf_{xi_{y2}} \in (vf_{max}, 1]$.
  - A tree with as children the trees for $P_{xi_{y1}}$ and $P_{xi_{y2}}$.

Additionally, the fragmentation is performed in a direction only if the dimension of the generated fragments are larger than a stipulated amount (In this case more than 1.25 times the bar width). This is to prevent cases where the fragment sizes become very comparable to the bar width to be matched and to provide a limit to the number of generations in the fragmentation-tree. A flowchart is presented in Figure 7.4 to better understand the adaptive fragmentation strategy proposed. Figure 7.2 illustrates the volume fraction based adaptive fragmentation of the cantilever TO solution.

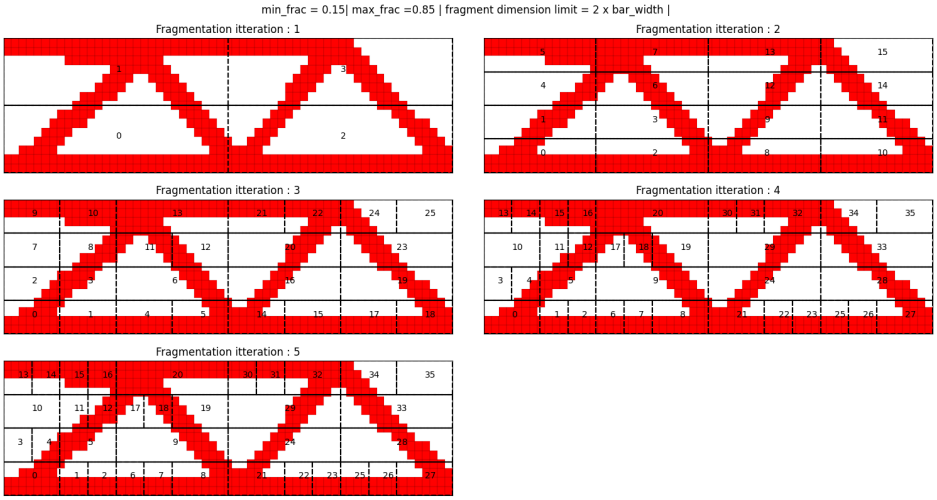

Figure 7.2: Volume fraction limited adaptive fragmentation

7.1.2. REDUNDANT AREA ISOLATION

Although the volume fraction-based fragmentation is capable of preventing cases where the volume fraction falls below the stipulated amount, it is analytical to assume that within a fragment that possesses a small amount of material, there can exist a child fragment that can contain material larger than the minimal area fraction. Therefore a purely maximal area fraction-based AF is proposed where isolation of fragments is performed if children fragment volume fractions violate the maximum volume fraction stipulation, if the said fragment is empty or if the fragment size becomes comparable to the bar width to be matched. Therefore, this method can be considered a variant of the volume fraction limited fragmentation where $vf_{min} = 0$. Figure 7.3 illustrates the redundant area isolation based adaptive fragmentation of the cantilever TO solution. A clear difference is noticed between Figures 7.2 and 7.3, where the latter isolates empty regions and attempts to include more of the underlying topologies within smaller fragments, leading to a larger fragment count.

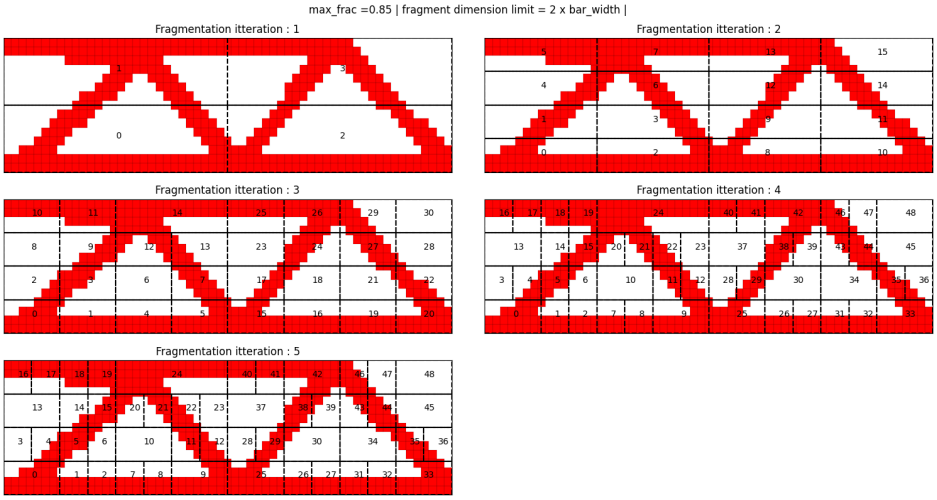

Figure 7.3: Redundant area isolation based adaptive fragmentation

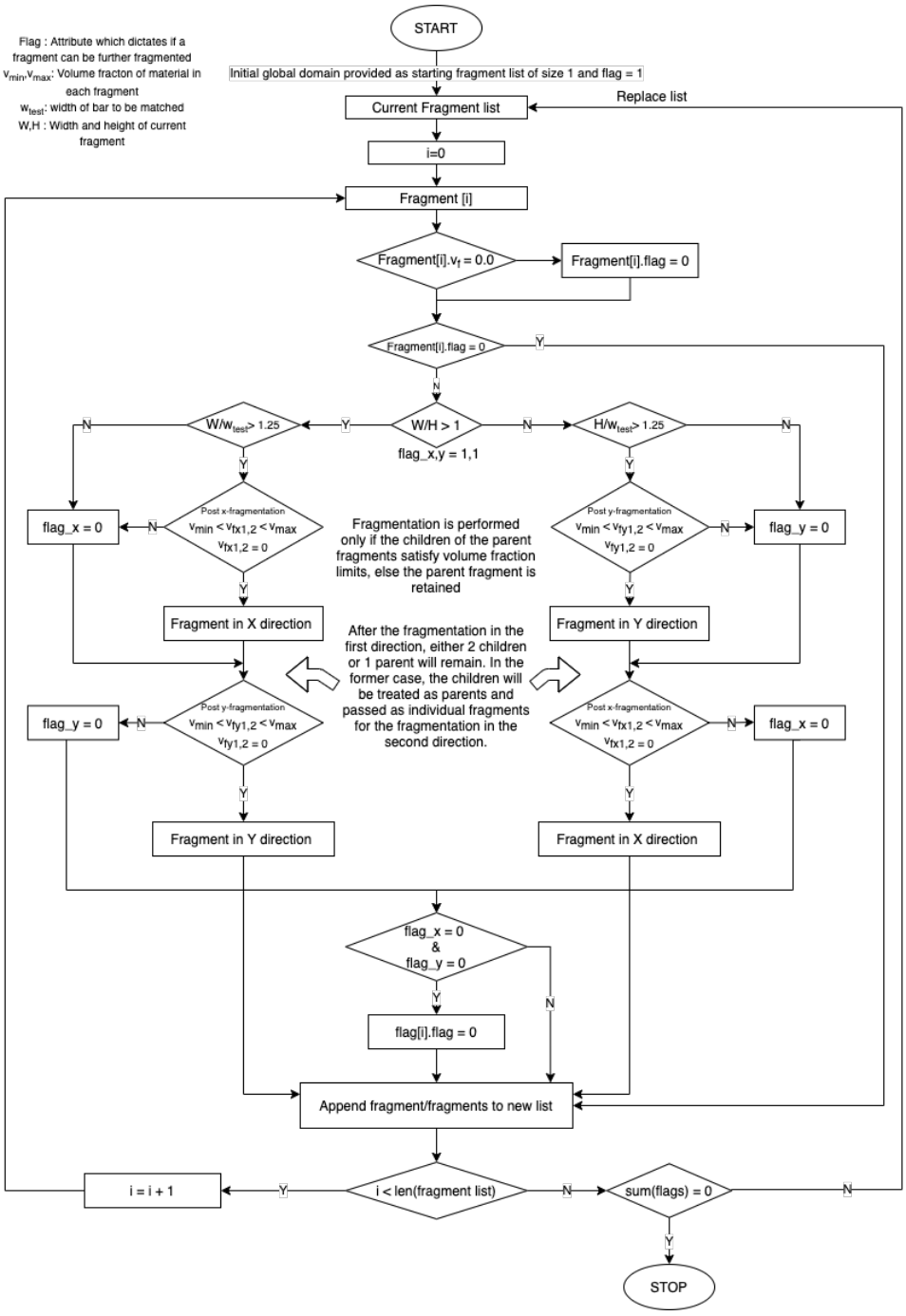

Figure 7.4: Volume fraction limited fragmentation.

7.2. BAR POINTS POST-PROCESSING

As a consequence of the fragmentation, the ability of bars to acquire globally optimized positions is hindered. The minimization of the matching domain has led to individual bars acquiring locally optimized positions throughout the domain. This is not of any structural use immediately, as although the floating bars resemble the underlying TO solution, it is not capable of sustaining any load. Therefore, the fragment-specific bars need to be coupled systematically and a TO congruent frame/ grillage is to be extracted. To this extent, a set of post-matching processes and processing sequences are proposed. Figure 7.5 represents a raw matching result.

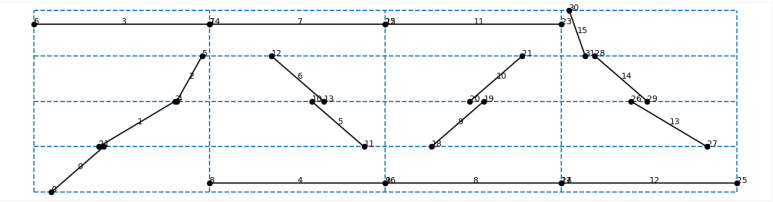

Figure 7.5: Raw matching solutions.

7.2.1. BAR POINT MERGING

Keeping in mind that the underlying topology being matched is continually connected, it is analytical to expect that the bars that are being matched will reflect the same. But, due to the act of matching a continuous bar to a piece-wise intensity distribution of the FEM TO image, leakage, and aliasing in the search, irregularities are expected. Therefore, the endpoints of bars in adjacent fragments need to be unified if suitable and in the vicinity. Two proposed capable methods are:

1. Common Edge merging: If the endpoints of the two bars are on the common edge of adjacent fragments, the endpoints can be merged. This aids in achieving the continuity of the underlying topology. Therefore any set of points lying on the same edge will be unified at their average position. This is demonstrated in Figure 7.6a on the cantilever solution.

2. Radial cluster merging: If multiple endpoints cluster together in close proximity, these points may be combined. This compensates for cases where due to fragmentation, a single point that is supposed to be an endpoint for multiple bars is replaced by multiple points and for cases where the endpoints of two bars occur in close proximity on the commonly extended edges of two adjacent fragments. The merging algorithm proposed utilizes a form of the smallest circle algorithm, where a set of closely packed points are identified and if the cluster falls within a circle of specified radius, the points can be unified at the center of said circle. This is demonstrated in Figure 7.6b on the cantilever solution.

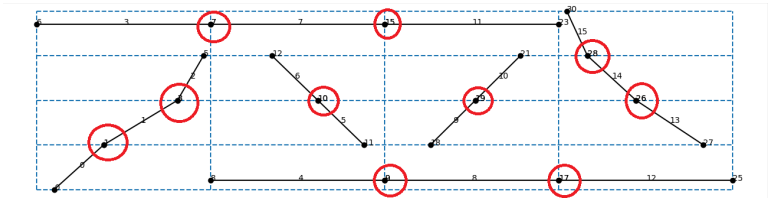

(a) Edge points merging

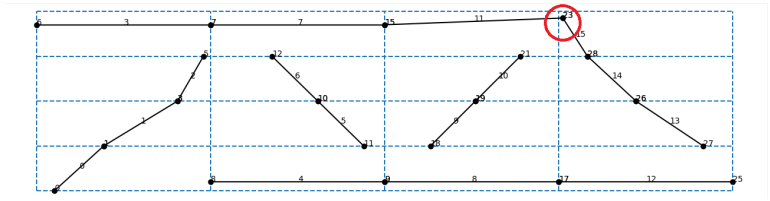

(b) Radial cluster merging.

Figure 7.6: Bar point merging operations

7.2.2. STRAND IDENTIFICATION AND EXTENSION

Although the endpoint merging allows for a significant reduction in the number of floating bars, it can often lead to merged bar strings being left unconnected. These strings of bars or 'Strands' need to be coupled together suitably. To take advantage of the inherent tendencies of the strands themselves, the connection point can be established by finding the nearest endpoint of the first intersecting bar when the strand end is extended. A radius of intersection is proposed as well, this helps to provide a working tolerance to enhance the capability of utilizing any inherent tendencies to intersect. This is illustrated in Figure 7.7 and demonstrated in Figure 7.8 on the cantilever solution.

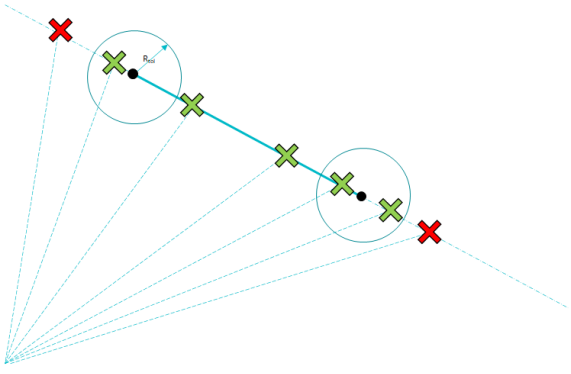

Figure 7.7: Strand extension with a radius of tolerance.

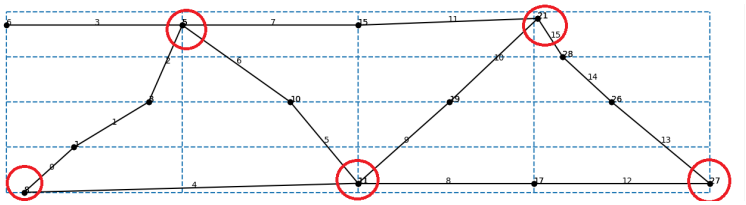

Figure 7.8: Cantilever strand creation and extension.

7.2.3. CONTROL POINT IDENTIFICATION

Given that the underlying TO solution is generated based on a set of loading and boundary conditions, it is logical to assume that these points are represented as endpoints in the generated frame structures. Therefore a localization step to move the nearest bar endpoint to these control points (BC and Loading points) is essential in mirroring the essential and natural boundary conditions of the TO solution. This is demonstrated in Figure 7.9 on the cantilever solution

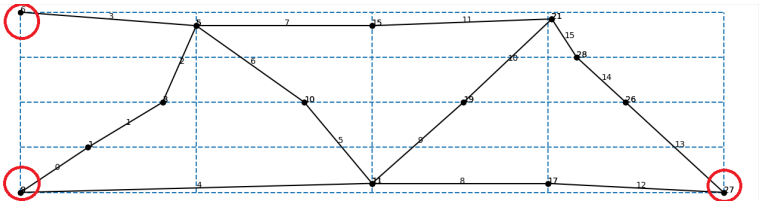

Figure 7.9: Control point movement

7.2.4. STRAND SIMPLIFICATION

Given that the fragmentation and the subsequent processing yields a string of small bars, and keeping in mind that the goal is to simplify a hard to manufacture structure, any long string of small bars needs to be simplified into a reduced set. To this extent, a sequential angular difference-based bar unification is implemented. The simplified strands can be considered as individual parts. This is demonstrated in Figure 7.10 on the cantilever solution.

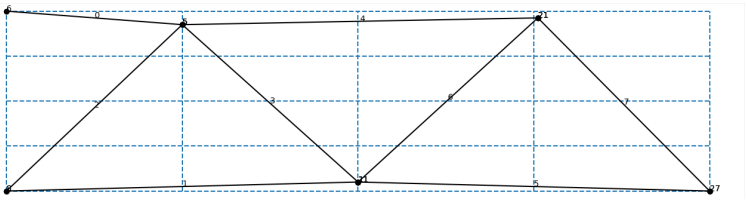

Figure 7.10: Strand simplification/Part creation

7.2.5. PROPOSED SEQUENCE AND OPERATIONAL PARAMETERS

From preliminary investigations, it can be deduced that the proposed processes are not commutative i.e. the sequence of operations have a huge influence on the resulting structure. Based on a preliminary investigation, a sequence for the execution of the operations is proposed. This sequence proves to be the best in achieving the closest representation of the underlying reference TO solution. Although the proposed sequence is what will be utilized, it is to be noted that the operations themselves can be executed in any order since they are independent. The proposed sequence post any matching is:

1. Common fragment edge merging: This process requires no tailoring of any parameters.

2. Radial cluster merging: Cluster merging utilizes a radius parameter that decides the largest circle of clustering to be considered. A proposed radius is 10 - 20 % of the fragment and is suggested to be reduced if required. (In the case of uniform fragmentation, in the case of adaptive fragmentation, this would require tailoring)

3. strand extension: A strand identification step identifies strands as a set of connected bars. A suggested step is to sort the strands in the increasing order of their lengths (in a number of bars) and to extend them in the same. A 25-30 % extension radius tolerance is proposed and is suggested to be minimized if possible.

4. control point movement: The Control points are both the loading and boundary condition points and if the matching is performed over a complex structure piecewise, the user must provide a suitable set of control points to ensure continuity between the sets.

5. Strand simplification: A 22.5 angular tolerance for the unification is proposed as a starting point and can be increased based on the requirement.

Figures 7.5 to 7.10 represents the elegant transformation of the raw matching solution into a load capable frame structure and Figure 7.11 showcases the conversion in comparision to the underlying TO solution.

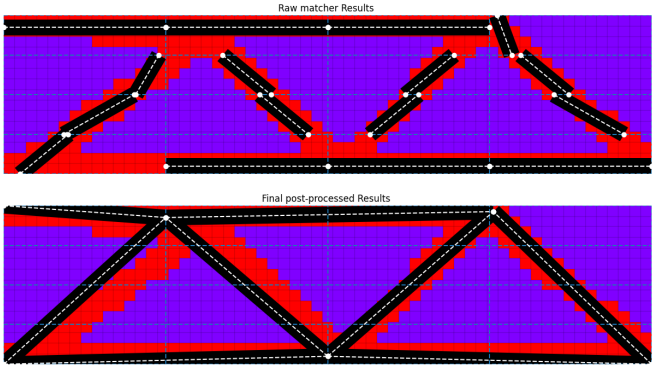

Figure 7.11: Post processing of bar matching results with proposed sequence of operations. $r_{merge} = 0.5R_{circumscribe}$,

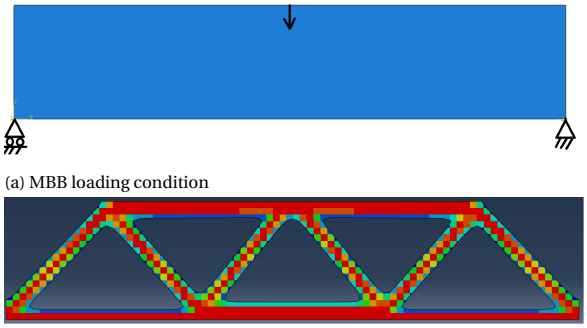

(a) MBB loading condition

(b) MBB TO solution

Figure 7.12: MBB Loading condition and TO solution.

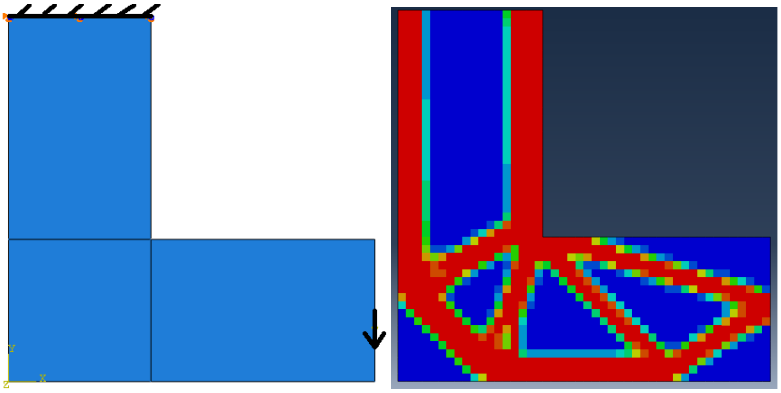

(a) Loaded knee loading condition

(b) Loaded knee TO solution

Figure 7.13: Loaded knee Loading condition and TO solution.

7.3. MODULARIZATION

The post-processing of the bar matching results forms the tail end of the moment matching-based modularization framework. The cumulative operation of the fragmented bar match followed by the post-processing ideally must produce a modularized structure identical to the underlying TO solution. This basic form of modularization is evaluated using a set of study cases from literature [17]. The cantilever beam, the MBB, and the loaded knee are common study cases in TO and were utilized to illustrate the capabilities of the developed methodology. Figures 7.12 and 7.13 illustrate the loading conditions and the cooresponding TO solutions for the MBB and Loaded knee. The three cases are evaluated with UF well as AF techniques and are post-processed to produce modularized solutions. The proposed modularization framework is represented through a flowchart in Figure7.19.

Of the two fragmentation techniques proposed, the uniform fragmentation method is iterative which requires specification of uniform domain discretization to be employed throughout the domain leading to a conundrum to choose the most suitable fragment size. The act of dividing a complex topology into uniform fragments that are to be matched with single bars is one that is assured to lead to erroneous structures if the fragment sizes are not compatible. Figure 7.17 illustrates this phenomenon with a general matching study conducted with varying fragment sizes for the cantilever beam and the corresponding post-processed results in Figure 7.18. As expected, a significant set of the studied structures lead to undesirable structures, some of which completely violate any resemblance to the load path in the underlying TO solution. Also, in each of these cases, the post-processing parameters must be tailored individually rather than using a constant value throughout, which requires the uniform fragmentation technique to be further tailored.

Although the adaptive fragmentation study requires the same post-processing parameters to be tuned, the size of the fragments themselves are more analytically decided based on the local topology, which makes the adaptive fragmentation method considerably superior. Given the bar width to be matched, the adaptive fragmentation strategy identifies the suitable fragments in a region without affecting the neighbors, therefore removing one of the tailoring aspects required by the uniform fragmentation strategy. Figures 7.14, 7.15 and 7.16 illustrate the modularization of the cantilever, loaded Knee and MBB TO solutions respectively using the AF strategy. Therefore, each of the chosen study cases is successfully converted from an element-based TO solution to a bar-based frame structure, therefore modularizing them. Although the module similarity is limited to its cross-section, the ability of the fragmented matching methodology to discretize the continuous structure is still a basic form of modularization.

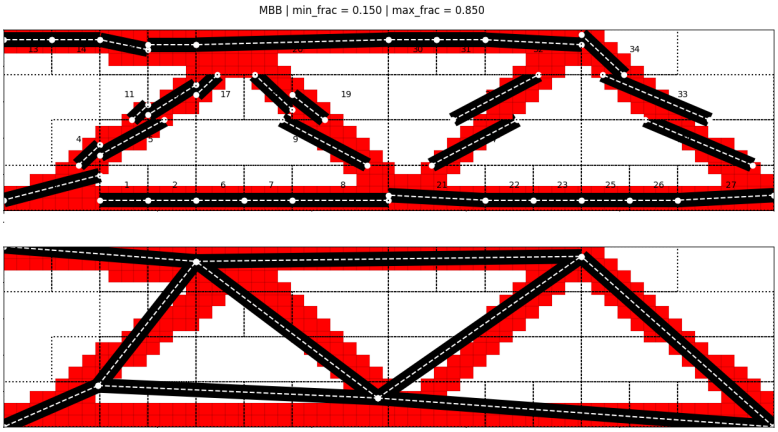

Figure 7.14: Adaptive fragmentation cantilever modularization.

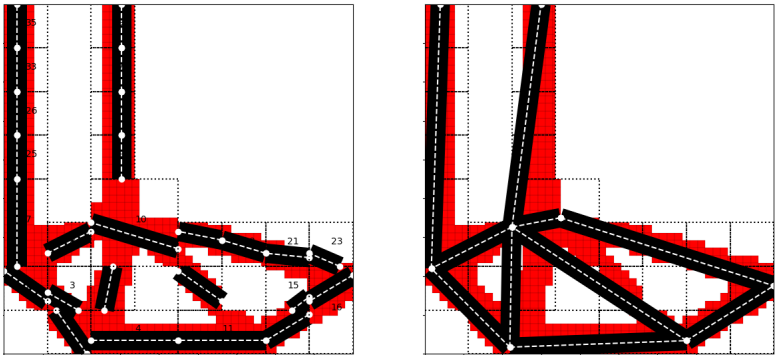

Figure 7.15: Adaptive fragmentation loaded knee modularization.

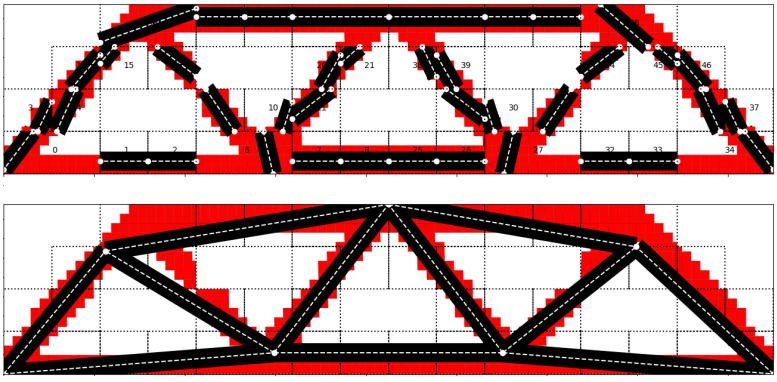

Figure 7.16: Adaptive fragmentation MBB modularization.

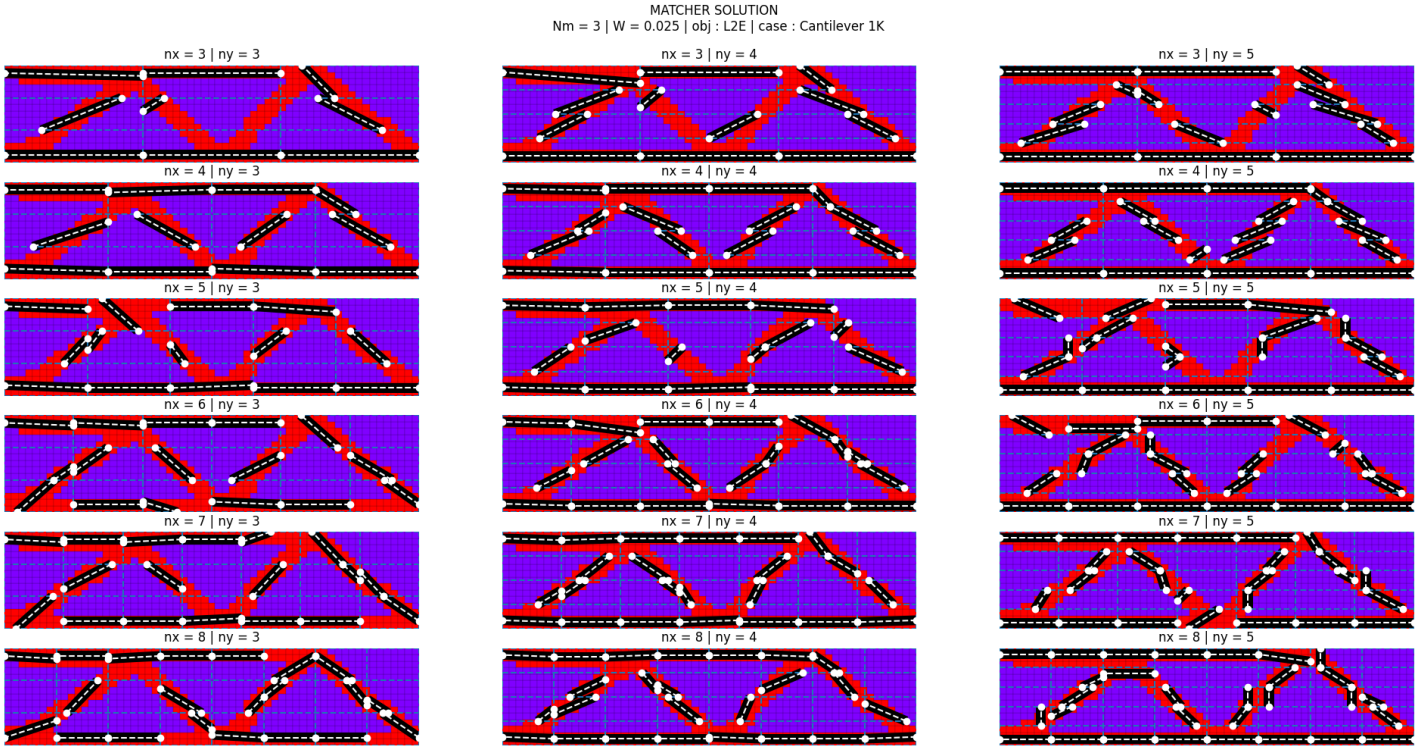

Figure 7.17: Uniform fragmentation study cantilever beam raw matching results.

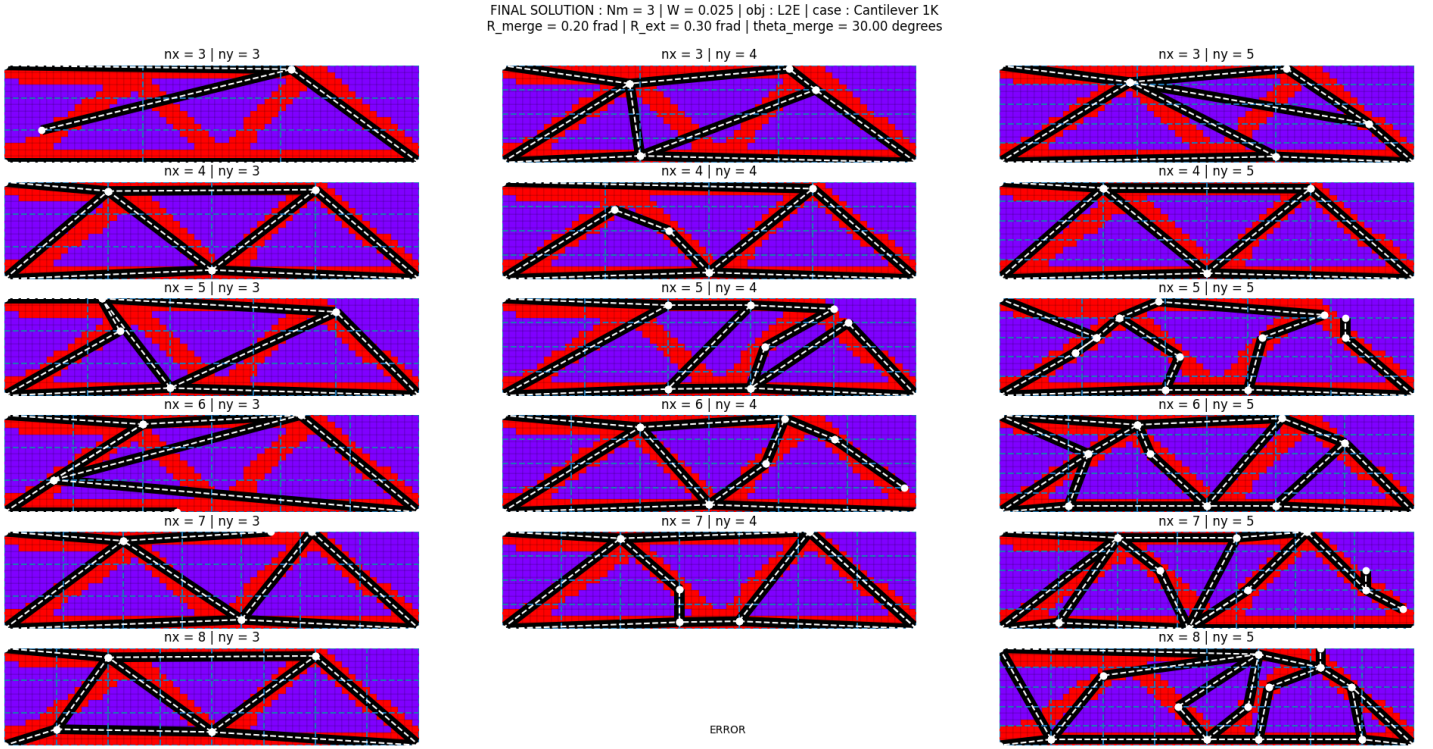

Figure 7.18: Uniform fragmentation study cantilever beam raw post-processed results.

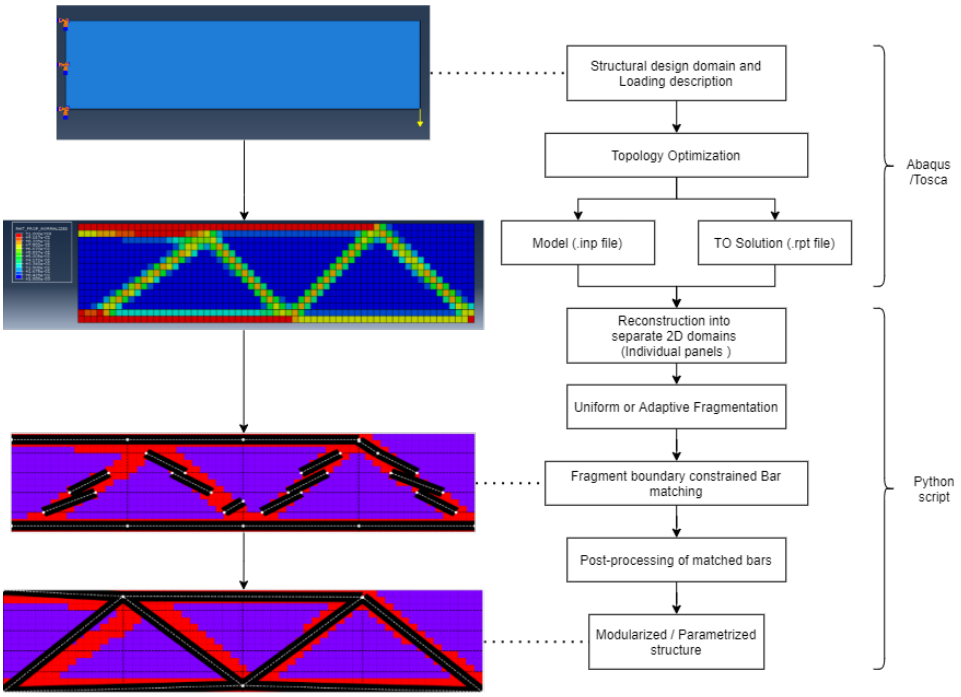

Figure 7.19: Modularization framework developed/proposed.

7

7.4. G5 PANEL MODULARIZATION

The G5 galley is comprised of a set of interconnected panels in the 3D space and in contrast the moment matching framework developed is rooted in 2D. This limitation can be overcome by suitably separating the panels beforehand, and each panel can be modularized individually. Once suitably modularized the panels can be reconstructed to obtain the G5 galley as a whole. Figure 7.20 depicts the result of the modularization for one such panel (39)[1]. The AF strategy employed shows promise in its ability to identify suitable fragment distribution in the domain and the corresponding bar matches when the post-processed result in a structure which largely resembles the underlying TO solution. Most of the major branches of the TO solution are well duplicated in a discretized form.

[1] The TO results utilized here are those belonging to the solution for the compliance minimization with 30% volume fraction

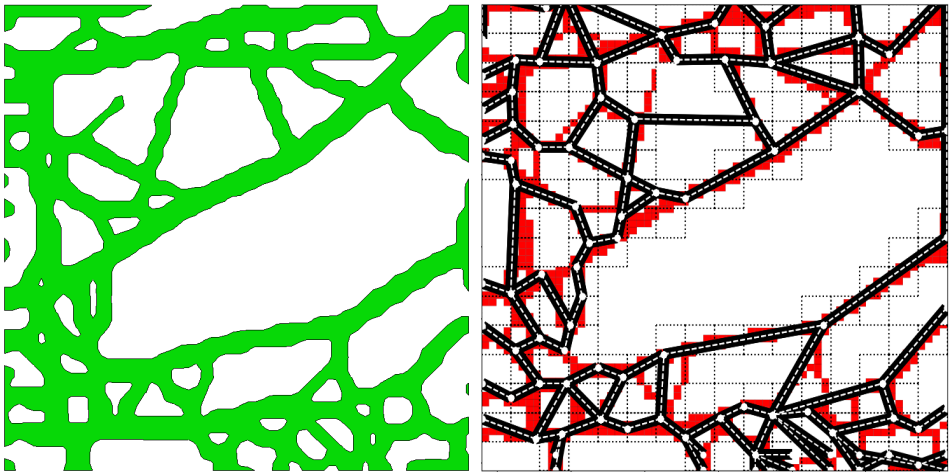

(a) TO Solution (b) Bar match

Figure 7.20: Panel 39 fragmented,post-processed solution.

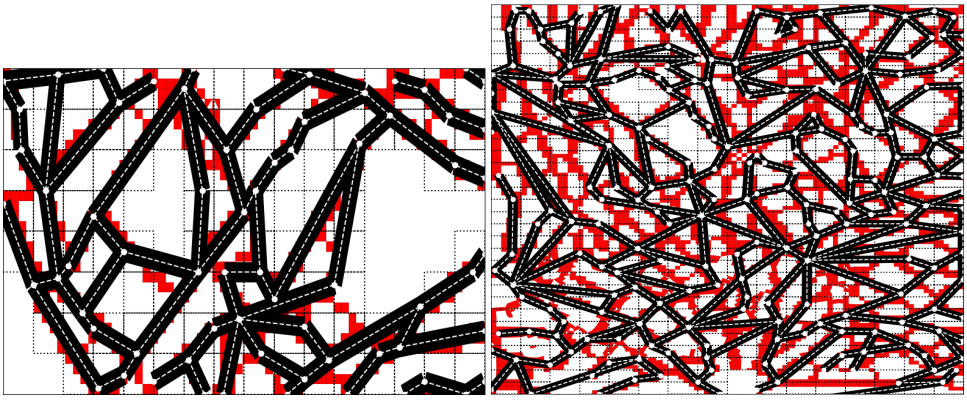

(a) Low volume fraction panel 25%. (b) high volume fraction panel 50%.

Figure 7.21: Volume fraction influence on the modularization of TO solutions using the moment based framework.

Although the framework developed is designed with a goal to modularize any TO solution, the application of the complex topologies obtained in the G5 galley panels yields some of the shortcomings of the methodology. Within Figure 7.20, the AF-based bar match has been able to capture to a large extent the optimized load paths of the TO solution. However, on closer inspection, the resulting modularized panel does not include some of the noticeable connection points as well as connecting members. Although this absence of members does not play a significant role visually, a direct application of the design loads onto the modularized panel assembly would display entirely different load

paths than those optimized for in the TO solution. This erroneous approximation of the TO solution is aggravated as the volume fraction of the material in the domain is increased. Figure 7.21 illustrates the modularized result obtained from 2 other panels in the G5 galley, one with 25% volume fraction and one with close to 50% volume fraction. The former indicates an excellent translation of the TO solution into a frame-based structure, whereas the latter panel indicates a comparatively poor approximation. The cause for erroneous matches can be possibly accounted for by 2 factors: post-processing parameters and the effect of fragmentation.

The post-processing strategy developed is in essence a set of approximation functions that attempt to utilize information from the fragment wise bar match to realize suitable structures. However, these parameters are highly subjective in their efficacy and require to be tuned/tailored to yield suitable solutions. Therefore, in general for an acceptable modularization, these parameters need to be investigated thoroughly for each fragmentation application. The parameters proposed in Section 7.2, can be used as a starting point and have proven to be capable for the 3 case studies from literature, yet they were proven insufficient for the topologies of the optimized G5 panels. Therefore, for complex topologies, the tailoring of these parameters becomes much more important.

However, an underlying misappropriation of the TO solution caused due to fragmentation cannot be entirely negated by the tuning parameters. As described in Section 6.5, the L2E objective is highly nonlinear, therefore requiring fragmentation of the TO solution and the adoption of a localized matching strategy. As a consequence, both the developed UF and AF strategies function over rectangular fragments arranged side to side. However, the complex TO solutions obtained are not constrained to shapes aligned at 0 or 90 degrees. Therefore, the matching is performed with an inherent assumption that the TO features cross over only at the fragment edges and that multiple features do not coalesce within a certain fragment. This limits the suitable topologies to those of low volume fractions since, as the volume fraction increases, feature sizes increase and the coalescence of features begins to occur within the fragments. The AF strategy although aims to alleviate this problem, by choosing the fragment sizes carefully based on the localized topologies, the fragment size itself is still limited, i.e, for a rectangular domain of size X and Y in the x and y direction, the fragments can be of size $X/2^n$ and $Y/2^n$ and these fragments can only achieve a certain limited set of positions within the domain, as the neighboring fragments themselves are decided based on their own local topologies and as a whole, all the individual fragments must globally reconstruct the initial domain of dimension X and Y. This can lead to unconnected bars for the matching of TO features crossing over at the corners of fragments. Also, in cases where the fragment sizes are smaller than the feature in the TO solution, stray bars can be introduced. The tailoring parameters such as the minimum and maximum volume fractions and the post-processing strategies in Section 7.2 aim to avoid and compensate for these effects. However, such complexities cannot be entirely eliminated. The results of the G5 panels represent the negative effect of these remaining intricacies which are a byproduct of the fragmentation approach.

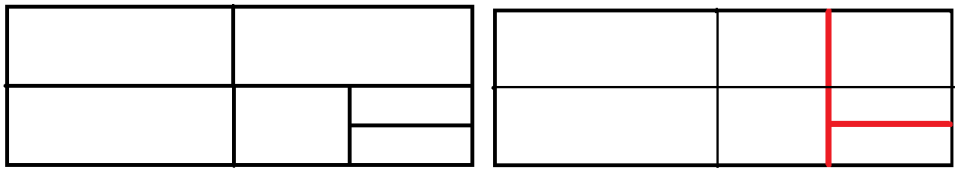

(a) Compatible (b) Incompatible

Figure 7.22: Compatible and incompatible fragments. The AF strategy produces only compatible fragments with the dimensions limited to $\frac{w}{2^n}, \frac{h}{2^m}$ with domain dimensions w, h.

Nonetheless, the modularization framework developed offers a preliminary strategy to translate TO solutions as well as provides an avenue for further processing.

7.5. PARAMETRIZATION AND SECONDARY DESIGN OPPORTUNITIES

The developed framework aims to describe the monolithic TO solution as an assembly of sub-structures/modules in this case bars of uniform width and varying lengths. As a consequence of the framework developed the modularized structures are described parametrically through a set of bars, points, and their coordinates. This computational strategy allows the obtained result to be directly translated to suit truss/frame-based optimization problems. Therefore, by using the simplified model of the structure additional requirements can be investigated.

As mentioned in Chapter 4, the galley self-weight itself was omitted from the loading during TO. The parametric solution obtained offers an opportunity for the omitted requirement to be reintroduced and compensated for. Additionally, the parametrization offers the scope for other design requirements and limitations to be considered such as:

1. Stress constraints: The optimized load path identified through TO is to some extent retained when modularized. However, the strengths of the beam elements require consideration as well. Through the simplified model obtained, a straightforward continuous or discrete sizing optimization can be performed to identify a capable set of profiles and sizes for the individual truss/frame elements.

2. Natural frequency considerations: Once modularized the stiffness of the structure can show large variation due to the change in form from a continuous structure. Therefore the natural frequency of the structure can vary to a large extent. This effect is further aggravated if rather than using the same material as optimized for, the optimized load path is reconstructed with alternate materials such as composites. Therefore, natural frequency analysis can be conducted on the structure to adapt the obtained structure to the requirements as well as compensate for material choice.

3. Stability considerations: The TO framework employs a linear FEM model to optimize the given structures. However, as the volume fraction constraints reduce and the obtained topologies approach slender members the resulting structures inevitably present non-linearity. Therefore, phenomena such as buckling which are entirely omitted in the design considerations increase in importance. The modularization framework provides an alternative to Non-linear FEM-based TO to address such effects through a simplified truss/frame model of the slender structures generated.

Additionally, from a manufacturing perspective, the use of the simplified model allows for studies to be considered similar to those discussed in Sections 5.1 and 5.2. One of the critical influences of modularization is its influence on performance. Within the scope of TO, a study on how the size of TO features influences the performance involves a large number of optimization routines to be conducted. However, through the modularization strategy employed, a much simpler post-analysis can be conducted using the simplified structural model to assess the influence of the module sizes. This offers a stage for more complex analysis as well. With the structure optimized for the given loading, the effect of the number of design variables on weight and cost can be conducted to extract break-even recommendations to obtain high-performing modular structures fit for mass production.[2]

Therefore, the moment-based modularization strategy although in its infancy is capable of being developed into a suitable strategy for utilizing TO-generated solutions. Few of the key limitations remain to be investigated; However, the formulated framework is deemed suitable by the Author to represent the outcomes of the current project.

7.6. SUMMARY

To summarize, based on the fragment boundary search strategy proposed in Chapter 6, this chapter proposes two fragmentation strategies that can be employed for 2D TO solutions. Following this, a set of post-processing operations are proposed which best embody the augmentations required for the extraction of load-capable structures from the fragment wise bar match. The bar matching, the fragmentation strategies, and the post-processing operations are encompassed within a framework that accepts TO solutions from Abaqus and operates on the results in Python to return a truss/frame-based modularized design in a parametric form. The framework is assessed on TO case studies from literature and to conclude, employed on a limited set of panels from the G5 TO solution. To conclude, a few of the limitations and possibilities offered by the framework are briefly commented on.

[2] Appendix includes a preliminary study conducted by the Author in the effort of demonstrating such a post-analysis with the simplified model obtained from the developed framework.

8

CONCLUSIONS AND RECOMMENDATIONS

Drawing attention to the first research goal posed in the introduction:

> *Can topology optimization be employed on a galley structure? If yes, how can a suitable/practical structure be generated?*

In order to find an answer, firstly a literature survey was performed where the computational framework for TO and the numerical implementations of the various design constraints were reviewed. A brief analysis of the current design strategy was conducted to interpret the structural requirements of the galley to be implemented into the TO framework. Utilizing the information from the Literature survey, the certification and operational requirements of the chosen G5 galley were translated into suitable objectives and constraints for TO. Based on the required resolution and capabilities of available TO tools identified in the literature survey, ABAQUS-TOSCA was chosen for employment. The direct TO result using the chosen objectives and constraints yielded impractical solutions with localized elimination of material. Additional geometric constraints were found to counteract the localized material elimination and generate a pragmatic galley solution.

Thus, to answer the first research question: Yes, the G5 galley can be topology optimized. By suitably modifying the loads to be compatible with the TO formulation and additional geometric constraints, a practical galley structure can be generated using TO. Through the use of the resource and reaction force constraints, a structure of equal weight to the current solution as well as a structure capable of being interfaced with the aircraft was generated. The metal galley generated showcases a skeletal architecture comprised of slender members extending from the interface locations.

The successful solution to the first research goal allowed the project to proceed to the second research goal.

> *How can a topology optimized galley be suitably modularized into simple modules?*

To understand the benefits modularization offers the literature survey additionally investigated the performance and cost influence offered by modularization. The common methods in the literature for feature extraction in TO were studied to identify methods that could be capable of modularizing the galley TO solution. A scarcity was noticed within the literature for methods to truly modularize TO structures.

An analogous nature was observed between the modularization of TO and the act of shape matching in image processing. Therefore, a novel image moment matching approach was proposed for investigation. The hypothetical moment matching approach offered the ability to identify modules within TO solutions similar to identifying shapes in digital images. Therefore, the initial investigation included an assessment of the ability of moment matching to provide the suitable positions of bar modules within TO solutions. However, as a consequence of the non-linearities presented by the chosen objective, the global bar matching resulted in the settling of bars at local optimal. To overcome this problem, the bar matching optimizer was augmented to be constrained within fragments of the initial domain, and thereafter the initial global matching process was converted to a fragment-wise matching process. In the interest of generating compatible matches as well as reducing the solution space, the optimizer was simplified to a fragment boundary search operation with a brute force search for the optima within a limited set of bar positions.

In order for the fragment boundary search to be employed, the TO solution domain is required to be suitably fragmented. Therefore, a uniform and an adaptive fragmentation strategy were formulated. The UF strategy follows a straightforward division of the entire domain into uniformly sized fragments but proves to be rather crude in implementation. The AF strategy was developed based on the standard quad-tree meshing strategy with additional tailoring in the context of TO. A set of post-processing methods and the corresponding sequence of operation was developed for the generation of load-capable modular structure based on the fragment-wise bar matching solution. The unified pipeline of the topology optimization process followed by the moment matching and post-processing forms the modularization framework developed in this thesis. This framework was successfully employed on 3 TO solutions recreated from literature and in each case a truss/frame-like structure was successfully generated.

Subsequently, the modularization framework was employed on the optimized galley panels. It was observed that the moment matching method was successful in achieving a partial skeletal similarity within the low volume fraction G5 panels. However, a noticeable amount of inconsistency was observed. Panels with low volume fractions could be modularized whereas the panels with material more than roughly 50% of the domain

yielded sub-par results. This most likely could be the consequence of the fragmentation approach as well as the choice of the tailoring parameters.

8.1. FINAL RECOMMENDATIONS

Owing to the maiden implementation of topology optimization on galleys and the novel nature of the moment matching principle, the topology optimization formulations inspected and the optimization strategies employed for the moment matching were largely limited. Given the investigations performed and observations obtained during this thesis, the work can be expanded and alternative strategies can be considered. This section presents the Author's recommendations for further exploration as well as any following related works.

As the preliminary goal of the thesis was the investigation of modularization strategies, a largely straightforward strategy is applied for the galley optimization. The proposed TO formulation is capable of producing solutions, yet it remains rather blunt in its implementation of multiple load cases. The choice of compliance summation as the objective allows in providing equal importance to all the load cases. However, an alternative to this methodology could be a weighted summation which can incorporate the importance or critically of each load case through said weights and could allow for neutralizing of redundant load cases and improve the convergence of the optimization.

The key necessity to generate viable solutions required the inclusion of geometric constraints within the framework. Within this work, due to the mesh size chosen, a maximum geometric constraint was found to be the most compatible form of the constraint. The choice of mesh size was primarily due to the computational limitations. However, if the mesh were to be further refined, a well-posed geometry constraint can be implemented which can allow for more well-defined topologies to be generated. The implementation of more strict geometry constraints also allows for a more suitable choice of bar dimensions for modularization further down the pipeline.

The moment matching principle utilized in this work had been previously investigated in the context of image comparison, however, it had never been investigated for its capability for image approximation through secondary elements. Therefore, much of the observations found in this work form a possible foundation for future work. Although the usage of the L2E as the objective allows for the identification of global optimal, its non-convex and non-linear nature led to considerable constraints on the optimization strategy. However, the utilization of other optimization strategies could offer an alternative to access the global optima without significant constraints. Meta-heuristic methods such as simulated annealing or Genetic algorithms can be preliminary alternatives for further investigation. In regards to Genetic algorithms, a preliminary ground structure-based L2E optimization using GA was demonstrated by the author and its results are available within Appendix A. Additionally, the current work investigated modularization only through the use of bar/beam-based modules. However, the moment matching is principle is universal in its capability of comparing shapes, i.e, rather than single bars

elements such as triangular frames and curved beams could be used to modularize a TO solution. Future works can also investigate alternative objectives such as the cosine similarity, magnitude weighted norms and image reconstruction error.

The Fragmentation strategy investigated and developed in this thesis has been limited to rectangular shapes. Even the AF strategy, though more flexible than the uniform fragmentation, still remains a product of the Quad-tree-based meshing. The inherently perpendicular edges of the fragments have been shown to be problematic in the case of complex TO solutions. A possible alternative to be investigated is the use of generalized quadrilateral-based fragmentation similar to free-form quad meshing. By limiting to convex quadrilaterals, the fragment-wise matching can be performed through remapping of the Legendre domain. This strategy naturally provides more flexibility in comparison to the adaptive fragmentation strategy used.

The post-processing steps required for tailoring the matched solution into modularized frame structures requires some attention as well. In this work, a preliminary sequence of operations is provided. However, this sequence has proven to fail in the case of complex TO solutions. One possible strategy is to identify features which can dictate the sequence of operations rather than using fixed operational sequence. This could also be performed by monitoring the matched solution after every post processing sequence to quantify if the proceeding direction is preferable or not.

Finally, a key motivation for this work of modularization of TO structures was to study its influence on its cost and performance. As a byproduct of the modularization, a parametrized model is created which defines the structure as an assembly of modules. In this work, the TO solution is obtained as an assembly of bar/beams and is parametrized as a function of the coordinates of the endpoints of each bar and the connectivity of each of the modules. This parametrization approach can be used as a preliminary model to evaluate the influence on manufacturing costs as well as performance. Through the finally obtained reduced model a novel technique is obtained to assess the performance and cost implications of designs obtained from topology optimization. A preliminary 2D form of this is depicted in A to study the weight, stress, and natural frequency implications of the variety of dimensions in a cantilever frame.

A

APPENDIX

This chapter presents some additional points of discussion and results pertaining to the thesis performed. This includes manufacturing considerations for the optimized galley, stiffness implications of the choice of a metal frame and numerical refinement considerations for bar matching.

A.1. METAL G5 MANUFACTURING CONSIDERATIONS

The G5 TO solution obtained is starkly contrasting with the current product. Although the TO solution retains the basic architecture of the original galley itself, the TO solution comprises slender branches of materials spreading throughout all the panels. This very feature symbolizes the key motivator to investigate truss/frame based modularization strategies. However, the alteration of design from a panel based design requires suitable augmentation of the manufacturing strategy to obtain a functional galley. The key factor to be considered is the largely empty panel regions. The low volume fraction of material is an unavoidable byproduct of using metal as the design material for TO and the unsaid requirement of any new design to be on a par with the previous designs, specifically for the weight to be the same as before. However, for a functional galley, flat operating surfaces and completely covered panels are necessary. This can be addressed through a thin covering skin. This design strategy was employed by AIRBUS to cover the frame like partition wall as illustrated by Figure A.1 and is a proven design strategy in electronics design to cover internal parts with thin moulded plastic panels.

A

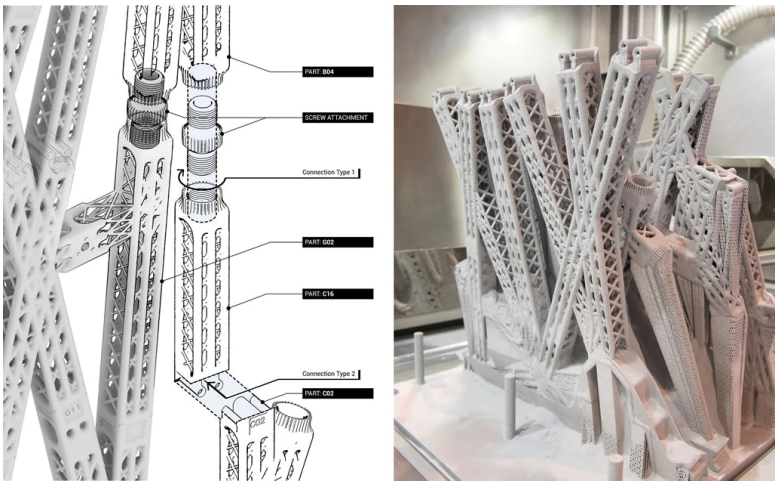

Figure A.2: Bionic Partition manufacturing and assembly [5].

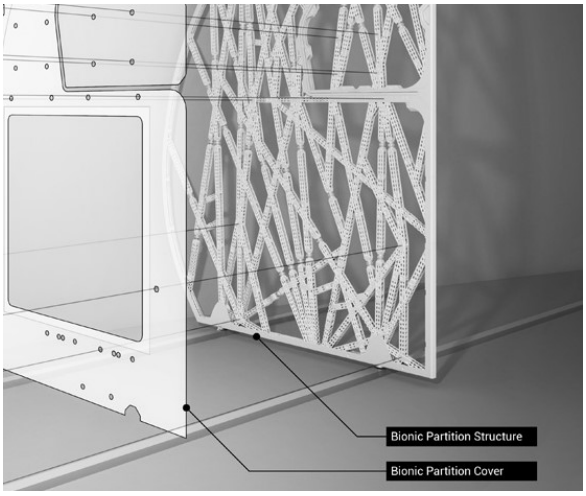

Figure A.1: Skin covered frame structure

From a modularization perspective, the manufacturing of the individual modules and the adjoining assembly requires addressing as well. AIRBUS achieved the manufacturing requirement through additive manufacturing [2] of the individual elements and assembly through custom screw joints as illustrated in Figure A.2. However, as addressed in Chapter 5 the use of additive manufacturing is limited to custom products.

From a modularization perspective, the individual modules are essentially simplified and can be replaced with simple metal rods or hollow sections. Through the use of identical section/profile throughout the structure the manufacturing task is reduced to

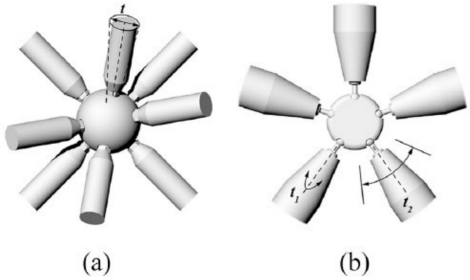

Figure A.3: Spherical ball joints and ball socket joints used in space frame construction [63]

cutting the rods/pipes to the required lengths. This allows for highly simplified certification as well as provides scope for automation. A common method employed to construct frame assemblies is through the use of spherical ball joints and ball and socket joints as illustrated in Figure A.3.

A.2. STIFFNESS OF FRAME BASED PANELS

The typically galley structure is comprised of composite sandwhich panels. This can largely be attributed to their excellent stiffness to weight ratio. From a material stiffness perspective, most of the structural stiffness for sandwhich panels lie in the composite plies of the skin. The composite skin of the panels provide flexural stiffness due to their excellent in-plane properties. This leads to most of the stress profile being localized at the skins during any out of plane loading. In comparison, isotropic metal panels provide equal stiffness contribution throughout the width of the panel. The replacement of the sandwhich panels with the metal frames can be visualized as the relocation of the stress from the narrow skin regions to a distribution across the width of the metal frames. It is interesting to note that this strategy completely opposes the choice to use composites. However, if the individual modules and fragments can be optimized further, the capability of such a frame structure can exceed the performance of the composite counterpart. This was illustrated by the metal frame based partition wall as illustrated in Figure 5.11. Therefore, once the modularization is performed with uniform width bars as proposed in Chapter 7 the performance can be enhanced using alternative frame sections with the same frame architecture. Although in the case of the bionic partition, this was achieved through additively manufactured frame elements, the use of standard profiles is more of prudent strategy from a cost efficiency and modularity perspective.

A.3. P-REFINEMENT OF NUMERICAL MOMENT CALCULATION

As prescribed in Section 6.4, the Legendre moments of the TO solution are calculated through an element-wise summation of the Gaussian quadrature based discrete integral. Although from the orthogonal frame of reference, the choice of the order of the Gaussian

quadrature can be made based on the order of the polynomial function along the respective axis, the S4 elements are in general arbitrary quadrilaterals and not rectangles with edges parallel to the coordinate axis. To offer a recommendation on the number of terms, a p refinement study is performed to study the LM of a bar calculated numerically using the L2E in comparison to the analytically calculated LM of a reference bar . Figure A.4 illustrates the L2E for varying size LM of varying integral point resolutions ($p \times p$). Due to the misalignment of the resolution direction of the integral points and the principal axis along which the Legendre moments are defined, the integration scheme to be employed is to be at least a single order higher than the order of L_n.

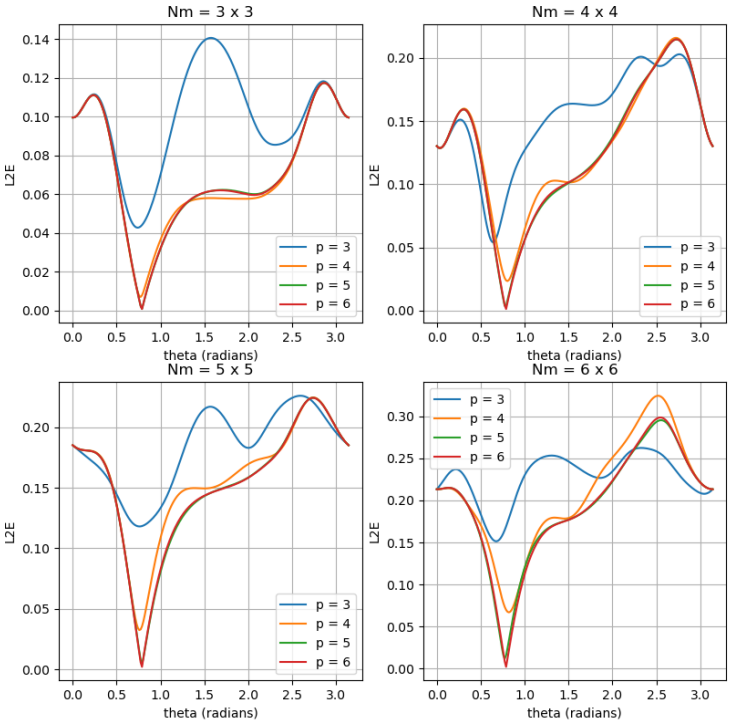

Figure A.4: Influence of L2E comparing numerical LM of a rotating bar and analytical LM of a reference bar (D[0,1,0,1] B[0.217,0.217,0.783,0.783]).

A.4. H-REFINEMENT IN FRAGMENTATION

The h refinement of the fragmentation is analogous to h refinement in finite element mesh. In general as the mesh is refined, the structural response display convergent properties. Similarly, as the fragment sizes are reduced, more finer and complex topologies can be incorporated and the resulting modularized result must theoretically exhibit a convergent behavior. This phenomenon was studied by varying the refinement of a uniform fragmentation FWBM for the Loaded Knee TO solution. Although the use of finer

fragments results in leakage issues as the dimensions of the fragment approach the width of the bar, Figure A.5 illustrates a near convergent phenomena for the compliance as the discretization in either directions increases. It is to be noted that this phenomenon is highly dependant on the post-processing parameters employed. In the investigated case a constant set of post processing parameters were utilized whereas a general recommendation is to tailor the parameters for each case. Therefore, as a recommendation for further study, a tailoring algorithm can be developed to identify these parameters for each case.

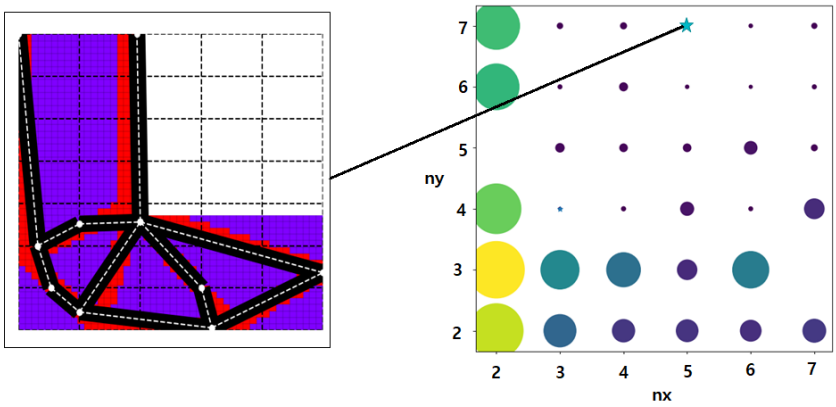

Figure A.5: Influence of h refinement in fragmentation on Compliance of final structure.

A.5. POST-ANALYSIS OF PARAMETRIZED SOLUTION

A byproduct of the image moment based modularization framework is a parametrized model comprised of simple elements described by their positions and their connectivity. In the current work, these simple elements are the truss/beam elements. Once the modularization is completed through the FWBM and the following post processing, the resulting structure is a much simplified frame structure as compared to the quad element based TO solution. This allows the resulting parametrized model to be further analyzed or optimized for attributes not included in the TO definition such as nonlinear behavior, failure mode etc. The parametrized model also allows for simplified cost and weight trade off analysis to be conducted to identify the number of variety of beam cross sections required to reduce cost as well as maintain performance. To this extent Figure A.6 illustrates a post analysis conducted to study the maximum stress, natural frequency and weight of the parametrized cantilever beam.

A

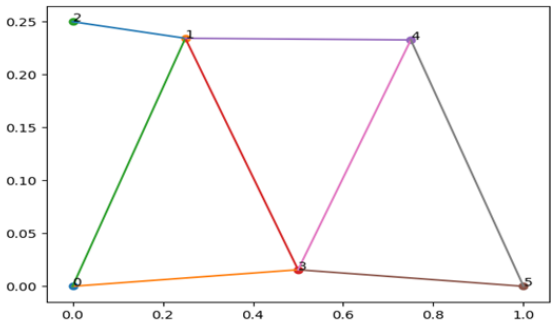

(a) Modularized/Parametrized TO solution of cantilever beam

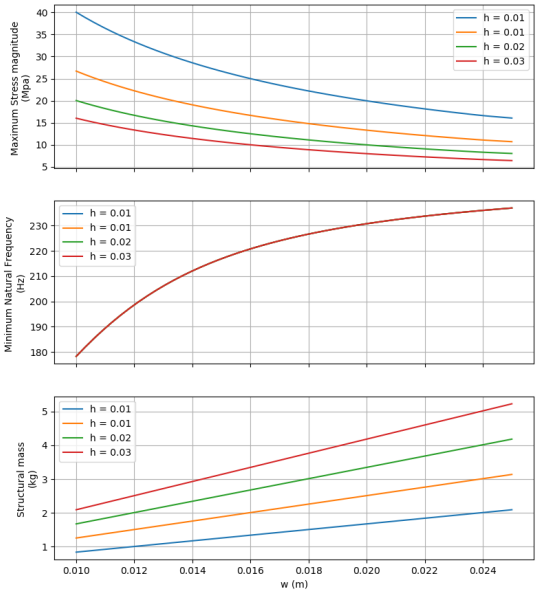

(b) Maximum stress, Natural frequency and weight as a function of inplane bar width w and out of plane depth h.

Figure A.6: post analysis of parametrized cantilever beam TO solution.

A.6. ALTERNATIVE OPTIMIZATION STRATEGIES

During the current thesis, the author's investigation is limited to the use of the gradient descent optimizer for the moment matching. However, due to the large non-linearities of the objective itself Meta-heuristic methods such as Genetic algorithms (GA) could be employed instead. A preliminary investigation conducted to optimize the L2E given a certain ground structure using Genetic Algorithms shows promise. The results in Figure

A.7 illustrates the solution obtained using a GA for a very simple ground structure. Although the solution is not perfect, the usage of alternative optimization strategies can be recommended for future investigations.

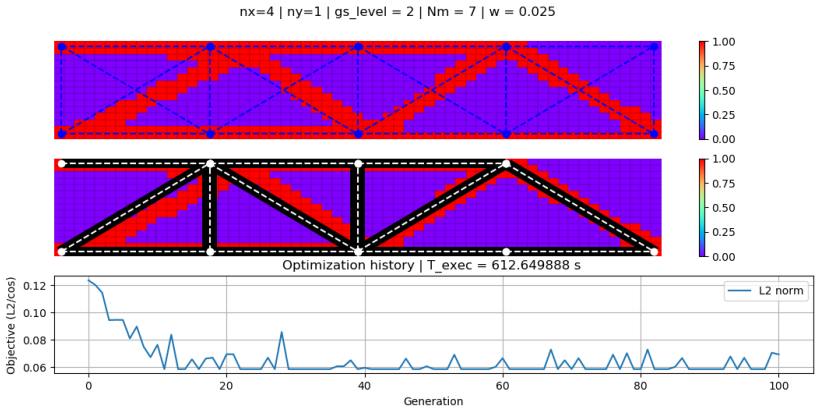

Figure A.7: Moment matching using Genetic algorithm

B

APPENDIX

The analytical expressions for the bar moments were obtained using symbolic integration through Sympy[79] . The functions to evaluate the moments are further hastened through precompilation protocolos provided by Cython[16]. For a given bar of length: L, width: W, centre positions: $x0$, $y0$, and orientation theta the expressions for the moments in $LM_{5\times5}$ is given here.

```
 LM_(0,0) = 0.25*L*W
 LM_(0,1) = 0.75*L*W*y0
 LM_(0,2) = L*W*(0.15625*L**2*sin(theta)**2 + 0.15625*W**2*cos(theta)**2 +
1.875*y0**2 - 0.625)
 LM_(0,3) = L*W*y0*(1.09375*L**2*sin(theta)**2 + 1.09375*W**2*cos(theta)**2 +
4.375*y0**2 - 2.625)
 LM_(0,4) = L*W*(0.4921875*L**4*sin(theta)**4 + L**2*(1.640625*W**2*cos(theta)**2 +
19.6875*y0**2 - 2.8125)*sin(theta)**2 + 0.4921875*W**4*cos(theta)**4 +
19.6875*W**2*y0**2*cos(theta)**2 - 2.8125*W**2*cos(theta)**2 + 39.375*y0**4 -
33.75*y0**2 + 3.375)/4
 LM_(1,0) = 0.75*L*W*x0
 LM_(1,1) = L*W*(0.09375*L**2*sin(2*theta) - 0.09375*W**2*sin(2*theta) +
2.25*x0*y0)
 LM_(1,2) = L*W*(L**2*(-0.9375*x0*cos(2*theta) + 0.9375*x0 + 1.875*y0*sin(2*theta))
+ 1.875*W**2*x0*cos(theta)**2 - 1.875*W**2*y0*sin(2*theta) + 22.5*x0*y0**2 -
7.5*x0)/4
 LM_(1,3) = L*W*(0.1640625*L**4*sin(2*theta) - 0.08203125*L**4*sin(4*theta) +
0.2734375*L**2*W**2*sin(4*theta) - 6.5625*L**2*x0*y0*cos(2*theta) +
6.5625*L**2*x0*y0 + 6.5625*L**2*y0**2*sin(2*theta) - 1.3125*L**2*sin(2*theta) -
0.1640625*W**4*sin(2*theta) - 0.08203125*W**4*sin(4*theta) +
6.5625*W**2*x0*y0*cos(2*theta) + 6.5625*W**2*x0*y0 - 6.5625*W**2*y0**2*sin(2*theta)
+ 1.3125*W**2*sin(2*theta) + 52.5*x0*y0**3 - 31.5*x0*y0)/4
 LM_(1,4) = L*W*(1.4765625*L**4*x0*(1 - cos(2*theta))**2 +
5.90625*L**4*y0*sin(2*theta) - 2.953125*L**4*y0*sin(4*theta) -
4.921875*L**2*W**2*x0*(1 - cos(2*theta))**2 - 9.84375*L**2*W**2*x0*cos(2*theta) +
9.84375*L**2*W**2*x0 + 9.84375*L**2*W**2*y0*sin(4*theta) -
118.125*L**2*x0*y0**2*cos(2*theta) + 118.125*L**2*x0*y0**2 +
16.875*L**2*x0*cos(2*theta) - 16.875*L**2*x0 + 78.75*L**2*y0**3*sin(2*theta) -
33.75*L**2*y0*sin(2*theta) + 1.4765625*W**4*x0*(1 - cos(2*theta))**2 +
5.90625*W**4*x0*cos(2*theta) - 5.90625*W**4*y0*sin(2*theta) -
2.953125*W**4*y0*sin(4*theta) + 118.125*W**2*x0*y0**2*cos(2*theta) +
118.125*W**2*x0*y0**2 - 16.875*W**2*x0*cos(2*theta) - 16.875*W**2*x0 -
78.75*W**2*y0**3*sin(2*theta) + 33.75*W**2*y0*sin(2*theta) + 472.5*x0*y0**4 -
405.0*x0*y0**2 + 40.5*x0)/16
 LM_(2,0) = L*W*(0.15625*L**2*cos(theta)**2 + 0.15625*W**2*sin(theta)**2 +
1.875*x0**2 - 0.625)
 LM_(2,1) = L*W*(L**2*(1.875*x0*sin(2*theta) + 0.9375*y0*cos(2*theta) + 0.9375*y0)
- 1.875*W**2*x0*sin(2*theta) + 1.875*W**2*y0*sin(theta)**2 + 22.5*x0**2*y0 -
7.5*y0)/4
 LM_(2,2) = L*W*(0.087890625*L**4*(1 - cos(4*theta)) + L**2*(0.5859375*W**2*(1 -
cos(2*theta))**2 + 1.171875*W**2*cos(2*theta) - 0.78125*W**2 -
2.34375*x0**2*cos(2*theta) + 2.34375*x0**2 + 9.375*x0*y0*sin(2*theta) +
2.34375*y0**2*cos(2*theta) + 2.34375*y0**2 - 1.5625) + 0.087890625*W**4*(1 -
cos(4*theta)) + 4.6875*W**2*x0**2*cos(theta)**2 - 9.375*W**2*x0*y0*sin(2*theta) +
4.6875*W**2*y0**2*sin(theta)**2 - 1.5625*W**2*sin(theta)**2 -
1.5625*W**2*cos(theta)**2 + 56.25*x0**2*y0**2 - 18.75*x0**2 - 18.75*y0**2 + 6.25)/4
 LM_(2,3) = L*W*(L**4*(13.125*x0*sin(theta) +
19.6875*y0*cos(theta))*sin(theta)**2*cos(theta) +
L**2*(5.46875*W**2*x0*sin(4*theta) + 16.40625*W**2*y0*(1 - cos(2*theta))**2 +
32.8125*W**2*y0*cos(2*theta) - 21.875*W**2*y0 - 65.625*x0**2*y0*cos(2*theta) +
```

```
65.625*x0**2*y0 + 131.25*x0*y0**2*sin(2*theta) - 26.25*x0*sin(2*theta) +
21.875*y0**3*cos(2*theta) + 21.875*y0**3 + 8.75*y0*cos(2*theta) - 35.0*y0) -
13.125*W**4*x0*sin(theta)*cos(theta)**3 + 2.4609375*W**4*y0*(1 - cos(4*theta)) +
131.25*W**2*x0**2*y0*cos(theta)**2 - 131.25*W**2*x0*y0**2*sin(2*theta) +
26.25*W**2*x0*sin(2*theta) + 43.75*W**2*y0**3*sin(theta)**2 -
26.25*W**2*y0*sin(theta)**2 - 43.75*W**2*y0*cos(theta)**2 + 525.0*x0**2*y0**3 -
315.0*x0**2*y0 - 175.0*y0**3 + 105.0*y0)/16
 LM_(2,4) = L*W*(2.63671875*L**6*sin(theta)**4*cos(theta)**2 +
L**4*(4.6142578125*W**2*(1 - cos(2*theta))**2 + 12.3046875*W**2*cos(2*theta) -
4.921875*W**2 - 7.3828125*x0**2*cos(2*theta) + 7.3828125*x0**2 +
59.0625*x0*y0*sin(2*theta) + 44.296875*y0**2*cos(2*theta) + 44.296875*y0**2 -
3.8671875*cos(2*theta) - 8.7890625)*sin(theta)**2 + L**2*(-2.30712890625*W**4*(1 -
cos(2*theta))**3 + 7.6904296875*W**4*(1 - cos(2*theta))**2 +
6.767578125*W**4*cos(2*theta) - 5.537109375*W**4 - 12.3046875*W**2*x0**2*(1 -
cos(2*theta))**2 - 24.609375*W**2*x0**2*cos(2*theta) + 24.609375*W**2*x0**2 +
49.21875*W**2*x0*y0*sin(4*theta) + 73.828125*W**2*y0**2*(1 - cos(2*theta))**2 +
147.65625*W**2*y0**2*cos(2*theta) - 98.4375*W**2*y0**2 - 6.4453125*W**2*(1 -
cos(2*theta))**2 - 12.890625*W**2*cos(2*theta) + 5.859375*W**2 -
295.3125*x0**2*y0**2*cos(2*theta) + 295.3125*x0**2*y0**2 +
42.1875*x0**2*cos(2*theta) - 42.1875*x0**2 + 393.75*x0*y0**3*sin(2*theta) -
168.75*x0*y0*sin(2*theta) + 49.21875*y0**4*cos(2*theta) + 49.21875*y0**4 +
56.25*y0*2*cos(2*theta) - 140.625*y0**2 - 9.84375*cos(2*theta) + 18.28125) +
2.63671875*W**6*sin(theta)**2*cos(theta)**4 + 14.765625*W**4*x0**2*cos(theta)**4 -
118.125*W**4*x0*y0*sin(theta)*cos(theta)**3 + 11.07421875*W**4*y0**2*(1 -
cos(4*theta)) - 1.58203125*W**4*(1 - cos(4*theta)) - 4.921875*W**4*cos(theta)**4 +
590.625*W**2*x0**2*y0**2*cos(theta)**2 - 84.375*W**2*x0**2*cos(theta)**2 -
393.75*W**2*x0*y0**3*sin(2*theta) + 168.75*W**2*x0*y0*sin(2*theta) +
98.4375*W**2*y0**4*sin(theta)**2 - 84.375*W**2*y0**2*sin(theta)**2 -
196.875*W**2*y0**2*cos(theta)**2 + 8.4375*W**2*sin(theta)**2 +
28.125*W**2*cos(theta)**2 + 1181.25*x0**2*y0**4 - 1012.5*x0**2*y0**2 + 101.25*x0**2
- 393.75*y0**4 + 337.5*y0**2 - 33.75)/16
 LM_(3,0) = L*W*x0*(1.09375*L**2*cos(theta)**2 + 1.09375*W**2*sin(theta)**2 +
4.375*x0**2 - 2.625)
 LM_(3,1) = L*W*(0.1640625*L**4*sin(2*theta) + 0.08203125*L**4*sin(4*theta) -
0.2734375*L**2*W**2*sin(4*theta) + 6.5625*L**2*x0**2*sin(2*theta) +
6.5625*L**2*x0*y0*cos(2*theta) + 6.5625*L**2*x0*y0 - 1.3125*L**2*sin(2*theta) -
0.1640625*W**4*sin(2*theta) + 0.08203125*W**4*sin(4*theta) -
6.5625*W**2*x0**2*sin(2*theta) - 6.5625*W**2*x0*y0*cos(2*theta) + 6.5625*W**2*x0*y0
+ 1.3125*W**2*sin(2*theta) + 52.5*x0**3*y0 - 31.5*x0*y0)/4
 LM_(3,2) = L*W*(L**4*(19.6875*x0*sin(theta) +
13.125*y0*cos(theta))*sin(theta)*cos(theta)**2 + L**2*(16.40625*W**2*x0*(1 -
cos(2*theta))**2 + 32.8125*W**2*x0*cos(2*theta) - 21.875*W**2*x0 -
5.46875*W**2*y0*sin(4*theta) - 21.875*x0**3*cos(2*theta) + 21.875*x0**3 +
131.25*x0**2*y0*sin(2*theta) + 65.625*x0*y0**2*cos(2*theta) + 65.625*x0*y0**2 -
8.75*x0*cos(2*theta) - 35.0*x0 - 26.25*y0*sin(2*theta)) + 2.4609375*W**4*x0*(1 -
cos(4*theta)) - 13.125*W**4*y0*sin(theta)**3*cos(theta) +
43.75*W**2*x0**3*cos(theta)**2 - 131.25*W**2*x0**2*y0*sin(2*theta) +
131.25*W**2*x0*y0**2*sin(theta)**2 - 43.75*W**2*x0*sin(theta)**2 -
26.25*W**2*x0*cos(theta)**2 + 26.25*W**2*y0*sin(2*theta) + 525.0*x0**3*y0**2 -
175.0*x0**3 - 315.0*x0*y0**2 + 105.0*x0)/16
```

```
 LM_(3,3) = L*W*(2.734375*L**6*sin(theta)**3*cos(theta)**3 +
L**4*(4.78515625*W**2*(1 - cos(2*theta))**2 + 9.5703125*W**2*cos(2*theta) -
5.7421875*W**2 - 22.96875*x0**2*cos(2*theta) + 22.96875*x0**2 +
68.90625*x0*y0*sin(2*theta) + 22.96875*y0**2*cos(2*theta) + 22.96875*y0**2 -
9.1875)*sin(theta)*cos(theta) + L**2*(-0.95703125*W**4*(1 -
cos(2*theta))**2*sin(2*theta) + 1.07666015625*W**4*sin(2*theta) -
0.95703125*W**4*sin(4*theta) - 0.35888671875*W**4*sin(6*theta) +
19.140625*W**2*x0**2*sin(4*theta) + 114.84375*W**2*x0*y0*(1 - cos(2*theta))**2 +
229.6875*W**2*x0*y0*cos(2*theta) - 153.125*W**2*x0*y0 -
19.140625*W**2*y0**2*sin(4*theta) - 153.125*x0**3*y0*cos(2*theta) +
153.125*x0**3*y0 + 459.375*x0**2*y0**2*sin(2*theta) - 91.875*x0**2*sin(2*theta) +
153.125*x0*y0**3*cos(2*theta) + 153.125*x0*y0**3 - 183.75*x0*y0 -
91.875*y0**2*sin(2*theta) + 18.375*sin(2*theta)) -
2.734375*W**6*sin(theta)**3*cos(theta)**3 -
45.9375*W**4*x0**2*sin(theta)*cos(theta)**3 + 17.2265625*W**4*x0*y0*(1 -
cos(4*theta)) - 45.9375*W**4*y0**2*sin(theta)**3*cos(theta) +
9.1875*W**4*sin(theta)**3*cos(theta) + 9.1875*W**4*sin(theta)*cos(theta)**3 +
306.25*W**2*x0**3*y0*cos(theta)**2 - 459.375*W**2*x0**2*y0**2*sin(2*theta) +
91.875*W**2*x0**2*sin(2*theta) + 306.25*W**2*x0*y0**3*sin(theta)**2 -
183.75*W**2*x0*y0*sin(theta)**2 - 183.75*W**2*x0*y0*cos(theta)**2 +
91.875*W**2*y0**2*sin(2*theta) - 18.375*W**2*sin(2*theta) + 1225.0*x0**3*y0**3 -
735.0*x0**3*y0 - 735.0*x0*y0**3 + 441.0*x0*y0)/16
 LM_(3,4) = L*W*(L**6*(73.828125*x0*sin(theta) +
98.4375*y0*cos(theta))*sin(theta)**3*cos(theta)**2 +
L**4*(516.796875*W**2*x0*sin(theta)**5 - 689.0625*W**2*x0*sin(theta)**3 +
206.71875*W**2*x0*sin(theta) + 137.8125*W**2*y0*sin(theta)**4*cos(theta) +
551.25*W**2*y0*cos(theta)**5 - 413.4375*W**2*y0*cos(theta)**3 +
137.8125*x0**3*sin(theta)**3 - 1653.75*x0**2*y0*cos(theta)**3 +
1653.75*x0**2*y0*cos(theta) - 2480.625*x0*y0**2*sin(theta)**3 +
2480.625*x0*y0**2*sin(theta) + 271.6875*x0*sin(theta)**3 - 354.375*x0*sin(theta) +
551.25*y0**3*cos(theta)**3 + 94.5*y0*cos(theta)**3 -
330.75*y0*cos(theta))*sin(theta) + L**2*(-64.599609375*W**4*x0*(1 -
cos(2*theta))**3 + 215.33203125*W**4*x0*(1 - cos(2*theta))**2 +
189.4921875*W**4*x0*cos(2*theta) - 155.0390625*W**4*x0 - 34.453125*W**4*y0*(1 -
cos(2*theta))**2*sin(2*theta) + 38.759765625*W**4*y0*sin(2*theta) -
34.453125*W**4*y0*sin(4*theta) - 12.919921875*W**4*y0*sin(6*theta) -
114.84375*W**2*x0**3*(1 - cos(2*theta))**2 - 229.6875*W**2*x0**3*cos(2*theta) +
229.6875*W**2*x0**3 + 689.0625*W**2*x0**2*y0*sin(4*theta) +
2067.1875*W**2*x0*y0**2*(1 - cos(2*theta))**2 + 4134.375*W**2*x0*y0**2*cos(2*theta)
- 2756.25*W**2*x0*y0**2 - 226.40625*W**2*x0*(1 - cos(2*theta))**2 -
452.8125*W**2*x0*cos(2*theta) + 255.9375*W**2*x0 - 229.6875*W**2*y0**3*sin(4*theta)
- 39.375*W**2*y0*sin(4*theta) - 2756.25*x0**3*y0**2*cos(2*theta) +
2756.25*x0**3*y0**2 + 393.75*x0**3*cos(2*theta) - 393.75*x0**3 +
5512.5*x0**2*y0**3*sin(2*theta) - 2362.5*x0**2*y0*sin(2*theta) +
1378.125*x0*y0**4*cos(2*theta) + 1378.125*x0*y0**4 + 472.5*x0*y0**2*cos(2*theta) -
2835.0*x0*y0**2 - 118.125*x0*cos(2*theta) + 354.375*x0 - 1102.5*y0**3*sin(2*theta)
+ 472.5*y0*sin(2*theta)) + 73.828125*W**6*x0*sin(theta)**2*cos(theta)**4 -
98.4375*W**6*y0*sin(theta)**3*cos(theta)**3 + 137.8125*W**4*x0**3*cos(theta)**4 -
1653.75*W**4*x0**2*y0*sin(theta)*cos(theta)**3 + 310.078125*W**4*x0*y0**2*(1 -
cos(4*theta)) - 44.296875*W**4*x0*(1 - cos(4*theta)) -
```

```
82.6875*W**4*x0*cos(theta)**4 - 551.25*W**4*y0**3*sin(theta)**3*cos(theta) +
236.25*W**4*y0*sin(theta)**3*cos(theta) + 330.75*W**4*y0*sin(theta)*cos(theta)**3 +
5512.5*W**2*x0**3*y0**2*cos(theta)**2 - 787.5*W**2*x0**3*cos(theta)**2 -
5512.5*W**2*x0**2*y0**3*sin(2*theta) + 2362.5*W**2*x0**2*y0*sin(2*theta) +
2756.25*W**2*x0*y0**4*sin(theta)**2 - 2362.5*W**2*x0*y0**2*sin(theta)**2 -
3307.5*W**2*x0*y0**2*cos(theta)**2 + 236.25*W**2*x0*sin(theta)**2 +
472.5*W**2*x0*cos(theta)**2 + 1102.5*W**2*y0**3*sin(2*theta) -
472.5*W**2*y0*sin(2*theta) + 11025.0*x0**3*y0**4 - 9450.0*x0**3*y0**2 + 945.0*x0**3
- 6615.0*x0*y0**4 + 5670.0*x0*y0**2 - 567.0*x0)/64
 LM_(4,0) = L*W*(0.4921875*L**4*cos(theta)**4 + L**2*(1.640625*W**2*sin(theta)**2 +
19.6875*x0**2 - 2.8125)*cos(theta)**2 + 0.4921875*W**4*sin(theta)**4 +
19.6875*W**2*x0**2*sin(theta)**2 - 2.8125*W**2*sin(theta)**2 + 39.375*x0**4 -
33.75*x0**2 + 3.375)/4
 LM_(4,1) = L*W*(5.90625*L**4*x0*sin(2*theta) + 2.953125*L**4*x0*sin(4*theta) +
1.4765625*L**4*y0*(1 - cos(2*theta))**2 + 5.90625*L**4*y0*cos(2*theta) -
9.84375*L**2*W**2*x0*sin(4*theta) - 4.921875*L**2*W**2*y0*(1 - cos(2*theta))**2 -
9.84375*L**2*W**2*y0*cos(2*theta) + 9.84375*L**2*W**2*y0 +
78.75*L**2*x0**3*sin(2*theta) + 118.125*L**2*x0**2*y0*cos(2*theta) +
118.125*L**2*x0**2*y0 - 33.75*L**2*x0*sin(2*theta) - 16.875*L**2*y0*cos(2*theta) -
16.875*L**2*y0 - 5.90625*W**4*x0*sin(2*theta) + 2.953125*W**4*x0*sin(4*theta) +
1.4765625*W**4*y0*(1 - cos(2*theta))**2 - 78.75*W**2*x0**3*sin(2*theta) -
118.125*W**2*x0**2*y0*cos(2*theta) + 118.125*W**2*x0**2*y0 +
33.75*W**2*x0*sin(2*theta) + 16.875*W**2*y0*cos(2*theta) - 16.875*W**2*y0 +
472.5*x0**4*y0 - 405.0*x0**2*y0 + 40.5*y0)/16
 LM_(4,2) = L*W*(2.63671875*L**6*sin(theta)**2*cos(theta)**4 +
L**4*(4.6142578125*W**2*(1 - cos(2*theta))**2 + 6.15234375*W**2*cos(2*theta) -
4.921875*W**2 - 44.296875*x0**2*cos(2*theta) + 44.296875*x0**2 +
59.0625*x0*y0*sin(2*theta) + 7.3828125*y0**2*cos(2*theta) + 7.3828125*y0**2 +
3.8671875*cos(2*theta) - 8.7890625)*cos(theta)**2 + L**2*(2.30712890625*W**4*(1 -
cos(2*theta))**3 - 6.15234375*W**4*(1 - cos(2*theta))**2 -
3.69140625*W**4*cos(2*theta) + 3.69140625*W**4 + 73.828125*W**2*x0**2*(1 -
cos(2*theta))**2 + 147.65625*W**2*x0**2*cos(2*theta) - 98.4375*W**2*x0**2 -
49.21875*W**2*x0*y0*sin(4*theta) - 12.3046875*W**2*y0**2*(1 - cos(2*theta))**2 -
24.609375*W**2*y0**2*cos(2*theta) + 24.609375*W**2*y0**2 - 6.4453125*W**2*(1 -
cos(2*theta))**2 - 12.890625*W**2*cos(2*theta) + 5.859375*W**2 -
49.21875*x0**4*cos(2*theta) + 49.21875*x0**4 + 393.75*x0**3*y0*sin(2*theta) +
295.3125*x0**2*y0**2*cos(2*theta) + 295.3125*x0**2*y0**2 - 56.25*x0**2*cos(2*theta)
- 140.625*x0**2 - 168.75*x0*y0*sin(2*theta) - 42.1875*y0**2*cos(2*theta) -
42.1875*y0**2 + 9.84375*cos(2*theta) + 18.28125) +
2.63671875*W**6*sin(theta)**4*cos(theta)**2 + 11.07421875*W**4*x0**2*(1 -
cos(4*theta)) - 118.125*W**4*x0*y0*sin(theta)**3*cos(theta) +
14.765625*W**4*y0**2*sin(theta)**4 - 1.58203125*W**4*(1 - cos(4*theta)) -
4.921875*W**4*sin(theta)**4 + 98.4375*W**2*x0**4*cos(theta)**2 -
393.75*W**2*x0**3*y0*sin(2*theta) + 590.625*W**2*x0**2*y0**2*sin(theta)**2 -
196.875*W**2*x0**2*sin(theta)**2 - 84.375*W**2*x0**2*cos(theta)**2 +
168.75*W**2*x0*y0*sin(2*theta) - 84.375*W**2*y0**2*sin(theta)**2 +
28.125*W**2*sin(theta)**2 + 8.4375*W**2*cos(theta)**2 + 1181.25*x0**4*y0**2 -
393.75*x0**4 - 1012.5*x0**2*y0**2 + 337.5*x0**2 + 101.25*y0**2 - 33.75)/16
 LM_(4,3) = L*W*(L**6*(98.4375*x0*sin(theta) +
73.828125*y0*cos(theta))*sin(theta)**2*cos(theta)**3 +
```

```
L**4*(689.0625*W**2*x0*sin(theta)**5 - 689.0625*W**2*x0*sin(theta)**3 +
137.8125*W**2*x0*sin(theta) + 206.71875*W**2*y0*sin(theta)**4*cos(theta) +
310.078125*W**2*y0*cos(theta)**5 - 275.625*W**2*y0*cos(theta)**3 +
551.25*x0**3*sin(theta)**3 - 2480.625*x0**2*y0*cos(theta)**3 +
2480.625*x0**2*y0*cos(theta) - 1653.75*x0*y0**2*sin(theta)**3 +
1653.75*x0*y0**2*sin(theta) + 94.5*x0*sin(theta)**3 - 330.75*x0*sin(theta) +
137.8125*y0**3*cos(theta)**3 + 271.6875*y0*cos(theta)**3 -
354.375*y0*cos(theta))*cos(theta) + L**2*(-34.453125*W**4*x0*(1 -
cos(2*theta))**2*sin(2*theta) + 38.759765625*W**4*x0*sin(2*theta) -
34.453125*W**4*x0*sin(4*theta) - 12.919921875*W**4*x0*sin(6*theta) +
64.599609375*W**4*y0*(1 - cos(2*theta))**3 - 172.265625*W**4*y0*(1 -
cos(2*theta))**2 - 103.359375*W**4*y0*cos(2*theta) + 103.359375*W**4*y0 +
229.6875*W**2*x0**3*sin(4*theta) + 2067.1875*W**2*x0**2*y0*(1 - cos(2*theta))**2 +
4134.375*W**2*x0**2*y0*cos(2*theta) - 2756.25*W**2*x0**2*y0 -
689.0625*W**2*x0*y0**2*sin(4*theta) + 39.375*W**2*x0*sin(4*theta) -
114.84375*W**2*y0**3*(1 - cos(2*theta))**2 - 229.6875*W**2*y0**3*cos(2*theta) +
229.6875*W**2*y0**3 - 226.40625*W**2*y0*(1 - cos(2*theta))**2 -
452.8125*W**2*y0*cos(2*theta) + 255.9375*W**2*y0 - 1378.125*x0**4*y0*cos(2*theta) +
1378.125*x0**4*y0 + 5512.5*x0**3*y0**2*sin(2*theta) - 1102.5*x0**3*sin(2*theta) +
2756.25*x0**2*y0**3*cos(2*theta) + 2756.25*x0**2*y0**3 -
472.5*x0**2*y0*cos(2*theta) - 2835.0*x0**2*y0 - 2362.5*x0*y0**2*sin(2*theta) +
472.5*x0*sin(2*theta) - 393.75*y0**3*cos(2*theta) - 393.75*y0**3 +
118.125*y0*cos(2*theta) + 354.375*y0) - 98.4375*W**6*x0*sin(theta)**3*cos(theta)**3
+ 73.828125*W**6*y0*sin(theta)**4*cos(theta)**2 -
551.25*W**4*x0**3*sin(theta)*cos(theta)**3 + 310.078125*W**4*x0**2*y0*(1 -
cos(4*theta)) - 1653.75*W**4*x0*y0**2*sin(theta)**3*cos(theta) +
330.75*W**4*x0*sin(theta)**3*cos(theta) + 236.25*W**4*x0*sin(theta)*cos(theta)**3 +
137.8125*W**4*y0**3*sin(theta)**4 - 44.296875*W**4*y0*(1 - cos(4*theta)) -
82.6875*W**4*y0*sin(theta)**4 + 2756.25*W**2*x0**4*y0*cos(theta)**2 -
5512.5*W**2*x0**3*y0**2*sin(2*theta) + 1102.5*W**2*x0**3*sin(2*theta) +
5512.5*W**2*x0**2*y0**3*sin(theta)**2 - 3307.5*W**2*x0**2*y0*sin(theta)**2 -
2362.5*W**2*x0**2*y0*cos(theta)**2 + 2362.5*W**2*x0*y0**2*sin(2*theta) -
472.5*W**2*x0*sin(2*theta) - 787.5*W**2*y0**3*sin(theta)**2 +
472.5*W**2*y0*sin(theta)**2 + 236.25*W**2*y0*cos(theta)**2 + 11025.0*x0**4*y0**3 -
6615.0*x0**4*y0 - 9450.0*x0**2*y0**3 + 5670.0*x0**2*y0 + 945.0*y0**3 - 567.0*y0)/64
 LM_(4,4) = L*W*(0.0105142593383789*L**8*cos(2*theta)**4 -
0.0210285186767578*L**8*cos(2*theta)**2 + 0.0105142593383789*L**8 -
0.126171112060547*L**6*W**2*cos(2*theta)**4 +
0.144195556640625*L**6*W**2*cos(2*theta)**2 - 0.0180244445800781*L**6*W**2 +
0.648880004882813*L**6*x0**2*cos(2*theta)**3 -
0.648880004882813*L**6*x0**2*cos(2*theta)**2 -
0.648880004882813*L**6*x0**2*cos(2*theta) + 0.648880004882813*L**6*x0**2 +
1.29776000976563*L**6*x0*y0*sin(2*theta) -
0.432586669921875*L**6*x0*y0*sin(6*theta) -
0.648880004882813*L**6*y0**2*cos(2*theta)**3 -
0.648880004882813*L**6*y0**2*cos(2*theta)**2 +
0.648880004882813*L**6*y0**2*cos(2*theta) + 0.648880004882813*L**6*y0**2 +
0.185394287109375*L**6*cos(2*theta)**2 - 0.185394287109375*L**6 +
0.264959335327148*L**4*W**4*cos(2*theta)**4 -
0.227108001708984*L**4*W**4*cos(2*theta)**2 + 0.0227108001708984*L**4*W**4 -
```

```
4.54216003417969*L**4*W**2*x0**2*cos(2*theta)**3 +
1.51405334472656*L**4*W**2*x0**2*cos(2*theta)**2 +
3.33091735839844*L**4*W**2*x0**2*cos(2*theta) - 0.302810668945313*L**4*W**2*x0**2 +
4.844970703125*L**4*W**2*x0*y0*sin(2*theta)*cos(2*theta)**2 -
9.68994140625*L**4*W**2*x0*y0*sin(2*theta)*cos(2*theta) -
0.605621337890625*L**4*W**2*x0*y0*sin(2*theta) +
4.844970703125*L**4*W**2*x0*y0*sin(4*theta) +
1.81686401367188*L**4*W**2*x0*y0*sin(6*theta) +
4.54216003417969*L**4*W**2*y0**2*cos(2*theta)**3 +
1.51405334472657*L**4*W**2*y0**2*cos(2*theta)**2 -
3.33091735839844*L**4*W**2*y0**2*cos(2*theta) - 0.302810668945307*L**4*W**2*y0**2 -
0.432586669921875*L**4*W**2*cos(2*theta)**2 -
1.11022302462516e-16*L**4*W**2*cos(2*theta) + 0.0865173339843751*L**4*W**2 +
1.21124267578125*L**4*x0**4*cos(2*theta)**2 -
2.4224853515625*L**4*x0**4*cos(2*theta) + 1.21124267578125*L**4*x0**4 +
19.3798828125*L**4*x0**3*y0*sin(2*theta) - 9.68994140625*L**4*x0**3*y0*sin(4*theta)
- 43.604736328125*L**4*x0**2*y0**2*cos(2*theta)**2 +
43.604736328125*L**4*x0**2*y0**2 + 5.1910400390625*L**4*x0**2*cos(2*theta)**2 +
2.076416015625*L**4*x0**2*cos(2*theta) - 7.2674560546875*L**4*x0**2 +
19.3798828125*L**4*x0*y0**3*sin(2*theta) + 9.68994140625*L**4*x0*y0**3*sin(4*theta)
- 16.611328125*L**4*x0*y0*sin(2*theta) +
1.21124267578125*L**4*y0**4*cos(2*theta)**2 +
2.4224853515625*L**4*y0**4*cos(2*theta) + 1.21124267578125*L**4*y0**4 +
5.1910400390625*L**4*y0**2*cos(2*theta)**2 - 2.076416015625*L**4*y0**2*cos(2*theta)
- 7.2674560546875*L**4*y0**2 - 0.6822509765625*L**4*cos(2*theta)**2 +
1.0975341796875*L**4 - 0.126171112060547*L**2*W**6*cos(2*theta)**4 +
0.144195556640625*L**2*W**6*cos(2*theta)**2 - 0.0180244445800781*L**2*W**6 +
4.54216003417969*L**2*W**4*x0**2*cos(2*theta)**3 +
1.51405334472656*L**2*W**4*x0**2*cos(2*theta)**2 -
3.33091735839844*L**2*W**4*x0**2*cos(2*theta) - 0.302810668945313*L**2*W**4*x0**2 -
4.844970703125*L**2*W**4*x0*y0*sin(2*theta)*cos(2*theta)**2 +
9.68994140625*L**2*W**4*x0*y0*sin(2*theta)*cos(2*theta) +
0.605621337890625*L**2*W**4*x0*y0*sin(2*theta) -
4.844970703125*L**2*W**4*x0*y0*sin(4*theta) -
1.81686401367188*L**2*W**4*x0*y0*sin(6*theta) -
4.54216003417969*L**2*W**4*y0**2*cos(2*theta)**3 +
1.51405334472656*L**2*W**4*y0**2*cos(2*theta)**2 +
3.33091735839844*L**2*W**4*y0**2*cos(2*theta) - 0.302810668945313*L**2*W**4*y0**2 -
0.432586669921875*L**2*W**4*cos(2*theta)**2 + 0.0865173339843751*L**2*W**4 -
4.0374755859375*L**2*W**2*x0**4*cos(2*theta)**2 + 4.0374755859375*L**2*W**2*x0**4 +
32.2998046875*L**2*W**2*x0**3*y0*sin(4*theta) +
145.34912109375*L**2*W**2*x0**2*y0**2*cos(2*theta)**2 -
48.44970703125*L**2*W**2*x0**2*y0**2 -
17.303466796875*L**2*W**2*x0**2*cos(2*theta)**2 + 3.460693359375*L**2*W**2*x0**2 -
32.2998046875*L**2*W**2*x0*y0**3*sin(4*theta) -
4.0374755859375*L**2*W**2*y0**4*cos(2*theta)**2 + 4.0374755859375*L**2*W**2*y0**4 -
17.303466796875*L**2*W**2*y0**2*cos(2*theta)**2 + 3.460693359375*L**2*W**2*y0**2 +
2.274169921875*L**2*W**2*cos(2*theta)**2 - 0.296630859375*L**2*W**2 -
96.8994140625*L**2*x0**4*y0**2*cos(2*theta) + 96.8994140625*L**2*x0**4*y0**2 +
13.8427734375*L**2*x0**4*cos(2*theta) - 13.8427734375*L**2*x0**4 +
```

```
258.3984375*L**2*x0**3*y0**3*sin(2*theta) - 110.7421875*L**2*x0**3*y0*sin(2*theta)
+ 96.8994140625*L**2*x0**2*y0**4*cos(2*theta) + 96.8994140625*L**2*x0**2*y0**4 -
166.11328125*L**2*x0**2*y0**2 - 3.5595703125*L**2*x0**2*cos(2*theta) +
20.1708984375*L**2*x0**2 - 110.7421875*L**2*x0*y0**3*sin(2*theta) +
47.4609375*L**2*x0*y0*sin(2*theta) - 13.8427734375*L**2*y0**4*cos(2*theta) -
13.8427734375*L**2*y0**4 + 3.5595703125*L**2*y0**2*cos(2*theta) +
20.1708984375*L**2*y0**2 - 2.373046875*L**2 +
0.0105142593383789*W**8*cos(2*theta)**4 - 0.0210285186767578*W**8*cos(2*theta)**2 +
0.0105142593383789*W**8 - 0.648880004882813*W**6*x0**2*cos(2*theta)**3 -
0.648880004882813*W**6*x0**2*cos(2*theta)**2 +
0.648880004882813*W**6*x0**2*cos(2*theta) + 0.648880004882813*W**6*x0**2 -
1.29776000976563*W**6*x0*y0*sin(2*theta) +
0.432586669921875*W**6*x0*y0*sin(6*theta) +
0.648880004882813*W**6*y0**2*cos(2*theta)**3 -
0.648880004882813*W**6*y0**2*cos(2*theta)**2 -
0.648880004882813*W**6*y0**2*cos(2*theta) + 0.648880004882813*W**6*y0**2 +
0.185394287109375*W**6*cos(2*theta)**2 - 0.185394287109375*W**6 +
1.21124267578125*W**4*x0**4*cos(2*theta)**2 +
2.4224853515625*W**4*x0**4*cos(2*theta) + 1.21124267578125*W**4*x0**4 -
19.3798828125*W**4*x0**3*y0*sin(2*theta) - 9.68994140625*W**4*x0**3*y0*sin(4*theta)
- 43.604736328125*W**4*x0**2*y0**2*cos(2*theta)**2 +
43.604736328125*W**4*x0**2*y0**2 + 5.1910400390625*W**4*x0**2*cos(2*theta)**2 -
2.076416015625*W**4*x0**2*cos(2*theta) - 7.2674560546875*W**4*x0**2 -
19.3798828125*W**4*x0*y0**3*sin(2*theta) + 9.68994140625*W**4*x0*y0**3*sin(4*theta)
+ 16.611328125*W**4*x0*y0*sin(2*theta) +
1.21124267578125*W**4*y0**4*cos(2*theta)**2 -
2.4224853515625*W**4*y0**4*cos(2*theta) + 1.21124267578125*W**4*y0**4 +
5.1910400390625*W**4*y0**2*cos(2*theta)**2 + 2.076416015625*W**4*y0**2*cos(2*theta)
- 7.2674560546875*W**4*y0**2 - 0.6822509765625*W**4*cos(2*theta)**2 +
1.0975341796875*W**4 + 96.8994140625*W**2*x0**4*y0**2*cos(2*theta) +
96.8994140625*W**2*x0**4*y0**2 - 13.8427734375*W**2*x0**4*cos(2*theta) -
13.8427734375*W**2*x0**4 - 258.3984375*W**2*x0**3*y0**3*sin(2*theta) +
110.7421875*W**2*x0**3*y0*sin(2*theta) -
96.8994140625*W**2*x0**2*y0**4*cos(2*theta) + 96.8994140625*W**2*x0**2*y0**4 -
166.11328125*W**2*x0**2*y0**2 + 3.5595703125*W**2*x0**2*cos(2*theta) +
20.1708984375*W**2*x0**2 + 110.7421875*W**2*x0*y0**3*sin(2*theta) -
47.4609375*W**2*x0*y0*sin(2*theta) + 13.8427734375*W**2*y0**4*cos(2*theta) -
13.8427734375*W**2*y0**4 - 3.5595703125*W**2*y0**2*cos(2*theta) +
20.1708984375*W**2*y0**2 - 2.373046875*W**2 + 387.59765625*x0**4*y0**4 -
332.2265625*x0**4*y0**2 + 33.22265625*x0**4 - 332.2265625*x0**2*y0**4 +
284.765625*x0**2*y0**2 - 28.4765625*x0**2 + 33.22265625*y0**4 - 28.4765625*y0**2 +
2.84765625)
```

REFERENCES

[1] Home | Official LEGO® Shop NL. URL https://www.lego.com/en-nl.

[2] Pioneering bionic 3D printing - Company - Airbus. URL https://www.airbus.com/newsroom/news/en/2016/03/Pioneering-bionic-3D-printing.html.

[3] Generative Design at Airbus | Customer Stories | Autodesk. URL https://www.autodesk.com/customer-stories/airbus.

[4] Boeing: Historical Snapshot: 787 Commercial Transport. URL http://www.boeing.com/history/products/787.page.

[5] Airbus Continues to Innovate Bionic Design for Future Sustainable Flights. URL https://www.autodesk.com/redshift/bionic-design/.

[6] Company profile: An introduction to The LEGO Group 2010. Technical report, The LEGO Group, 2010. URL https://issuu.com/headlenio/docs/download98e142631e71927fdd52304c1c0.

[7] What COVID-19 did to European Aviation in 2020, and Outlook 2021. Technical report, EUROCONTROL, 1 2021. URL https://www.eurocontrol.int/publication/what-covid19-did-european-aviation-2020-outlook-2021.

[8] Niels Aage, Erik Andreassen, and Boyan Stefanov Lazarov. Topology optimization using PETSc: An easy-to-use, fully parallel, open source topology optimization framework. *Structural and Multidisciplinary Optimization*, 51(3):565–572, 3 2015. doi: 10.1007/s00158-014-1157-0.

[9] Yaser S. Abu-Mostafa and Demetri Psaltis. Recognitive Aspects of Moment Invariants. *IEEE Transactions on Pattern Analysis and Machine Intelligence*, PAMI-6(6): 698–706, 11 1984. doi: 10.1109/TPAMI.1984.4767594.

[10] Wolfgang Achtziger and W Achtziger. On simultaneous optimization of truss geometry and topology. 33:285–304, 2007. doi: 10.1007/s00158-006-0092-0.

[11] Oswin Aichholzer Franz Aurenhammer and David G Alberts Bernd. A Novel Type of Skeleton for Polygons. *Journal of Universal Computer Science*, 1(12):752–761, 1995.

[12] Luigi Ambrosio and Giuseppe Buttazzo. An optimal design problem with perimeter penalization. *Calculus of Variations and Partial Differential Equations*, 1(1): 55–69, 3 1993. ISSN 09442669. doi: 10.1007/BF02163264.

[13] Panayotis Apostolopoulos and Christos Kassapoglou. Recurring Cost Minimization of Composite Laminated Structures-Optimum Part Size as a Function of Learning Curve Effects and Assembly. *Journal of COMPOSITE MATERIALS*, 36(04), 2002. doi: 10.1106/002199802023556.

[14] Alireza Asadpoure, James K Guest, Lorenzo Valdevit, A Asadpoure, and J K Guest. Incorporating fabrication cost into topology optimization of discrete structures and lattices. *Structural and Multidisciplinary Optimization*, 51:385–396, 2015. doi: 10.1007/s00158-014-1133-8.

[15] B. Barroqueiro, A. Andrade-Campos, R. A. F. Valente, and V. Neto. Metal Additive Manufacturing Cycle in Aerospace Industry: A Comprehensive Review. *Journal of Manufacturing and Materials Processing*, 3(3):52, 6 2019. ISSN 2504-4494. doi: 10.3390/jmmp3030052. URL https://www.mdpi.com/2504-4494/3/3/52.

[16] Stefan Behnel, Robert Bradshaw, Craig Citro, Lisandro Dalcin, Dag Sverre Seljebotn, and Kurt Smith. Cython: The Best of Both Worlds. *Computing in Science & Engineering*, 13(02):31–39, 3 2011. ISSN 1521-9615. doi: 10.1109/MCSE.2010.118.

[17] M. P. Bendøse and O. Sigmund. *Topology Optimization - Theory, Methods and Applications*. Springer, 2 edition, 2003. ISBN 978-3-540-42992-0.

[18] M. P. Bendsøe. Optimal shape design as a material distribution problem. *Structural Optimization*, 1(4):193–202, 12 1989. ISSN 09344373. doi: 10.1007/BF01650949.

[19] M. P. Bendsøe and O. Sigmund. Material interpolation schemes in topology optimization. *Archive of Applied Mechanics*, 69(9-10):635–654, 1999. doi: 10.1007/s004190050248.

[20] Martin P. Bendsoe, Niels Olhoff, and John E. Taylor. A Variational Formulation for Multicriteria Structural Optimization. *Journal of Structural Mechanics*, 11(4):523–544, 1983. doi: 10.1080/03601218308907456.

[21] Martin Philip Bendsøe and Noboru Kikuchi. Generating optimal topologies in structural design using a homogenization method. *Computer Methods in Applied Mechanics and Engineering*, 71(2):197–224, 11 1988. doi: 10.1016/0045-7825(88)90086-2.

[22] MP BendsOe and A Ben-Tal. Optimization methods for truss geometry and topology design. Technical report, 1994.

[23] Alain. Bensoussan, J.-L. (Jacques-Louis) Lions, and George Papanicolaou. *Asymptotic analysis for periodic structures*. North-Holland Pub. Co., 1978. ISBN 0444851720.

[24] L V Berlyand and S M Koz˜ov. Asymptotics of the Homogenized Moduli for the Elastic Chess-Board Composite. Technical report, 1992.

[25] T. Borrvall. Topology optimization of elastic continua using restriction. *Archives of Computational Methods in Engineering*, 8(4):351–385, 12 2001. ISSN 1134-3060. doi: 10.1007/bf02743737.

[26] Blaise Bourdin. Filters in topology optimization. *International Journal for Numerical Methods in Engineering*, 50(9):2143–2158, 3 2001. ISSN 00295981. doi: 10.1002/nme.116. URL http://doi.wiley.com/10.1002/nme.116.

[27] Matteo Bruggi. On an alternative approach to stress constraints relaxation in topology optimization. *Structural and Multidisciplinary Optimization*, 36(2):125–141, 8 2008. ISSN 1615147X. doi: 10.1007/s00158-007-0203-6.

[28] T. E. Bruns. A reevaluation of the SIMP method with filtering and an alternative formulation for solid-void topology optimization. *Structural and Multidisciplinary Optimization*, 30(6):428–436, 12 2005. doi: 10.1007/s00158-005-0537-x.

[29] Tyler E. Bruns and Daniel A. Tortorelli. Topology optimization of non-linear elastic structures and compliant mechanisms. *Computer Methods in Applied Mechanics and Engineering*, 190(26-27):3443–3459, 3 2001. doi: 10.1016/S0045-7825(00)00278-4.

[30] T. Buhl, C. B.W. Pedersen, and O. Sigmund. Stiffness design of geometrically nonlinear structures using topology optimization. *Structural and Multidisciplinary Optimization*, 19(2):93–104, 4 2000. ISSN 1615147X. doi: 10.1007/s001580050089.

[31] José A. Ceroni. Economic Rationalization of Automation Projects. In *Springer Handbook of Automation*, pages 699–713. Springer Berlin Heidelberg, 2009. doi: 10.1007/978-3-540-78831-7{_}40.

[32] G. D. Cheng and X. Guo. ϵ-relaxed approach in structural topology optimization. *Structural Optimization*, 13(4):258–266, 1997. ISSN 09344373. doi: 10.1007/BF01197454.

[33] Amy Chiang and Simon Liao. Image Analysis with Legendre Moment Descriptors. *Journal of Computer Science*, 11(1):127–136, 9 2014. ISSN 1552-6607. doi: 10.3844/JCSSP.2015.127.136. URL https://thescipub.com/abstract/jcssp.2015.127.136.

[34] Yu Hsin Chou and Chyi Yeu Lin. Improved image interpreting and modeling technique for automated structural optimization system. *Structural and Multidisciplinary Optimization*, 40(1-6):215–226, 1 2010. doi: 10.1007/s00158-008-0352-2.

[35] A Diaz. Checkerboard patterns in layout optimization. Technical report, 1995.

[36] Michael W. Dobbs and Lewis P. Felton. Optimization of Truss Geometry. *Journal of the Structural Division*, 95(10):2105–2118, 10 1969. doi: 10.1061/JSDEAG.0002374. URL https://ascelibrary.org/doi/abs/10.1061/JSDEAG.0002374.

[37] W. Dorn, R. Gomory, and H. J. Greenberg. Automatic design of optimal structures. *Journal de Mecanique*, 3:25–52, 1964.

[38] Yixian Du, Shuangqiao Yan, Yan Zhang, Huanghai Xie, and Qihua Tian. A modified interpolation approach for topology optimization. *Acta Mechanica Solida Sinica*, 28(4):420–430, 8 2015. doi: 10.1016/S0894-9166(15)30027-6.

B

[39] Maria B. Dühring, Jakob S. Jensen, and Ole Sigmund. Acoustic design by topology optimization. *Journal of Sound and Vibration*, 317(3-5):557–575, 11 2008. doi: 10.1016/j.jsv.2008.03.042.

[40] P. Duysinx and M. P. Bendsøe. Topology optimization of continuum structures with local stress constraints. *International Journal for Numerical Methods in Engineering*, 43(8):1453–1478, 12 1998. ISSN 1097-0207. doi: 10.1002/(SICI)1097-0207(19981230)43:8<1453::AID-NME480>3.0.CO;2-2. URL http://doi.wiley.com/10.1002/%28SICI%291097-0207%2819981230%2943%3A8%3C1453%3A%3AAID-NME480%3E3.0.CO%3B2-2.

[41] P. Duysinx and O. Sigmund. New developments in handling stress constraints in optimal material distribution. In *7th AIAA/USAF/NASA/ISSMO Symposium on Multidisciplinary Analysis and Optimization*, pages 1501–1509. American Institute of Aeronautics and Astronautics Inc, AIAA, 1998. doi: 10.2514/6.1998-4906.

[42] Pierre Duysinx. Topology Optimization with Different Stress Limit in Tension and Compression. 1999.

[43] EASA. Certification Specifications and Acceptable Means of Compliance for Large Aeroplanes. Technical report.

[44] EASA. European Aviation Environmental Report 2019. *Ege Üniv. Ziraat Fak. Derg.*, 40(1):112, 2019. doi: 10.2822/309946.

[45] J Enrique Herencia, Raphael T Haftka, and Vladimir Balabanov. Structural optimization of composite structures with limited number of element properties. 47: 233–245, 2013. doi: 10.1007/s00158-012-0821-5.

[46] E. A. Fancello. Topology optimization for minimum mass design considering local failure constraints and contact boundary conditions. *Structural and Multidisciplinary Optimization*, 32(3):229–240, 9 2006. ISSN 1615147X. doi: 10.1007/s00158-006-0019-9.

[47] P. Fernandes, J. M. Guedes, and H. Rodrigues. Topology optimization of three-dimensional linear elastic structures with a constraint on 'perimeter'. *Computers and Structures*, 73(6):583–594, 1999. ISSN 00457949. doi: 10.1016/S0045-7949(98)00312-5.

[48] A. Gersborg-Hansen, M. P. Bendsøe, and O. Sigmund. Topology optimization of heat conduction problems using the finite volume method. *Structural and Multidisciplinary Optimization*, 31(4):251–259, 4 2006. doi: 10.1007/s00158-005-0584-3.

[49] J. K. Guest, J. H. Prévost, and T. Belytschko. Achieving minimum length scale in topology optimization using nodal design variables and projection functions. *International Journal for Numerical Methods in Engineering*, 61(2):238–254, 9 2004. ISSN 0029-5981. doi: 10.1002/nme.1064. URL http://doi.wiley.com/10.1002/nme.1064.

[50] R. B. Haber, M. P. Bendøse, and C. S. Jog. Perimeter Constrained Topology Optimization of Continuum Structures. pages 113–120. 1996. doi: 10.1007/978-94-009-0153-7{_}15.

[51] R B Haber, C S Jog, and M P Bendsoe. A new approach to variable-topology shape design using a constraint on perimeter. Technical report, 1996.

[52] Zhi Hao Zuo, Yi Min Xie, and Xiaodong Huang. Optimal Topological Design of Periodic Structures for Natural Frequencies. 2011. doi: 10.1061/(ASCE)ST.1943-541X.0000347.

[53] Erik Holmberg, Bo Torstenfelt, and Anders Klarbring. Stress constrained topology optimization. *Structural and Multidisciplinary Optimization*, 48(1):33–47, 7 2013. doi: 10.1007/s00158-012-0880-7.

[54] Ming Kuei Hu. Visual Pattern Recognition by Moment Invariants. *IRE Transactions on Information Theory*, 8(2):179–187, 1962. ISSN 21682712. doi: 10.1109/TIT.1962.1057692.

[55] X. Huang and Y. M. Xie. Optimal design of periodic structures using evolutionary topology optimization. *Structural and Multidisciplinary Optimization*, 36(6):597–606, 11 2008. doi: 10.1007/s00158-007-0196-1.

[56] O Sigmund J Petersson. Slope constrained topology optimization. *Int J Numer Methods Eng*, 41(8):1417–1434, 1998. doi: 10.1002/(sici)1097-0207(19980430)41:8<1417::aid-nme344>3.0.co.

[57] Kai A James, Jorn S Hansen, and Joaquim R R A Martins. Engineering Optimization Structural topology optimization for multiple load cases using a dynamic aggregation technique Structural topology optimization for multiple load cases using a dynamic aggregation technique. 41(12):1103–1118, 2009. ISSN 1029-0273. doi: 10.1080/03052150902926827. URL https://www.tandfonline.com/action/journalInformation?journalCode=geno20.

[58] L Jiang and C W Wu. Topology optimization of energy storage flywheel. doi: 10.1007/s00158-016-1576-1.

[59] Andrei Jipa, Mathias Bernhard, Mania Meibodi, and Benjamin Dillenburger. 3D-Printed Stay-in-Place Formwork for Topologically Optimized Concrete Slabs. In *TxA Emerging Design + Technology*, 2016. URL https://www.researchgate.net/publication/327793571_3D-Printed_Stay-in-Place_Formwork_for_Topologically_Optimized_Concrete_Slabs.

[60] Ali K. Kamrani and Emad Abouel Nasr. Modular Design. In *Engineering Design and Rapid Prototyping*, pages 57–86. Springer, Boston, MA, 2009. doi: 10.1007/978-0-387-95863-7{_}3. URL https://link.springer.com/chapter/10.1007/978-0-387-95863-7_3.

[61] Markus Kaufmann, Dan Zenkert, and Christophe Mattei. Cost optimization of composite aircraft structures including variable laminate qualities. *Composites Science and Technology*, 68(13):2748–2754, 10 2008. ISSN 02663538. doi: 10.1016/j.compscitech.2008.05.024.

[62] U. Kirsch. On singular topologies in optimum structural design. *Structural Optimization*, 2(3):133–142, 9 1990. ISSN 09344373. doi: 10.1007/BF01836562.

[63] Antiopi Koronaki, Paul Shepherd, and Mark Evernden. Rationalization of freeform space-frame structures: Reducing variability in the joints:. *https://doi-org.tudelft.idm.oclc.org/10.1177/1478077119894881*, 18(1):84–99, 1 2020. doi: 10.1177/1478077119894881. URL https://journals-sagepub-com.tudelft.idm.oclc.org/doi/10.1177/1478077119894881.

[64] Lars Krog, Alastair Tucker, Martin Kemp, and Richard Boyd. Topology Optimisation of Aircraft Wing Box Ribs. In *10th AIAA/ISSMO Multidisciplinary Analysis and Optimization Conference*, Reston, Virigina, 8 2004. American Institute of Aeronautics and Astronautics. doi: 10.2514/6.2004-4481.

[65] Lars A. Krog and Niels Olhoff. Optimum topology and reinforcement design of disk and plate structures with multiple stiffness and eigenfrequency objectives. *Computers and Structures*, 72(4):535–563, 8 1999. ISSN 00457949. doi: 10.1016/S0045-7949(98)00326-5.

[66] K. W. Lau Antonio, Richard C.M. Yam, and Esther Tang. The impacts of product modularity on competitive capabilities and performance: An empirical study. *International Journal of Production Economics*, 105(1):1–20, 1 2007. ISSN 09255273. doi: 10.1016/j.ijpe.2006.02.002.

[67] B. S. Lazarov and O. Sigmund. Filters in topology optimization based on Helmholtz-type differential equations. *International Journal for Numerical Methods in Engineering*, 86(6):765–781, 5 2011. ISSN 00295981. doi: 10.1002/nme.3072. URL http://doi.wiley.com/10.1002/nme.3072.

[68] Boyan S. Lazarov and Fengwen Wang. Maximum length scale in density based topology optimization. *Computer Methods in Applied Mechanics and Engineering*, 318:826–844, 5 2017. doi: 10.1016/j.cma.2017.02.018.

[69] Boyan S Lazarov, Fengwen Wang, and · Ole Sigmund. Length scale and manufacturability in density-based topology optimization. *Archive of Applied Mechanics*, 86:189–218, 2016. doi: 10.1007/s00419-015-1106-4.

[70] Chau Le, Julian Norato, Tyler Bruns, Christopher Ha, and Daniel Tortorelli. Stress-based topology optimization for continua. *Structural and Multidisciplinary Optimization*, 41(4):605–620, 4 2010. ISSN 1615147X. doi: 10.1007/s00158-009-0440-y.

[71] Seungjae Lee, Jaeseong Park, Euishin Kwak, Sudeok Shon, Changhoon Kang, and Hosoon Choi. Verification of the seismic performance of a rigidly connected modular system depending on the shape and size of the ceiling bracket. *Materials*, 10 (3), 2017. doi: 10.3390/MA10030263.

[72] Hao Li, Liang Gao, and Peigen Li. Topology optimization of structures under multiple loading cases with a new compliance–volume product. *Engineering Optimization*, 46(6):725–744, 6 2014. ISSN 0305-215X. doi: 10.1080/0305215X.2013.800054. URL http://www.tandfonline.com/doi/abs/10.1080/0305215X.2013.800054.

[73] L J Li, Z B Huang, and F Liu. A heuristic particle swarm optimization method for truss structures with discrete variables. 2009. doi: 10.1016/j.compstruc.2009.01.004.

[74] Lei Li and Kapil Khandelwal. Volume preserving projection filters and continuation methods in topology optimization. *Engineering Structures*, 85:144–161, 2 2015. ISSN 1873-7323. doi: 10.1016/j.engstruct.2014.10.052.

[75] Qing Li, Grant P. Steven, Y. M. Xie, and Osvaldo M. Querin. Evolutionary topology optimization for temperature reduction of heat conducting fields. *International Journal of Heat and Mass Transfer*, 47(23):5071–5083, 11 2004. doi: 10.1016/j.ijheatmasstransfer.2004.06.010.

[76] C. Y. Lin and L. S. Chao. Automated image interpretation for integrated topology and shape optimization. *Structural and Multidisciplinary Optimization*, 20 (2):125–137, 10 2000. doi: 10.1007/s001580050144.

[77] R T Marler and J S Arora. Survey of multi-objective optimization methods for engineering Maximum objective function values. doi: 10.1007/s00158-003-0368-6.

[78] Achille Messac. Physical programming: Effective optimization for computational design. *AIAA Journal*, 34(1):149–158, 5 1996. ISSN 00011452. doi: 10.2514/3.13035.

[79] Aaron Meurer, Christopher P. Smith, Mateusz Paprocki, Ondřej Čertík, Sergey B. Kirpichev, Matthew Rocklin, AMi T. Kumar, Sergiu Ivanov, Jason K. Moore, Sartaj Singh, Thilina Rathnayake, Sean Vig, Brian E. Granger, Richard P. Muller, Francesco Bonazzi, Harsh Gupta, Shivam Vats, Fredrik Johansson, Fabian Pedregosa, Matthew J. Curry, Andy R. Terrel, Štěpán Roučka, Ashutosh Saboo, Isuru Fernando, Sumith Kulal, Robert Cimrman, and Anthony Scopatz. SymPy: Symbolic computing in python. *PeerJ Computer Science*, 2017(1), 2017. doi: 10.7717/PEERJ-CS.103.

[80] A.G.M. Michell. LVIII. The limits of economy of material in frame-structures. *The London, Edinburgh, and Dublin Philosophical Magazine and Journal of Science*, 8 (47):589–597, 11 1904. ISSN 1941-5982. doi: 10.1080/14786440409463229.

[81] E Moses, M B Fuchs, and M Ryvkin. Topological design of modular structures under arbitrary loading. *Struct Multidisc Optim*, 24:407–417, 2003. doi: 10.1007/s00158-002-0254-7. URL http://www.eng.tau.ac.il/~fuchs.

[82] M. G. Mullender, R. Huiskes, and H. Weinans. A physiological approach to the simulation of bone remodeling as a self-organizational control process. *Journal of Biomechanics*, 27(11):1389–1394, 1994. ISSN 00219290. doi: 10.1016/0021-9290(94)90049-3.

B

[83] Danil Nagy, Dale Zhao, and David Benjamin. Nature-Based Hybrid Computational Geometry System for Optimizing Component Structure. *Humanizing Digital Reality*, pages 167–176, 2018. doi: 10.1007/978-981-10-6611-5{_}15. URL https://link.springer.com/chapter/10.1007/978-981-10-6611-5_15.

[84] Danil Nagy, Dale Zhao, and David Benjamin. Nature-Based Hybrid Computational Geometry System for Optimizing Component Structure. In *Humanizing Digital Reality*, pages 167–176. Springer Singapore, 2018. doi: 10.1007/978-981-10-6611-5{_}15.

[85] Katsuya Nomura, Shintaro Yamasaki, Kentaro Yaji, Hiroki Bo, Atsuhiro Takahashi, Takashi Kojima, and Kikuo Fujita. Topology optimization of conductors in electrical circuit. *Structural and Multidisciplinary Optimization*, 59(6):2205–2225, 6 2019. doi: 10.1007/s00158-018-02187-2.

[86] Niels Olhoff, Martin P. Bendsøe, and John Rasmussen. On CAD-integrated structural topology and design optimization. *Computer Methods in Applied Mechanics and Engineering*, 89(1-3):259–279, 8 1991. doi: 10.1016/0045-7825(91)90044-7.

[87] Panos Y Papalambros and Mehran Chirehdast. An Integrated Environment for Structural Configuration Design. *Journal of Engineering Design*, 1(1):73–96, 1990. doi: 10.1080/09544829008901645.

[88] J. París, F. Navarrina, I. Colominas, and M. Casteleiro. Block aggregation of stress constraints in topology optimization of structures. *Advances in Engineering Software*, 41(3):433–441, 3 2010. ISSN 09659978. doi: 10.1016/j.advengsoft.2009.03.006.

[89] Gyung-Jin Park. Structural Optimization. In *Analytic Methods for Design Practice*, chapter 4, pages 171–253. Springer, London, London, 2007. doi: 10.1007/978-1-84628-473-1{_}4. URL https://link.springer.com/chapter/10.1007/978-1-84628-473-1_4.

[90] Thomas A. Poulsen. A new scheme for imposing a minimum length scale in topology optimization. *International Journal for Numerical Methods in Engineering*, 57(6):741–760, 6 2003. ISSN 0029-5981. doi: 10.1002/nme.694. URL http://doi.wiley.com/10.1002/nme.694.

[91] Susana Rojas-Labanda and Mathias Stolpe. Automatic penalty continuation in structural topology optimization. *Structural and Multidisciplinary Optimization*, 52(6):1205–1221, 12 2015. ISSN 16151488. doi: 10.1007/s00158-015-1277-1.

[92] Azriel Rosenfeld and Larry S. Davis. A Note on Thinning. *IEEE Transactions on Systems, Man and Cybernetics*, SMC-6(3):226–228, 1976. doi: 10.1109/TSMC.1976.5409243.

[93] G I N Rozvany. On design-dependent constraints and singular topologies. Technical report, 2001.

[94] G. I. N. Rozvany, M. Zhou, and T. Birker. Generalized shape optimization without homogenization. *Structural Optimization*, 4(3-4):250–252, 9 1992. doi: 10.1007/bf01742754.

[95] G.I.N. Rozvany and T. Birker. On singular topologies in exact layout optimization. *Structural Optimization*, 8:228–235, 1994.

[96] Pablo Sanmiguel. PLD Space, "The European Commercial Launch Service Provider Dedicated to Small Payloads and Small Satellites". In *Small Satellite Conference*, 2021. URL https://digitalcommons.usu.edu/smallsat/2021/all2021/85.

[97] O. Sigmund. A 99 line topology optimization code written in matlab. *Structural and Multidisciplinary Optimization*, 21(2):120–127, 4 2001. ISSN 1615147X. doi: 10.1007/s001580050176.

[98] O Sigmund and J Petersson. Numerical instabilities in topology optimization: A survey on procedures dealing with checkerboards, mesh-dependencies and local minima. Technical report, 1998.

[99] Ole sigmund. Design of material structures using topology optimization. *Department of Solid Mechanics*, (January 1994), 1994.

[100] Ole Sigmund. Optimum Design of Microelectromechanical Systems. In *Mechanics for a New Mellennium*, pages 505–520. Kluwer Academic Publishers, 1 2006. doi: 10.1007/0-306-46956-1{_}33.

[101] Ole Sigmund. Morphology-based black and white filters for topology optimization. *Structural and Multidisciplinary Optimization*, 33(4-5):401–424, 4 2007. ISSN 1615147X. doi: 10.1007/s00158-006-0087-x.

[102] Ole Sigmund and Kurt Maute. Sensitivity filtering from a continuum mechanics perspective. *Structural and Multidisciplinary Optimization*, 46(4):471–475, 10 2012. ISSN 1615147X. doi: 10.1007/s00158-012-0814-4.

[103] M. Stolpe and K. Svanberg. An alternative interpolation scheme for minimum compliance topology optimization. *Structural and Multidisciplinary Optimization*, 22(2):116–124, 2001. doi: 10.1007/s001580100129.

[104] M. Stolpe and K. Svanberg. On the trajectories of penalization methods for topology optimization. Technical Report 2, 4 2001.

[105] Krister Svanberg. The method of moving asymptotes—a new method for structural optimization. *International Journal for Numerical Methods in Engineering*, 24(2):359–373, 1987. ISSN 10970207. doi: 10.1002/nme.1620240207.

[106] G Sved and Z Grsos. STRUCTURAL OPTIMIZATION UNDER MULTIPLE LOADING. Technical report, 1968.

B

[107] Michael Reed Teague. Image analysis via the general theory of moments. *JOSA, Vol. 70, Issue 8, pp. 920-930*, 70(8):920–930, 8 1980. doi: 10.1364/JOSA.70.000920. URL https://www.osapublishing.org/viewmedia.cfm?uri=josa-70-8-920&seq=0&html=truehttps://www.osapublishing.org/abstract.cfm?uri=josa-70-8-920https://www.osapublishing.org/josa/abstract.cfm?uri=josa-70-8-920.

[108] Cho Huak Teh and Roland T. Chin. On Image Analysis by the Methods of Moments. *IEEE Transactions on Pattern Analysis and Machine Intelligence*, 10(4):496–513, 1988. ISSN 01628828. doi: 10.1109/34.3913.

[109] R Timothy Marler, Jasbir S Arora, R T Marler, and J S Arora. The weighted sum method for multi-objective optimization: new insights. 41:853–862, 2010. doi: 10.1007/s00158-009-0460-7.

[110] Imco Van Gent and Christos Kassapoglou. Cost-weight trades for modular composite structures. *Structural and Multidisciplinary Optimization*, 49(6):931–952, 11 2014. doi: 10.1007/s00158-013-1019-1.

[111] Michael Vassilakopoulos and Theodoros Tzouramanis. Quadtrees (and Family). *Encyclopedia of Database Systems*, pages 2946–2952, 2018. doi: 10.1007/978-1-4614-8265-9{_}286. URL https://link.springer.com/referenceworkentry/10.1007/978-1-4614-8265-9_286.

[112] Alexander Verbart, Fred van Keulen, and Matthijs Langelaar. *Topology Optimization with Stress Constraints*. PhD thesis, 2015.

[113] Pauli Virtanen, Ralf Gommers, Travis E. Oliphant, Matt Haberland, Tyler Reddy, David Cournapeau, Evgeni Burovski, Pearu Peterson, Warren Weckesser, Jonathan Bright, Stéfan J. van der Walt, Matthew Brett, Joshua Wilson, K. Jarrod Millman, Nikolay Mayorov, Andrew R. J. Nelson, Eric Jones, Robert Kern, Eric Larson, CJ Carey, İlhan Polat, Yu Feng, Eric W. Moore, Jake VanderPlas, Denis Laxalde, Josef Perktold, Robert Cimrman, Ian Henriksen, E. A. Quintero, Charles R Harris, Anne M. Archibald, Antônio H. Ribeiro, Fabian Pedregosa, Paul van Mulbregt, and SciPy 1. 0 Contributors. SciPy 1.0–Fundamental Algorithms for Scientific Computing in Python. *Nature Methods*, 17(3):261–272, 7 2019. doi: 10.1038/s41592-019-0686-2. URL https://arxiv.org/abs/1907.10121v1.

[114] Fengwen Wang, Boyan Stefanov Lazarov, and Ole Sigmund. On projection methods, convergence and robust formulations in topology optimization. *Structural and Multidisciplinary Optimization*, 43(6):767–784, 6 2011. doi: 10.1007/s00158-010-0602-y.

[115] Xiongwei Wu, Doyen Sahoo, and Steven C.H. Hoi. Recent advances in deep learning for object detection. *Neurocomputing*, 396:39–64, 7 2020. doi: 10.1016/J.NEUCOM.2020.01.085.

[116] Yi Xia, Matthijs Langelaar, and Max A.N. Hendriks. A critical evaluation of topology optimization results for strut-and-tie modeling of reinforced concrete. *Computer-Aided Civil and Infrastructure Engineering*, 35(8):850–869, 8 2020. doi: 10.1111/MICE.12537.

[117] Shengli Xu, Yuanwu Cai, and Gengdong Cheng. Volume preserving nonlinear density filter based on heaviside functions. *Structural and Multidisciplinary Optimization*, 41(4):495–505, 4 2010. ISSN 1615147X. doi: 10.1007/s00158-009-0452-7.

[118] R. J. Yang and C. J. Chen. Stress-based topology optimization. *Structural Optimization*, 12(2-3):98–105, 10 1996. doi: 10.1007/BF01196941.

[119] R. J. Yang and C. H. Chuang. Optimal topology design using linear programming. *Computers and Structures*, 52(2):265–275, 7 1994. ISSN 00457949. doi: 10.1016/0045-7949(94)90279-8.

[120] Guilian Yi and Nam H. Kim. Identifying boundaries of topology optimization results using basic parametric features. *Structural and Multidisciplinary Optimization*, 55(5):1641–1654, 5 2017. doi: 10.1007/s00158-016-1597-9.

[121] Gil Ho Yoon, Hyunggyu Choi, and Shin Hur. Multiphysics topology optimization for piezoelectric acoustic focuser. *Computer Methods in Applied Mechanics and Engineering*, 332:600–623, 4 2018. doi: 10.1016/j.cma.2017.12.002.

[122] Weihong Zhang and Shiping Sun. Scale-related topology optimization of cellular materials and structures. *INTERNATIONAL JOURNAL FOR NUMERICAL METHODS IN ENGINEERING Int. J. Numer. Meth. Engng*, 68:993–1011, 2006. doi: 10.1002/nme.1743. URL www.interscience.wiley.com.

[123] Weisheng Zhang, Wenliang Zhong, and Xu Guo. An explicit length scale control approach in SIMP-based topology optimization. *Computer Methods in Applied Mechanics and Engineering*, 282:71–86, 12 2014. ISSN 00457825. doi: 10.1016/j.cma.2014.08.027.

[124] M. Zhou and G.I.N. Rozvany. The COC algorithm, Part II: Topological, geometrical and generalized shape optimization. *Computer Methods in Applied Mechanics and Engineering*, 89(1-3):309–336, 8 1991. ISSN 00457825. doi: 10.1016/0045-7825(91)90046-9. URL https://linkinghub.elsevier.com/retrieve/pii/0045782591900469.

[125] Mingdong Zhou, Boyan S. Lazarov, Fengwen Wang, and Ole Sigmund. Minimum length scale in topology optimization by geometric constraints. *Computer Methods in Applied Mechanics and Engineering*, 293:266–282, 8 2015. ISSN 00457825. doi: 10.1016/j.cma.2015.05.003.

[126] Mu Zhu, Yang Yang, Andrew T. Gaynor, and James K. Guest. Considering constructability in structural topology optimization. In *Structures Congress 2014 - Proceedings of the 2014 Structures Congress*, pages 2754–2764. American Society of Civil Engineers (ASCE), 2014. ISBN 9780784413357. doi: 10.1061/9780784413357.241.

B